

**A SERS Study of the Electrochemical Reduction
of Carbon Dioxide on Copper Electrodes**

by

Brian Douglas Smith

A thesis

presented to the University of Waterloo

in fulfilment of the

thesis requirement for the degree of

Doctor of Philosophy

in

Chemistry

Waterloo, Ontario, Canada, 1998

© Brian D. Smith, 1998



National Library
of Canada

Acquisitions and
Bibliographic Services

395 Wellington Street
Ottawa ON K1A 0N4
Canada

Bibliothèque nationale
du Canada

Acquisitions et
services bibliographiques

395, rue Wellington
Ottawa ON K1A 0N4
Canada

Your file Votre référence

Our file Notre référence

The author has granted a non-exclusive licence allowing the National Library of Canada to reproduce, loan, distribute or sell copies of this thesis in microform, paper or electronic formats.

The author retains ownership of the copyright in this thesis. Neither the thesis nor substantial extracts from it may be printed or otherwise reproduced without the author's permission.

L'auteur a accordé une licence non exclusive permettant à la Bibliothèque nationale du Canada de reproduire, prêter, distribuer ou vendre des copies de cette thèse sous la forme de microfiche/film, de reproduction sur papier ou sur format électronique.

L'auteur conserve la propriété du droit d'auteur qui protège cette thèse. Ni la thèse ni des extraits substantiels de celle-ci ne doivent être imprimés ou autrement reproduits sans son autorisation.

0-612-30649-6

The University of Waterloo requires the signatures of all persons using or photocopying this thesis. Please sign below, and give address and date.

Abstract

A SERS Study of The Electrochemical Reduction of Carbon Dioxide on Copper Electrodes

A Surface Enhanced Raman Scattering (SERS) study of the intermediates formed on copper during the electrochemical reduction of CO₂ and of the species which poisoned this reaction was conducted. The spectroelectrochemical cell designed for this study allowed SERS spectra from a copper surface in non-halide media to be observed. An electrode pretreatment method using fifteen 1 V/s and two 10 mV/s Oxidation Reduction Cycles (ORCs) was developed to produce clean, SERS active surfaces. The ORC process which created the SERS active surface was explored. The SERS active surface was found to have been formed by the decomposition of an oxide/hydroxide/carbonate layer on the copper electrode surface.

The results from voltammetry, potential step, and time dependence studies were used to assign the observed bands. Potential step experiments were used to explore the origin of the voltammetric features and thus aid in the identification of interfacial species at the copper surface before, during, and after CO₂ reduction. Time dependence studies were performed at -1.06 V, as CO₂ reduction occurred at this potential.

Adsorbed CO was shown to be an intermediate in the reduction of CO₂ and band assignments were made for the CO stretch, the Cu-CO stretch and Cu-CO frustrated rotation. The intensity of all these bands decreased with time while the intensity of the band attributed to the poisoning of the reaction increased. This demonstrated that the changes in band intensity were related to the electrochemical reduction process and not the loss of SERS active sites.

Band assignments for a CH_x species were made. The relationship between the CH_x species and graphite was explored and it was found that a possible interchange existed between these substances. Neither of these substances was found to be associated with the poisoning of CO₂ reduction.

SERS bands of a large number of carbonate/bicarbonate modes were observed. These were from the interfacial region, but did not appear to be involved in the reduction of CO₂ as they varied only slightly in the time dependence studies. Bands for these species were assigned to $\nu_s(\text{Cu-OCO}_2)$, $\nu_1(\text{CO}_3^{2-})$, $\nu_2(\text{CO}_3^{2-})$, $\nu_4(\text{CO}_3^{2-})$, $\nu_5(\text{HCO}_3^-)$.

Bands attributable to Cu₂O were assigned and compared favourably with spectra from oxide films of exposed copper. An oxide/hydroxide patina is proposed as the poisoning species in the reaction, since graphite and carbide were ruled out.

Acknowledgements

I would like to thank Dr. D.E. Irish for his help, guidance and patience throughout the course of this work. I would like to thank Dr. J. Augustynski for the opportunity to work co-operatively with the University of Geneva, and Dr. Peter Kedzierzawski and Dr. Robert Kostecki for their advice and support. I would also like to thank Dr. Z.Q. Tian, Xiamen University, for providing me with a pre-publication copy of his paper and Dr. P. Russell, University of Waterloo, for providing reference mineral samples.

I would like to thank Alexandre Brolo, Dr. Richard Bartholomew, Dr. Marek Odziemkowski, and Dr. G.E. Toogood for their assistance and for making this work more enjoyable.

Finally, I would like to thank my family. I would like to thank my wife, Anne-Marie, for her help in proofreading, typesetting and keeping me from quitting when it seemed that the fates were conspiring against me. As well, I would like to thank my children, Ian, Scott, Andrea and Stephen who each helped out in their own way and to whom I owe a good long family summer vacation this year.

Dedication

"They were having a rest in a small sand-pit on the top of the Forest. Pooh was getting rather tired of that sand pit, and suspected it of following them about, because whichever direction they started in, they always ended up at it, and each time, as it came through the mist at them, Rabbit said triumphantly, 'Now I know where we are!' and Pooh said sadly, 'So do I,' and Piglet said nothing...

'Well,' said Rabbit, after a long silence in which nobody thanked him for the nice long walk they were having, 'we'd better get on, I suppose. Which way shall we try?' 'How would it be,' said Pooh slowly, 'if as soon as we're out of sight of this Pit, we try to find it again?'

'What's the good of that?' said Rabbit. 'Well,' said Pooh, 'we keep looking for Home and not finding it, so I thought that if we looked for the Pit we'd be sure not to find it, which would be a Good Thing because then we might find something that we *weren't*, which might be just what we *were* looking for, really!'

(A.A. Milne, *The House at Pooh Corner*, (1928))

Table of Contents

Chapter 1: Introduction	1
1.0 Scope	2
1.1 Raman Spectroscopy	2
1.1.1 Selection Rules	5
1.1.2 Hyper-Raman Scattering	9
1.1.3 Resonance Raman Scattering	10
1.1.4 Raman Scattering from the Solid State	14
1.2 Spectroscopy of Surface Adsorbates	15
1.2.1 IR Spectroscopy at Surfaces	20
1.2.2 EELS at Surfaces	21
1.2.3 Raman Spectroscopy at Surfaces	22
1.3 Surface Enhanced Raman Scattering (SERS)	25
1.3.1 EM Mechanism	26
1.3.2 CT Model	31
1.3.3 Comparison between EM and CT Models	34
1.3.4 Comparison between SERS, IR and EELS	35
1.4 Carbon Dioxide Equilibria	37
1.4.1 Vibrational Spectroscopy of CO ₂ /H ₂ O	46
1.5 Electrochemical Reduction of CO ₂	50

Chapter 2: Experimental Background	54
2.0 Scope	55
2.1 Chemicals	55
2.2 Cell Design	56
2.3 Electrochemical Instrumentation	59
2.3.1 Electrode Pretreatment	60
2.3.2 Preparation of a SERS Active Surface	60
2.4 Spectroscopic Instrumentation	62
2.4.1 Dilor OMARS 89 Raman Spectrometer	62
2.4.2 Renishaw System 1000 Raman Microscope	64
2.4.3 Spectrometer Comparison	65
Chapter 3: Literature Review	70
3.0 Scope	71
3.1 Solids	71
3.1.1 Copper Oxides	71
3.1.2 Copper Hydroxide	79
3.1.3 Copper Carbonates	80
3.2 Solutions	84
3.3 Electrodes in Bicarbonate Solution	86

3.4 Adsorbates	88
3.4.1 Adsorbed CO	89
3.4.2 Adsorbed CO ₂ and CO ₂ ^{-•}	95
3.4.3 Adsorbed Oxygen	96
3.4.4 Adsorbed CH Groups	98
3.4.5 Adsorbed Water	99
3.5 Electrochemical Reduction of CO ₂ on Copper	103
Chapter 4: Experimental Results and Discussion	109
4.0 Scope	110
4.1 Experimental Results	111
4.1.1 The Creation of SERS Active Surfaces	111
4.1.2 Voltammetry	119
4.1.3 Potential Dependence	123
4.1.3.1 CO ₂ -Saturated 0.1 M NaHCO ₃	124
4.1.3.2 CO ₂ -Saturated 0.1 M KHCO ₃	130
4.1.4 Time Dependence	135
4.1.5 Poisoning Species	140

4.2 Discussion of Band Assignments	144
4.2.1 Adsorbed CO	145
4.2.2 CH _x Species	153
4.2.3.1 CH/Graphitic Carbon Interchange	155
4.2.4 Carbonate/Bicarbonate	159
4.2.5 Copper Oxides	167
4.2.6 Poisoning Species	172
 Chapter 5: Conclusions	 182
5.0 Scope	183
5.1 Cell Design and Instrumentation	183
5.2 SERS Active Surfaces	184
5.3 Band Assignment	184
5.4 SERS Mechanism	186
5.5 Future Work	189
 References	 191

List of Tables

Table 1.1:	Abbreviated Displacement, Polarizability and Hyper-Polarizability Table for a T_d Molecule	12
Table 1.2:	Band Assignments for HCO_3^- and CO_3^{2-} in H_2O	49
Table 1.3:	Equilibrium Electrochemical Potentials (E°) for Possible CO_2 Reduction Products	51
Table 3.1:	Band Assignments for Cu_2O and CuO	73
Table 3.2:	Band Assignments for Copper Carbonates	81
Table 4.1:	Band Assignments from CO_2 -Saturated 0.1 M NaHCO_3/Cu for Potential Step Experiments	126
Table 4.2:	Band Assignments from CO_2 -Saturated 0.1 M NaHCO_3/Cu for Potential Step Experiments	132
Table 4.3:	Band Assignments for the Poisoning Species at Various Potentials from Figure 4.11; CO_2 -Saturated 0.1 M NaHCO_3/Cu	142

List of Figures

Fig. 1.1:	A Diagrammatic Representation of Rayleigh and Raman Scattering	4
Fig. 1.2:	An Illustration of the Vibrational Modes of a Linear Molecule ($D_{\infty h}$), e.g., CO_2	7
Fig. 1.3:	An Illustration of the Vibrational Modes of a Tetrahedral Molecule (T_d), e.g., CCl_4	11
Fig. 1.4:	A Generalized Co-ordinate System for the Interaction of Light with a Surface	17
Fig. 1.5:	A Schematic of the Image Charge Model	19
Fig. 1.6:	A Schematic Illustration of the CT Mechanism of SERS Enhancement	32
Fig. 1.7:	An Equiligraph for an Open Carbonate System at $P_{CO_2} = 1$ atm.	39
Fig. 1.8:	An Equiligraph for a Closed System $C_T = 0.1$ M	41
Fig. 1.9:	An Equiligraph of a Closed System after C_T is Reduced to 0.09 M	44
Fig. 1.10:	An Equiligraph of a Closed System after C_T is Reduced to 0.075 M	45
Fig. 1.11:	An Illustration of the Vibrational Modes of a Planar Triangular Molecule (D_{3h}), e.g., CO_3^{2-}	47
Fig. 1.12:	The Proposed Mechanism for CO_2 Reduction on Ag, Au, Cu, and Zn Surfaces	52
Fig. 2.1:	A Diagram of the Spectroelectrochemical Cell Used for SERS Experiments	57
Fig. 2.2:	A Block Diagram Comparing the Renishaw and Dilor Instruments	66

Fig. 2.3:	A Comparison of the Modes of Adsorbed CO on Copper at -1.26 V between the Renishaw and Dilor Instruments	68
Fig. 3.1:	Spectra from Azurite and Malachite Mineral Samples	82
Fig. 3.2:	The Distribution of Cu ²⁺ Species as a Function of pH	85
Fig. 3.3:	A Pourbaix Diagram for the Cu/CO ₂ /H ₂ O System at 0.1 M Total Carbonate Concentration	87
Fig. 3.4:	A Illustration of the Vibrational Modes of an Adsorbed CO	91
Fig. 4.1:	A Cyclic Voltammogram from CO ₂ -Saturated 0.1 M NaHCO ₃ /Cu at 1 V/s from -1.56 to 1.3 V	113
Fig. 4.2:	Spectra from the Cu Electrode at -1.06 V in CO ₂ -Saturated 0.1 M NaHCO ₃ where Each Cycle Represents 3 ORCs at 1 V/s	115
Fig. 4.3:	Spectra from the Cu Electrode at -1.06 V in CO ₂ -Saturated 0.1 M NaHCO ₃ where Each Cycle Represents 1 ORC at 10 mV/s	117
Fig. 4.4:	A Comparison between 10 mV/s and 1 V/s Cleaning Cycles	118
Fig. 4.5:	A Set of 3 Voltammograms Run at 10 mV/s with Anodic Limits of 1.3, 0.74 and 0.54 V for CO ₂ -Saturated 0.1 M NaHCO ₃ /Cu	121
Fig. 4.6:	Spectra from the Cu Electrode in CO ₂ -Saturated 0.1 M NaHCO ₃ for Potential Step Experiments	125
Fig. 4.7:	Spectra from the Cu Electrode in CO ₂ -Saturated 0.1 M KHCO ₃ for Potential Step Experiments	131
Fig. 4.8:	Time Dependence Spectra from the Cu Electrode at -1.06 V in CO ₂ -Saturated 0.1 M NaHCO ₃	136
Fig. 4.9:	Time Dependence Spectra from the Cu Electrode at -1.06 V in CO-Saturated 0.1 M NaHCO ₃	138

Fig. 4.10:	Time Dependence Spectra from the Cu Electrode at -1.06 V in CO ₂ -Saturated 0.1 M KDCO ₃	139
Fig. 4.11:	Spectra of the Poisoning Species from the Cu Electrode at Various Potentials in CO ₂ -Saturated 0.1 M NaHCO ₃	141
Fig. 4.12:	Spectra from the Cu Electrode in CO ₂ -Saturated 0.1 M NaHCO ₃ for the CO Stretching Region	147
Fig. 4.13:	Spectra from the Cu Electrode in CO ₂ -Saturated 0.1 M KHCO ₃ for the CO Stretching Region	148
Fig. 4.14:	Time Dependence of the Intensity of the CO Stretching Band from the Cu Electrode at -1.06 V in Gas-Saturated 0.1 M Electrolyte	150
Fig. 4.15:	Spectra from the Cu Electrode at -1.21 V in 0.1 M NaHCO ₃	151
Fig. 4.16:	Spectra from the Cu Electrode at -1.26 V in CO ₂ -Saturated 0.1 M KDCO ₃	156
Fig. 4.17:	Spectra Comparing CH _x and Possible Graphite Bands from the Cu Electrode in CO ₂ -Saturated 0.1 M NaHCO ₃	158
Fig. 4.18:	Spectra from the Cu Electrode in CO ₂ -Saturated 0.1 M NaHCO ₃ for the Carbonate/Bicarbonate Region	160
Fig. 4.19:	Spectra from the Cu Electrode in CO ₂ -Saturated 0.1 M KHCO ₃ for the Carbonate/Bicarbonate Region	161
Fig. 4.20:	Spectra from Azurite and Malachite Compared to the Cu Electrode at -0.36 V in CO ₂ -Saturated 0.1 M NaHCO ₃ and KHCO ₃	166
Fig. 4.21:	Spectra from the Cu Electrode in CO ₂ -Saturated 0.1 M NaHCO ₃ for the Oxide Region	168
Fig. 4.22:	Spectra from the Cu Electrode in CO ₂ -Saturated 0.1 M KHCO ₃ for the Oxide Region	169

Fig. 4.23:	Reference Spectra Measured in Air from a Cu Electrode Before and After Cleaning and a Penny	171
Fig. 4.24:	Time Dependence of the Intensity of the Poisoning Band from the Cu Electrode at -1.06 V in Gas-Saturated 0.1 M Electrolyte	173
Fig. 4.25:	Spectra Comparing Poisoning Species from the Cu Electrode at -1.76 V in CO ₂ -Saturated 0.1 M Electrolyte	176
Fig. 4.26:	Spectra Comparing Poisoning Species Bands from the Cu Electrode at 0.14 V in CO ₂ -Saturated 0.1 M Electrolyte with Bands from Oxidized Cu	180

Chapter 1

Introduction

1.0 Scope

The electrolysis of a carbon dioxide saturated aqueous solution at a copper electrode yields a number of products, including hydrocarbons. The mechanism by which CO_2 is reduced is not certain. The goal of this research is to seek the identities of intermediates and products, and thereby elucidate the mechanism of the reduction process. The approach has been to apply Raman spectroscopy to this study.

This chapter will present a brief review of the theory of classical Raman Spectroscopy, Surface Enhanced Raman Scattering (SERS), carbon dioxide solution equilibria, and the general aspects of the electrochemical reduction of CO_2 . This will provide the necessary background for understanding the experimental results and discussion which follows. Background specific to copper electrodes is presented in Chapter 3.

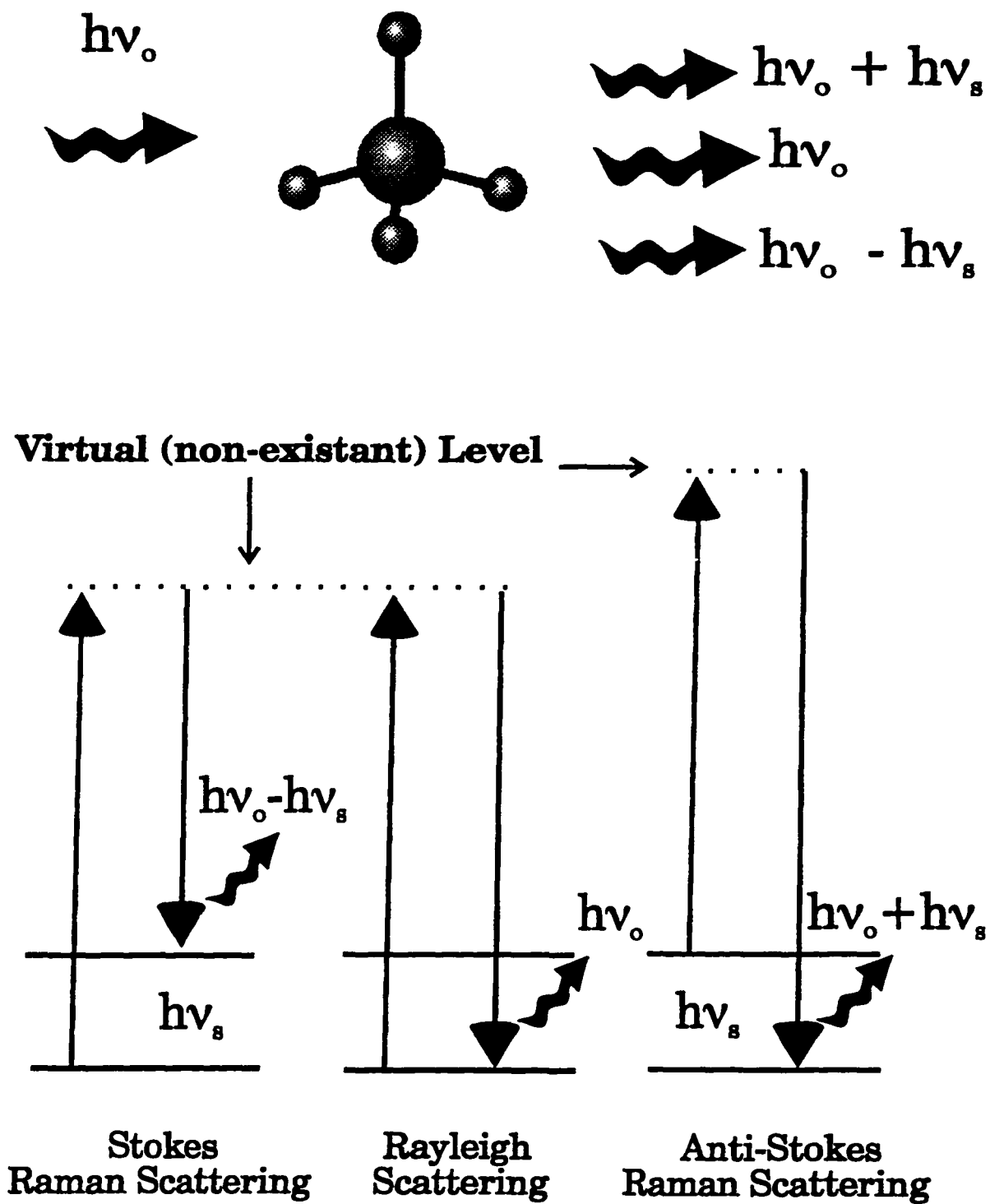
1.1 Raman Spectroscopy

This section will briefly cover classical vibrational Raman spectroscopy. Detailed discussions of the theory and practical aspects of Raman spectroscopy are readily available [1-4]. Raman spectroscopy utilizes visible light to excite energy level changes within molecules. Since vibrational energy changes are

characteristic of specific molecules, Raman spectroscopy can be used to identify molecular species.

If the incident light is viewed as a beam of particles, or quanta of energy, this becomes more apparent (Fig. 1.1). A photon ($h\nu_o$) colliding with a molecule can be scattered with higher ($h\nu_o+h\nu_s$), lower ($h\nu_o-h\nu_s$), or the same ($h\nu_o$) energy. The collision between the photon and the molecule is described as either elastic or inelastic. Raman scattering occurs from an inelastic collision which results in either a higher-energy or lower-energy scattered photon. The change in energy is the result of a transition between energy states. This provides information about the molecule. When the molecule undergoes a transition from an excited to a ground state, a photon of higher energy is emitted; this is termed Anti-Stokes Raman scattering. If the molecule undergoes a transition from a ground state to an excited state, an energy loss is observed yielding Stokes Raman scattering. Since the populations of the molecules in a given set of energy states are governed by a Boltzmann distribution, a greater number of molecules will be in a lower energy state at room temperature. As a result, more Stokes Raman scattering occurs, which provides more intense spectral features. Thus Stokes Raman scattering is most commonly measured. When an elastic collision occurs, there is no energy change. This results in Rayleigh scattering. Rayleigh scattering is ca. 10^6 times as intense as Raman scattering.

Fig. 1.1: A Diagrammatic Representation of Rayleigh and Raman Scattering



1.1.1 Selection Rules

Raman scattering provides information complementary to that provided by infrared spectroscopy (IR). IR spectra result from the absorption of a photon with an energy equal to the difference between vibrational energy states ($h\nu_g$). The complementary natures of these two techniques are also revealed through the mechanisms by which this energy change occurs. In order to obtain an IR spectrum from a molecule, the vibrational mode itself must involve a change in the dipole moment of the molecule. Raman spectra result from a change in the dipole moment induced by the incident radiation. The induced dipole moment, μ , is related to the applied electric field from the radiation, \mathbf{E} , by the equation:

$$\mu = \alpha\mathbf{E}.$$

The α is referred to as the polarizability of the molecule. Since \mathbf{E} and μ can be different in the x, y and z directions this can be expressed in matrix form as:

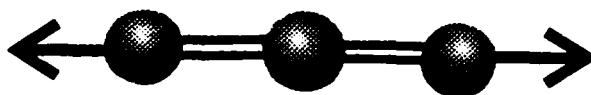
$$\begin{bmatrix} \mu_x \\ \mu_y \\ \mu_z \end{bmatrix} = \begin{bmatrix} \alpha_{xx} & \alpha_{xy} & \alpha_{xz} \\ \alpha_{yx} & \alpha_{yy} & \alpha_{yz} \\ \alpha_{zx} & \alpha_{zy} & \alpha_{zz} \end{bmatrix} \begin{bmatrix} E_x \\ E_y \\ E_z \end{bmatrix}$$

It is possible to use the α terms to construct a polarizability ellipsoid. The Raman scattering is dependant on this ellipsoid changing shape during a given vibration.

In order to further illustrate the differences between the IR and Raman spectrum of a molecule it is useful to consider CO_2 . There are four normal modes of vibration for the CO_2 molecules. It can be seen in Fig. 1.2 that there is no change in dipole moment for the ν_1 mode, since the bond dipoles induced by this motion are at 180° to each other. Since there is no net dipole induced in the molecule, this vibration is IR inactive. However, it is Raman active, because qualitatively the electron density thickens and thins as the molecule vibrates which changes the polarizability ellipsoid.

Campion [5] provided a convenient method of visualising the changes in the polarizability ellipsoid. Since different motions of the molecule alter the polarizability of each bond, the polarizability ellipsoid undergoes an overall expansion and contraction during a vibration. This can be compared with the antisymmetric stretch ν_3 which is Raman inactive and IR active. It can be seen from Fig. 1.2 that the dipole moment will be additive for this mode since it involves the compression of one bond and the expansion of another bond. It can be argued that the polarizability ellipsoid will not change during this vibrational mode since the change induced by the compression of one bond will

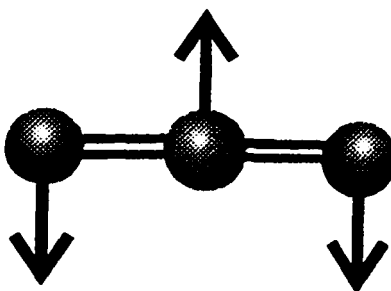
Fig. 1.2: An Illustration of the Vibrational Modes of a Linear Molecule ($D_{\infty h}$), e.g., CO_2



$\nu_1(\Sigma_g^+ \text{ or } A_{1g})$



$\nu_3(\Sigma_u^+ \text{ or } A_{1u})$



$\nu_2(\Pi_u \text{ or } E_{1u})$

be offset by the expansion of the other. These arguments while illustrative are only useful for cases which are intuitive. The polarizability change for the bending mode ν_2 of the molecule is not as intuitive. It is a doubly degenerate mode; the displacement vectors can be rotated by 90° , in and out of the plane, giving a second mode with the same frequency. In order to determine that this mode is IR active and Raman inactive, a more complex mathematical characterization must be made.

Character tables of the mathematics of groups [2], where the geometry of a molecule is given by a point group symbol deduced from the symmetry elements which describe it, aid in the assignment of vibrational modes. The characters of the (x,y,z) components, known as the Cartesian displacement vectors, indicate whether the mode is IR active. When the characters of the vibrational mode are the same as at least one of the Cartesian displacement vectors, the mode is IR active. The quadratic components (xx,xy,xz,yy...zz) are associated with the polarizability of the molecules ($\alpha_x \dots \alpha_z$), and indicate whether the mode is Raman active. When characters of the vibrational mode are the same as at least one of the quadratic components, the mode is Raman active.

The Cartesian displacement vectors and quadratic components are mutually exclusive for molecules which contain a centre of symmetry.

Therefore, the IR and Raman spectra are mutually exclusive in such cases. This is the case for the CO₂ (D_{∞h}) molecule. The modes are referred to as g, even modes, and u, odd modes; the g modes cannot be IR active and the u modes cannot be Raman active under normal conditions.

Comparison of the results from IR and Raman spectra aids in determining vibrational modes, and the symmetry of molecules. If the symmetry of a molecule is known, the combination of IR and Raman spectroscopy can be used to assign the vibrational modes. Likewise, if the vibrational modes are known, the combination of IR and Raman spectroscopy can be used to determine the symmetry of the molecule.

1.1.2 Hyper-Raman Scattering

The equation for the induced dipole can be expanded by including the polarizability, α , and hyper-polarizability, β , as follows:

$$\boldsymbol{\mu} = \alpha\mathbf{E} + \frac{1}{2}\beta\mathbf{E}^2$$

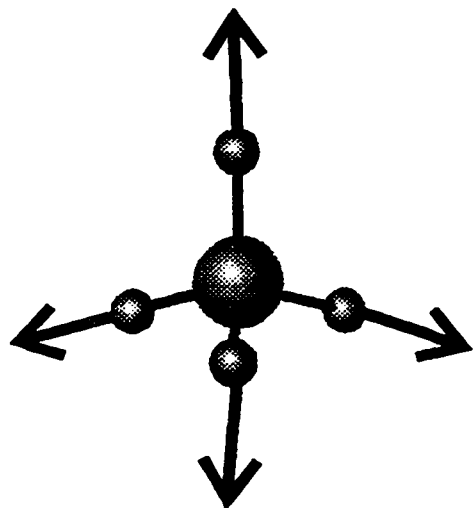
The hyper-polarizability, β , can be expanded for all xyz components and contains 27 elements. Therefore, the selection rules for Hyper-Raman and Raman scattering are different. As an example for contrasting the selection

rules for IR, Raman and Hyper-Raman scattering consider a tetrahedral molecule which belongs to the point group T_d (e.g., CCl_4). Pictorial representations of the vibrational modes, similar to those presented by Nakamoto [1], are shown in Fig. 1.3. Table 1.1 is an abbreviated version of the table presented by Long [2], which lists the displacement, polarizability, and hyper-polarizability for a tetrahedral molecule (T_d). Since the F_2 modes transform as (x,y,z) , they are the only ones which involve a change in the dipole moment of the molecule. Therefore, they are the only ones that are active in the IR. The irreducible representation of all the vibrational modes span α terms and as a result a change in the polarizability ellipsoid of the molecule occurs. Thus, all four vibrational modes are Raman active. Since the components of β , hyper-polarizability, are not associated with the modes of E symmetry, these will not be active in the Hyper-Raman spectrum of a T_d molecule but the A_1 and F_2 will be. Long [2] reported that this was indeed the case for CCl_4 .

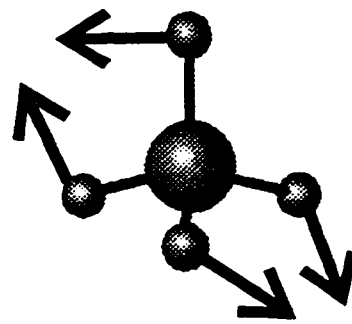
1.1.3 Resonance Raman Scattering

The resonance effect occurs in Raman scattering when the energy of the incident radiation is equal to an electronic transition within the molecule. In this case instead of the molecule being excited to a virtual (non-existent) state, as indicated in Fig. 1.1, the molecule can be excited into another electronic

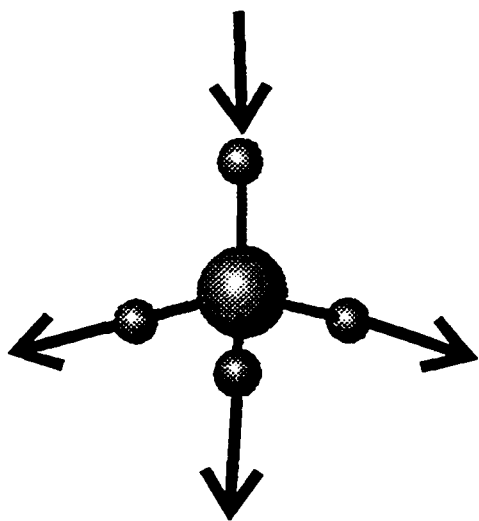
Fig. 1.3: An Illustration of the Vibrational Modes of a Tetrahedral Molecule (T_d), e.g., CCl_4



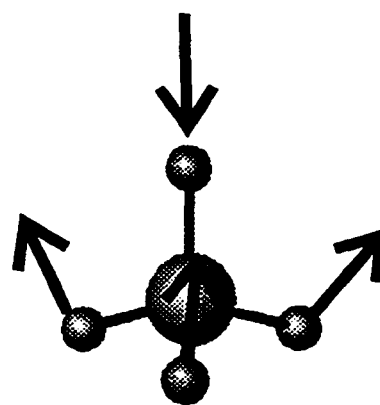
$\nu_1(A_1)$



$\nu_2(E)$



$\nu_3(F_2)$



$\nu_4(F_2)$

Table 1.1: Abbreviated Displacement, Polarizability and Hyper-Polarizability Table for a T_d Molecule

Td	Displacement (IR Activity)	Polarizability (Raman Activity)	Hyper-Polarizability (Hyper-Raman Activity)
A_1		$\alpha_{xx} + \alpha_{yy} + \alpha_{zz}$	(β_{xyz})
E		$\alpha_{xx} + \alpha_{yy} - 2\alpha_{zz}$ $\alpha_{xx} - \alpha_{yy}$	
F_2	(x, y, z)	$\alpha_{xy}, \alpha_{yz}, \alpha_{zx}$	$(\beta_{xxx}, \beta_{yyy}, \beta_{zzz})$ $(\beta_{xyy} + \beta_{zzx}, \beta_{xxy} + \beta_{yzz}, \beta_{zxx} + \beta_{yyz})$

state. This causes a considerable increase in the signal which makes the resonance Raman spectroscopic technique very sensitive, but also very specific. If the exciting frequency is not the same as the electronic transition, the resonance does not occur and the Raman scattering is considerably weaker.

In normal Raman scattering the α terms of the polarizability are not dependent on the incident radiation frequency ν_0 . In Resonance Raman Scattering (RRS), this is not the case and the polarizability is expressed as:

$$\alpha = A + B + C + D$$

Each of these terms is then expanded into an expression containing the wavefunctions of the electronic excited states that are potentially involved in the resonance process. The A term scattering deals with the transition between the ground and excited states of the molecule. The B term deals with the transition between the ground and excited states, as well as the mixing of resonantly excited state with other excited states, accessible from dipole allowed transitions. Since the C and D terms involve transitions to highly excited electronic states, they are usually not considered to be major contributors to the RRS [6].

The A term enhancement is only observed for totally symmetric modes. The contributions made by the B term scattering may apply to both totally symmetric and non-totally symmetric vibrations depending on the symmetries of the excited vibrational states that can be accessed. The A term will give rise to overtones in the RRS spectrum but the B term will not [6].

1.1.4 Raman Scattering from the Solid State

The principles of Raman spectroscopy, which deal with isolated molecules (i.e., gas phase species), generally can be applied to molecules in liquid and solution phases. In the solid state the atoms are fixed in space and this changes the nature of the Raman scattering. In solids there are internal modes which are vibrations of the molecules that compose the crystal (e.g., the CO_3^{2-} modes in solid carbonate species). These modes will behave in a manner similar to the gas and liquid phases.

In solids it is also possible to have collective translational and rotational motions of the molecules composing the crystal. These collective oscillations of the components of the crystal are referred to as phonons. Phonons, like molecular oscillations, are quantized and Raman scattering can be observed from them. Phonons can be further classified into four groups TO (Transverse Optical), LO (Longitudinal Optical), TA (Transverse Acoustic), and

LA (Longitudinal Acoustic). Transverse phonons have the motion of the atoms in the crystal perpendicular to the direction of propagation of the phonon. In a longitudinal mode the motion of the molecules in the crystal is in the same direction as the propagation of the phonon. Optical modes are those for which there is a dipole moment change caused by the motions in the crystal. Acoustic phonons do not have a dipole change associated with their motion [7].

It is also possible to have RRS from a solid. The mechanism of this excitation can be quite complex, such as the creation of an exciton. An exciton is defined as a bound electron-hole pair, which is free to move through a crystal as a neutral species [7]. The fundamental principle that the incident radiation frequency ν_0 must be the same as an allowable electronic excitation of the solid still applies.

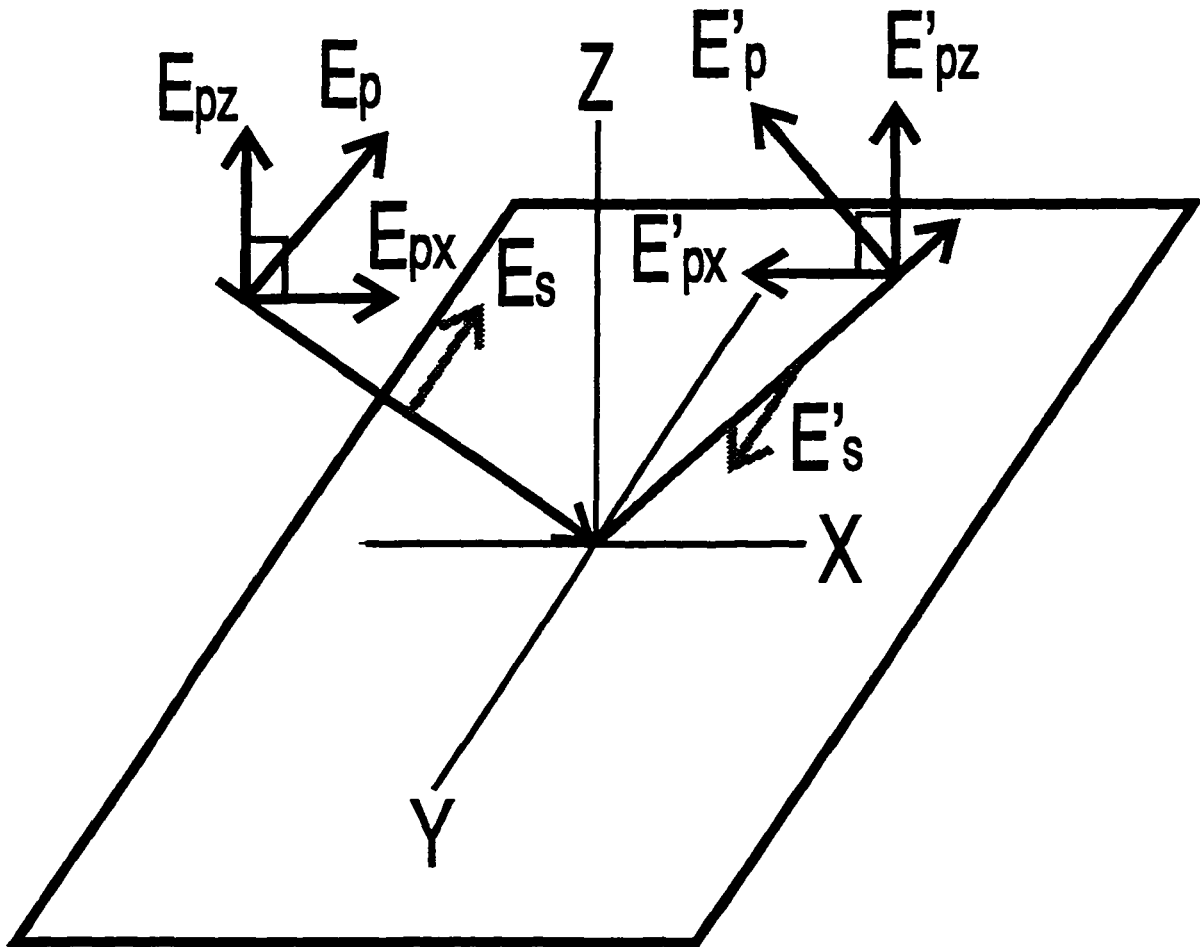
1.2 Spectroscopy of Surface Adsorbates

A molecule that is adsorbed on a surface can be classified as chemisorbed or physisorbed. According to Somorjai [8] a species is chemisorbed if the interaction with the substrate is significantly stronger than the interaction between adsorbate species. For a physisorbed species the reverse is true; the interaction with the substrate is minimal compared with the interactions between adsorbate species on the surface.

In order to obtain information from a surface species the interaction of light with a surface system needs to be considered. Figure 1.4 shows a generalized coordinate system for optical surface spectroscopy; the surface is in the XY plane. The electric field of the incident radiation can be separated into two components, E_p and E_s , orthogonal to the direction of propagation and to each other. Light which is polarized in the plane of the surface (the XY plane) is referred to as s-polarized. Light which is polarized in the plane of incidence (i.e., the XZ plane) is referred to as p-polarized. In the case of p-polarized light the E_p can be further divided into E_{px} and E_{pz} components. After reflection at the surface each of these components undergo a 180° phase shift. These are labelled as E'_s , E'_p , E'_{px} and E'_{pz} . Owing to this phase reversal on reflection, the electric fields of the s and Px components individually cancel and result in a reduced electric field at the surface. However, for the Pz component the direction of the field is unchanged on reflection. This would indicate that for a perfect mirror there can be no net electric field in the plane of the surface for any angle of incidence.

Campion [5] demonstrated this for a perfect silver mirror by calculating the normalized electric field strengths for light with an incident wavelength of $5 \mu\text{m}$. He demonstrated that the maximum field strength is achieved for a grazing angle of incidence (i.e., as close to 90° from normal as possible). Most metals are not perfect mirrors when the incident light is in the visible or

Fig. 1.4: A Generalized Co-ordinate System for the Interaction of Light with a Surface

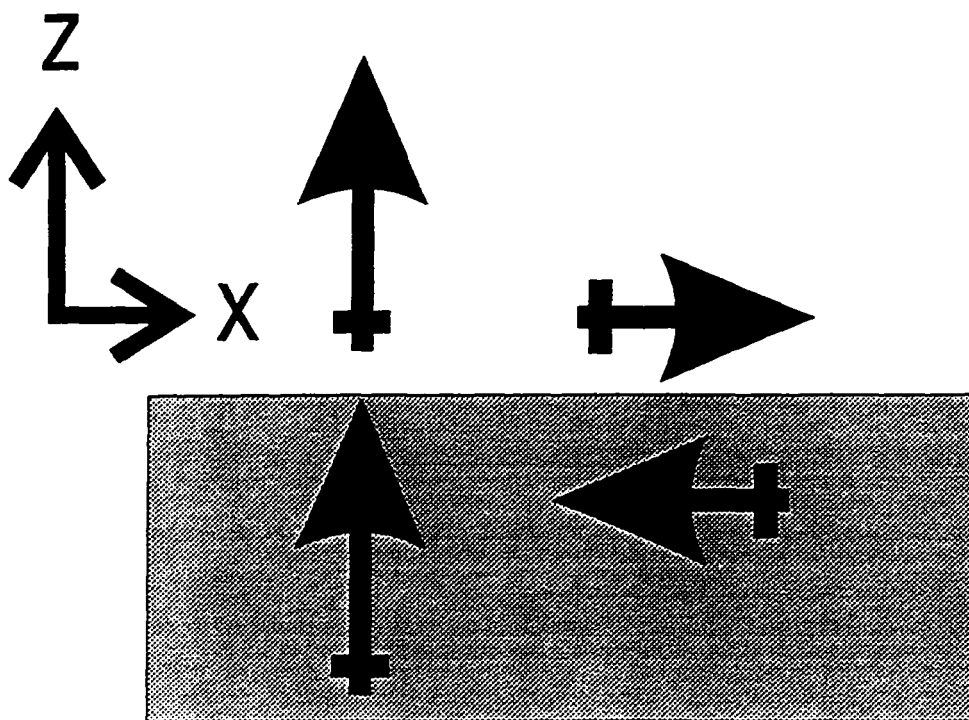


the UV. Nevertheless, it is possible to calculate the electric field component at the surface from the E_z and E_{px} components of the incident light. This has been shown for silver where the tangential components of the field at the surface are found to increase as the energy of the incident light increases [9]. It is also possible to show that the P_z component will reach its maximum for an incident angle of ca. 60° from normal for visible light [5,9].

Another consideration for obtaining spectra from species adsorbed onto a surface is the effect of the dipole of the adsorbate on the metal surface. This can be expressed in terms of an image charge model, which is illustrated in Fig. 1.5. If the dipole, or a component of the dipole, is oriented along the Z axis, it is possible for it to induce an image charge in the metal below. This will result in a net increase in the effective dipole at the surface. However if the dipole, or a component of it, is oriented parallel to the surface (i.e., in the XY plane), the induced dipole will oppose the dipole at the surface and no net dipole will result. This is known as the dipole selection rule.

One final consideration is the assignment of the symmetry species of surface adsorbates. A thorough review of this subject has been given by Richardson and Sheppard [10]. A molecule adsorbed at a surface can possess neither inversion symmetry, a plane of symmetry in the plane of the surface, nor an improper axis of rotation. The symmetry of the adsorbed species will

Fig. 1.5: A Schematic of the Image Charge Model



Dipole increased
by image charge

Dipole Screened
by image charge

depend on the symmetry of the adsorption site (e.g., a three fold hollow site would have C_{3v} symmetry). This limits the available symmetry groups to C_1 , C_s , C_2 , C_3 , C_4 , C_6 , C_{2v} , C_{3v} , C_{4v} , C_{6v} . Urban [11] considered it possible for a molecule adsorbed on an "on top" site to possess $C_{\infty v}$ symmetry.

1.2.1 IR Spectroscopy at Surfaces

Bradshaw and Schwitzer [12], Heyden [13], and Beden and Lamy [14] have provided reviews of the application of IR spectroscopy for studying adsorbed molecules on metallic surfaces. Since a metal is not transparent, IR spectra have to be collected from surface species by reflection. This is called RAIRS (Reflection Absorption Infrared Spectroscopy) or IRAS (Infrared Reflection Absorption Spectroscopy). When this technique is applied to an electrode surface, a modulation of the electrode between a working and a reference potential can be incorporated. This is called EMIRS (Electrochemically Modulated Infrared Reflectance Spectroscopy) or SNIFTIRS (Subtractively Normalized Interfacial Fourier Transform Infrared Spectroscopy) [14]. For all of these techniques the strength of the incident electric field at the metal surface will determine the intensity of the adsorption that can be observed. Several authors [12-14] have shown that the intensity of the E_{pz} component can be maximized by using a grazing angle of incidence and it is this component which interacts with dipoles on the surface. The E_{px} and

E_x light components do not interact significantly with the adsorbate. Also due to the dipole selection rule, the E_{p_z} component of the light can only interact with the dipole, or component of the dipole, which is oriented along the Z axis. As a result, surface IR spectroscopy is sensitive to modes of vibration which have a component of their dipole oriented in the Z direction.

1.2.2 EELS at Surfaces

Electron Energy Loss Spectroscopy (EELS) is a technique which uses inelastically scattered electrons to probe the energy states of adsorbates on metals. Chesters and Sheppard [15] have written a review of this subject. If the incident energy of the electron beam is low enough, then it is possible to resolve the vibrational structure of the adsorbates. This is often referred to as HREELS (High Resolution Electron Energy Loss Spectroscopy). Although electrons, being charged particles with rest mass, will not interact with the surface of a metal in the same manner as photons, the interaction is similar enough that some of the principles of photon spectroscopy at surfaces can qualitatively be applied. If the incident electron interacts with the adsorbate, it can be scattered with a lower energy than the incident electron. This is somewhat analogous to the scattering of photons in the Raman effect. The most common form of EELS scattering, via a dipole mechanism, is similar to

that shown in Fig. 1.5 for photon spectroscopy. The surface selection rules for this form of EELS and IR at surfaces are very similar.

The dipole mechanism applies in most HREELS, which involves collecting specularly scattered electrons. If the collection of electrons is in an off-specular direction, it is possible to observe impact scattering effects. By varying the angle at which the scattered electrons are observed, impact scattering makes possible the observation of vibrational modes which are not allowed via dipole scattering.

1.2.3 Raman Spectroscopy at Surfaces

Raman spectroscopy has a number of advantages for the study of surface species. As a visible light technique, it is possible to examine species which are covered by a liquid phase. Many other surface science techniques which employ electrons as the probe particle require Ultra High Vacuum (UHV) conditions. The region of the spectrum between 50 and 500 cm^{-1} is as readily observable as the higher wavenumber region. This region, which is of particular interest in surface studies since it contains information about the vibration mode of the metal adsorbate bond, is not easily observed with IR spectroscopy. Since Raman spectroscopy uses visible light, cells can be constructed with glass windows which permit measurement over the entire

spectral range. IR spectroscopy normally uses inorganic halide or chalconide materials which can obscure portions of the spectral range. Another advantage of Raman spectroscopy is the ability to focus the incident exciting light. This allows specific areas on a surface to be studied and spatial information to be obtained.

In spite of the apparent advantages of Raman spectroscopy, it is limited by the inherent weakness of the Raman effect. Since only one in 10^6 photons is Raman scattered, the very large amount of Rayleigh scattering must be removed by some optical device. However, the use of any optical device significantly reduces the observed Raman scattering. Campion [5] provided a simple calculation to illustrate this point. If it is assumed that there is roughly a monolayer of adsorbate on a smooth surface then it is expected that the Raman scattering will be of the order of 2.5×10^2 counts per second. However, in order to observe this, it is necessary to separate the Raman and Rayleigh scattering. For a classical monochromator instrument with a Photomultiplier Tube (PMT), the throughput of Raman scattering is estimated at 10% for the monochromator and the PMT is estimated to be about 10% efficient. This will reduce the signal to 2-3 counts per second which is insufficient to distinguish this signal from other background noise. If an intensified photodiode array is used, it is possible to speed up the collection time by collecting ca. 500 cm^{-1} at a time. Adding the spectra increases the signal to noise ratio providing about

30% efficiency. With careful technique Campion [5] was able to observe submonolayer amounts of nitrobenzene on Ni(111) using an intensified photodiode array. However this required very precise optical alignment and long accumulation times. Instead of using a monochromator the most recent generation of Raman instruments increases the throughput by using a holographic notch filter which is about 90% efficient and a Charge Coupled Device (CCD), which is 50 - 70% efficient or better, as a detector [16,17]. This provides instruments capable of more readily observing surface species.

As with EELS, a modification of the dipole selection rule applies for species adsorbed on the surface of the electrode. In the IR the maximum for the electric field E_{p_z} occurs at $\sim 90^\circ$ to the surface normal. This is not true for Surface Raman spectroscopy. Campion [5] pointed out that since the dielectric constant of the metal changes with the energy of the incident light, the angle of incidence at which the maximum in the E_{p_z} light component occurs is at ca. 60° to the surface normal. Campion concluded that the optimum angle of observation should be ca. -60° from the surface normal. Campion also produced a series of selection rules for unenhanced Surface Raman spectroscopy [5]. These rules are similar to, but not the same as, those for IR spectroscopy since the Raman effect involves a change in the polarizability, α , whereas IR involves a change in the dipole moment. The selection rules are inferred from the differential enhancement observed for those modes with an induced dipole

component normal to the surface. Because the Pz component of the electric field is strongest, modes with α_{ZZ} will be most enhanced whereas modes with α_{XZ} , α_{YZ} , α_{ZX} , α_{ZY} , will be enhanced to a lesser degree. The other species which transform only as X and Y terms will be virtually non-observable due to the low strength of the tangential electric fields.

1.3 Surface Enhanced Raman Scattering (SERS)

The preceding discussion of the Raman spectra has applied only to species that are adsorbed on smooth metal surfaces. For certain metals, if the surface is roughened, the observed Raman scattering from adsorbates can be enhanced up to 10^6 . This enhancement is called Surface Enhanced Raman Scattering (SERS). SERS was first observed in electrochemical systems for pyridine adsorbed on silver electrodes [18]. The metals which have been confirmed to provide this effect include silver, copper, gold, lithium, sodium and potassium [5]. It has recently been reported that, with improved instrumentation, it is possible to observe SERS from platinum, palladium, rhodium, ruthenium, nickel, cobalt, and iron [19]. Thus by studying systems which exhibit SERS, valuable information about the surface species can be observed.

The mechanism of SERS relates to how certain metals are able to modify the intensity of the observed Raman scattering. As previously noted the Raman intensity is proportional to the induced dipole, μ where:

$$\mu = \alpha \mathbf{E}.$$

If either the strength of the electric field, \mathbf{E} , or the polarizability of the molecule, α , is increased, both μ and the observed Raman scattering will increase. Two theoretical approaches have been developed to explain SERS. The electromagnetic or EM mechanism accounts for the changes in the local electric field, \mathbf{E} , that are induced by roughness features on the surface of the electrode, in analogy to the calculations previously discussed for Raman scattering from smooth surfaces. The charge transfer or CT mechanism considers the modification of the polarizability, α , through a charge transfer between the metal and the adsorbate. This approach bears a number of similarities to RRS [9,20-23].

1.3.1 EM Mechanism

The EM mechanism attributes the increase in the SERS intensity to an increase in the local electric field experienced by the molecules, which results from small bumps on the surface. These can be in the form of spheres [6] or

ellipsoids [6], or the whole surface can be viewed as a sinusoidal grating [9]. The simplest model of the EM enhancement is provided by considering an isolated sphere, as outlined by Creighton [6]. If the sphere has a diameter less than $1/20$ of the wavelength of the incident radiation then the response of the surface plasmons (collective oscillations of the electrons in the metal) will resemble that of a dipole. This will result in an effective polarizability of the sphere that will be dependent on the dielectric constants of the metal at the incident wavelength. The metals for which this effect will be most pronounced are Ag, Au, Cu, and the alkali metals. A similar model has been developed to account for other geometric shapes of particles and it has been extended to take into account sinusoidal gratings, which again produce enhanced fields via the excitation of surface plasmons [9].

Based on the model of a spherical particle, Creighton [6] was able to develop and elucidate a series of surface selection rules. Since the surface selection rules apply to the polarizability, α , of the molecule, the enhancement effects are incorporated into the selection rules for molecules adsorbed on the surface of a spherical particle. This is expressed as an effective Raman tensor, α_{eff} :

$$\alpha_{\text{eff}} = \frac{9}{(\epsilon_i + 2)(\epsilon_s + 2)} \begin{bmatrix} \alpha_{11} & \alpha_{12} & \epsilon_s \alpha_{13} \\ \alpha_{21} & \alpha_{22} & \epsilon_s \alpha_{23} \\ \epsilon_i \alpha_{31} & \epsilon_i \alpha_{32} & \epsilon_i \epsilon_s \alpha_{33} \end{bmatrix}$$

Since this model refers to the surface of a sphere the subscripts 1 and 2 refer to the directions on the surface and the 3 refers to the direction normal to the surface. The coefficients ϵ_i and ϵ_s are the metal dielectric constants at the incident and scattered frequencies. The most significant result is that the ϵ factor provides a multiplicative factor with respect to the α terms. If $\epsilon_i = \epsilon_s$, there is a selective enhancement of the modes which contain components normal to the surface. The ratio of this selective enhancement becomes:

$$\alpha_{33} : \alpha_{13}, \alpha_{23}, \alpha_{31}, \alpha_{32} : \alpha_{11}, \alpha_{12}, \alpha_{21}, \alpha_{22}, \alpha_{22}$$

is as

$$|\epsilon|^4 : |\epsilon|^2 : 1$$

This selection rule, while derived for a sphere, can be qualitatively applied to a roughened surface. However, since the roughened electrode surface is similar to, but not composed of, isolated metal spheres, it is more a "propensity rule" than a selection rule. Creighton [6] cited several studies in which these rules have been applied to SERS active surfaces.

It is possible to expand the expression for the isolated sphere approach to include a second term. In this case μ is expressed as:

$$\mu = \alpha\mathbf{E} + \frac{1}{3}A\nabla\mathbf{E}$$

The second term is the field gradient term and A transforms in a similar manner to the hyper-polarizability β . A simple interpretation was presented by Sass et al. [24]; if the image charge approach is adopted, it can be assumed that a translation in X causes a translation -X of the image, similarly Y causes a -Y while Z causes a Z. This is analogous to the dipole selection rule mentioned earlier. In the case of the A term, however, each A consists of three XYZ terms. According to Sass et al. [24], if the term does not change sign under transformation then the vibrations that correspond to that term are surface active. If the term does change sign under the transformation then the vibrations are said to be surface inactive. For example, under transformation A_{zzz} :

$$Z \rightarrow Z, Z \rightarrow Z, Z \rightarrow Z.$$

Thus $1 \times 1 \times 1 = 1$ and the sign of A_{ZZZ} does not change; therefore it is surface active. Similarly for A_{XYZ} :

$$X \rightarrow -X, Y \rightarrow -Y, Z \rightarrow Z$$

Thus $-1 \times -1 \times 1 = 1$ and the sign does not change so the vibration is surface active.

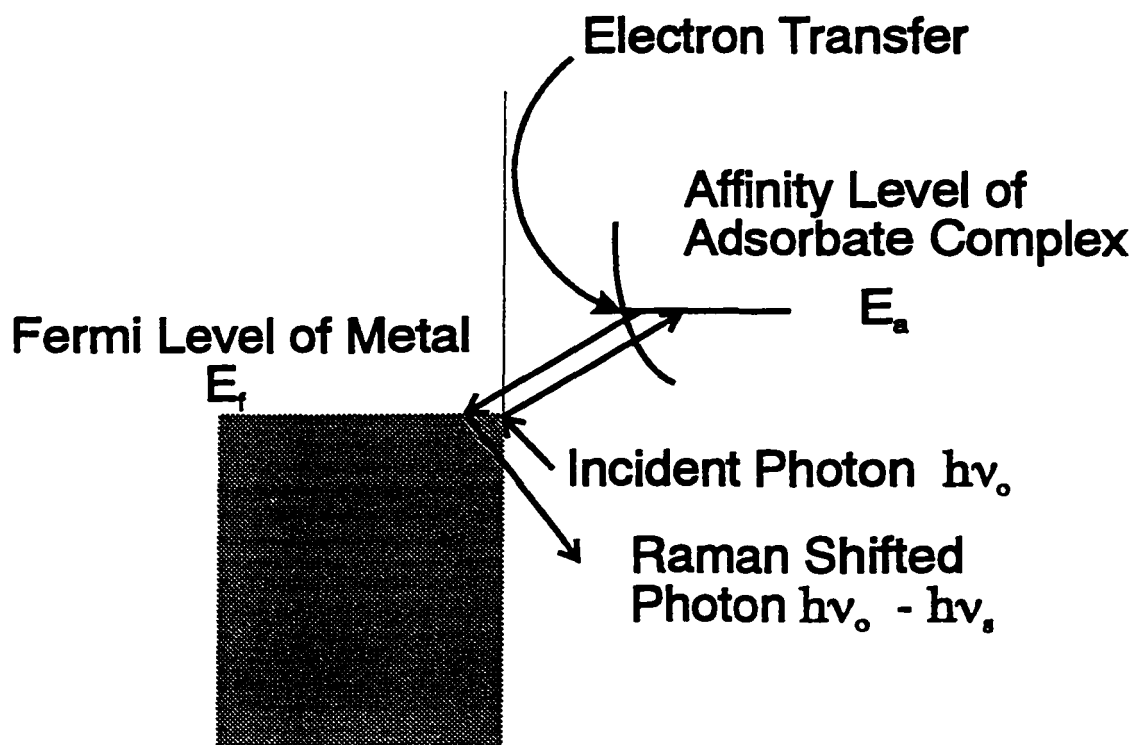
This was used by Sass et al. [24] to explain the appearance of modes of u symmetry of D_{6h} molecules such as benzene. Although u modes are Raman forbidden, they are Hyper-Raman allowed and thus the field gradient mechanism would allow for these modes to become active. Sass et al. [24] felt that this was a better alternative to explain the appearance of Raman inactive modes than the lowering of the symmetry of the molecule during adsorption, since they did not observe any band shifts consistent with the molecule being strongly adsorbed onto the surface. One of the features of the EM mechanism is that it accounts for the fact that only certain metals are SERS active and it takes into consideration the optical properties of the metal. The prediction that enhancement can occur for molecules close to the surface accounts for the observation of SERS from molecules just above the surface.

1.3.2 CT Model

Birke et al. [21] noted that the EM model effectively accounts for a number of the experimental characteristics of SERS such as the requirement of surface roughness, the SERS specificity of certain metals, and the fact that molecules which are not in contact with the surface of the electrode can generate enhanced signals. However, the EM model cannot adequately account for some of the other observations of SERS such as: the differential enhancement of molecules whose gas phase Raman cross sections are the same, such as surface adsorbed CO and N₂; significant preferential enhancement of adsorbates in the "first" layer as opposed to second and subsequent layers; the existence of SERS intensity profiles as a function of electrode potential [21].

Otto et al. [22,23] have presented a chemical enhancement model of SERS based on a charge transfer between the adsorbate and the metal. This model can effectively account for a number of the observations that are not accounted for within the EM model. The CT model involves the creation of an adsorbate-surface complex. This complex results from the interaction of the adsorbate with atomic scale roughness features (i.e., adatoms) on the surface of the metal. This complex can then possess electronic affinity levels which can be accessed by a photo-excited electron. This is shown in Fig. 1.6. The incident photon creates an electron-hole pair. The electron is then excited into

Fig. 1.6: A Schematic Illustration of the CT Mechanism of SERS Enhancement



the affinity level created by the adsorbate surface interaction. The electron then de-excites back into the molecules with the emission of a Raman shifted photon. This is similar in concept to a RRS process. The CT model can account for the first layer enhancement effect as the charge transfer will occur only with molecules on the surface. The variation in observed Raman enhancements observed can be explained by the CT model. Birke et al. [21] noted that, since overtones are not observed in SERS, the charge transfer mechanism must be similar to a B or C term RRS process (referred to as the Herzberg-Teller terms).

Otto et al. [22,23] have introduced a nomenclature for classifying the adsorbate sites into N (Normal) or E (Extra) sites. In their nomenclature N sites are available on atomically smooth surfaces and E sites are not available on these surfaces. The N and E sites are roughly analogous to physisorption and chemisorption. The E sites are thought to be affiliated with the CT SERS process.

Although the CT mechanism invokes RRS like arguments there are some important differences between SERS and RRS. Most significantly the RRS process occurs within the species of interest. Thus one can expect that neither the film thickness nor the substrate roughness will significantly affect the resonance process. The SERS process on the other hand requires specific

adsorbate substrate interactions. The resonance process would no doubt work quite well for films of considerable thickness since it involves an enhancement process that occurs within the molecule of interest. The SERS process on the other hand requires an interaction between the molecule of interest and the electrode surface and can only apply to molecules on the surface, or for EM enhancement, molecules in the vicinity of the surface.

1.3.3 Comparison between EM and CT Models

A number of comparisons and arguments for and against the EM and CT models and their relative importance have been made. Moskovits [25] argued strongly for the EM type models and responded to a number of criticisms of the model. Similarly Otto et al. [23] addressed the criticisms of the CT model. Pettinger [9] noted that there are a number of similarities between the quantum mechanical treatment of the electromagnetic and the electron hole-pair (CT) enhancement models. Both theories may be useful in explaining the different aspects of SERS enhancement which occur under differing experimental conditions.

1.3.4 Comparison between SERS, IR and EELS

As noted previously there are some similarities between Raman, EELS and IR spectroscopy. In general the biggest difference between SERS and all other surface techniques is the requirement of a roughened surface. IR and EELS studies most commonly employ single crystal surfaces and as a result the information obtained from IR and EELS measurements is not always directly compatible with that obtained from SERS measurements. A series of comparisons between EELS and SERS on roughened silver surfaces have been made [26-28]. Gu et al. [28] concluded that EELS and SERS probe different sites and EELS seemed to be more globally sensitive to the adsorbate on the surface whereas SERS seemed to probe fewer, but more chemically reactive sites.

The fundamental problem in the application of EELS to the electrochemical system is the requirement that it be performed under UHV conditions. Wagner [29] addresses this concern by showing that a number of systems which resemble an electrified interface can be observed in and simulated under UHV conditions.

The use of SERS is limited as well, as it requires that several experimental conditions exist. Since SERS has a wavelength specific

component it is necessary to obtain SERS from Cu and Au surfaces with red excitation, whereas for Ag surfaces green or red excitation can be used. Since the most intense SERS spectra are observed on Ag, Cu, and Au, it is these systems that are most commonly studied.

The most crucial experimental perturbation is the requirement that the surface be roughened in order to observe SERS. The most common method of roughening an electrode surface is through the use of one or more Oxidation Reduction Cycles (ORCs). A typical ORC consists of stepping or sweeping the potential to a desired anodic limit, to form a solution or surface oxidized species, and then stepping the potential to a negative value to reduce it, resulting in the deposition of metal. It has been observed that the roughening procedure can result in the oxidation and/or reduction of the species of interest [30,31]. Brolo et. al. [32] demonstrated that surface morphology has a direct relationship to the intensity of SERS. Surface roughness features of about 100 nm were optimum for gold electrodes when using 650 nm excitation. The roughening of the surface makes quantification of SERS experiments considerably more difficult and the effect of creating a rough surface must be taken into account in any analysis of SERS data.

1.4 Carbon Dioxide Equilibria

When a gas is dissolved in aqueous solutions an equilibrium can be established between the solution and gas phase species. For example:



The concentration of the species in solution is proportional to the partial pressure of the gas phase species, as stated by Henry's Law:

$$[\text{N}_2] = K_{\text{H}} P_{\text{N}_2}$$

These solution concentrations are usually quite small. For example at 298 K and 1 atm. of pressure $[\text{N}_2] = 6.61 \times 10^{-4}$ M and $[\text{CO}] = 9.55 \times 10^{-4}$ M. For CO_2 the behaviour governed by Henry's Law is complicated by the equilibria that are established between CO_2 and carbonate solution species:



The equilibrium concentration of H_2CO_3 is approximately 10^{-3} times smaller than that of CO_2 and thus it can be incorporated into a $\text{CO}_2(\text{aq})$ term in the equilibrium. For a system under a constant pressure of CO_2 ("open"), the following equilibrium relationships will apply [33]:

$$[\text{CO}_2(\text{aq})] = K_H P_{\text{CO}_2} \quad K_H = 10^{-1.5}$$

$$\frac{[\text{H}^+][\text{HCO}_3^-]}{[\text{CO}_2(\text{aq})]} = K_1 \quad K_1 = 10^{-6.3}$$

$$\frac{[\text{H}^+][\text{CO}_3^{2-}]}{[\text{HCO}_3^-]} = K_2 \quad K_2 = 10^{-10.3}$$

Thus for a given P_{CO_2} , the concentration of $[\text{CO}_3^{2-}]$, $[\text{HCO}_3^-]$ and $[\text{CO}_2(\text{aq})]$ can be calculated as a function of $[\text{H}^+]$. These data can be plotted as the log of the concentration verses pH yielding an "equiligraph". Figure 1.7 shows an equiligraph for the open system, $P_{\text{CO}_2} = 1 \text{ atm}$.

It is also possible to establish the equilibrium conditions for a "closed" system, in which the total carbonate content is fixed. In this case the equiligraph can be constructed using the following relationships [33]:

$$C_T = [\text{CO}_2(\text{aq})] + [\text{HCO}_3^-] + [\text{CO}_3^{2-}]$$

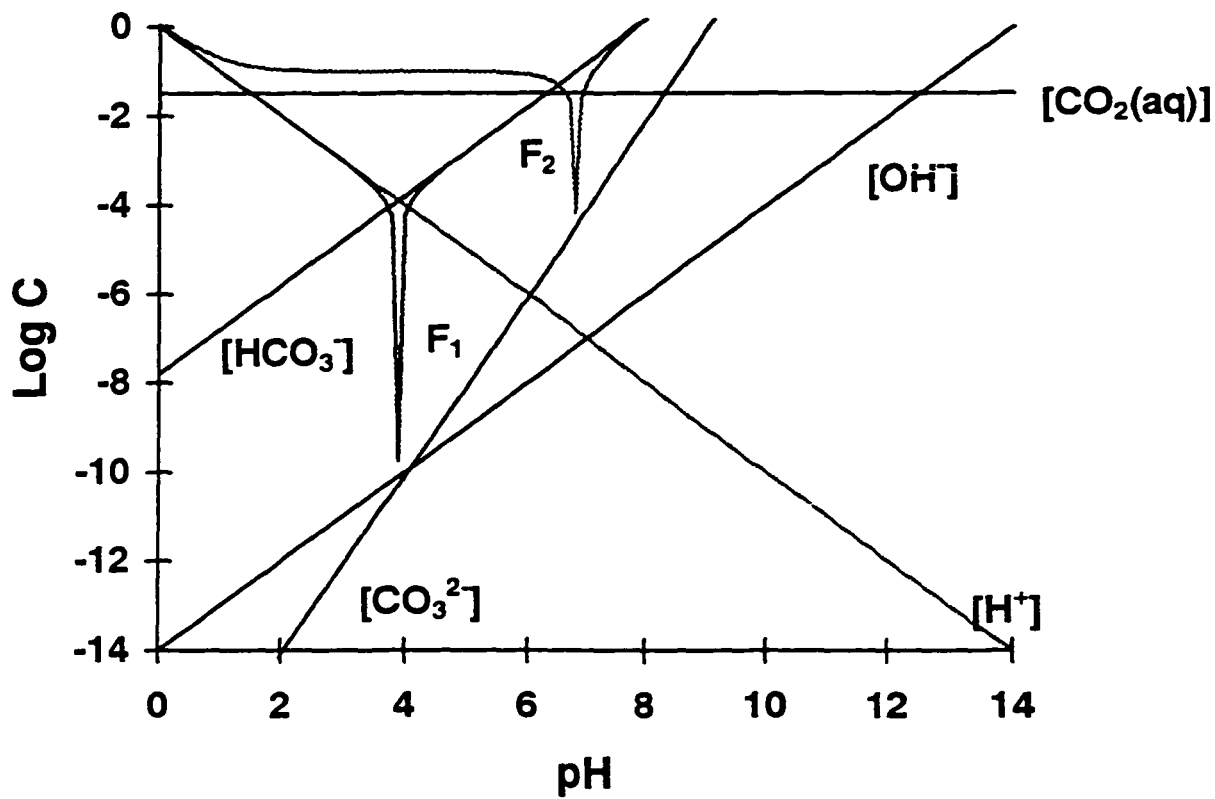
and

$$[\text{CO}_2(\text{aq})] = \frac{[\text{H}^+]^2 C_T}{D}$$

$$[\text{HCO}_3^-] = \frac{[\text{H}^+] K_1}{D}$$

$$[\text{CO}_3^{2-}] = \frac{K_1 K_2}{D}$$

Fig. 1.7: An Equilligraph for an Open Carbonate System at $P_{\text{CO}_2} = 1 \text{ atm}$.



$D = ([H^+]^2 + [H^+] K_1 + K_1 K_2)$ and the K_1 and K_2 values are the same as for the "open" system. Figure 1.8 shows an equiligraph for the system where $C_T = 0.1$ M.

An equiligraph can be used to determine the pH of solutions. This can be done by using Freiser's "pointer function" [34]. The pointer function utilizes the fact that in a spreadsheet a significant quantity of data can be rapidly calculated and used to find the pH of the system. For example:

$$P = 1 \text{ atm for CO}_2 \text{ in H}_2\text{O (open system)}$$

In this case the overall charge balance is:

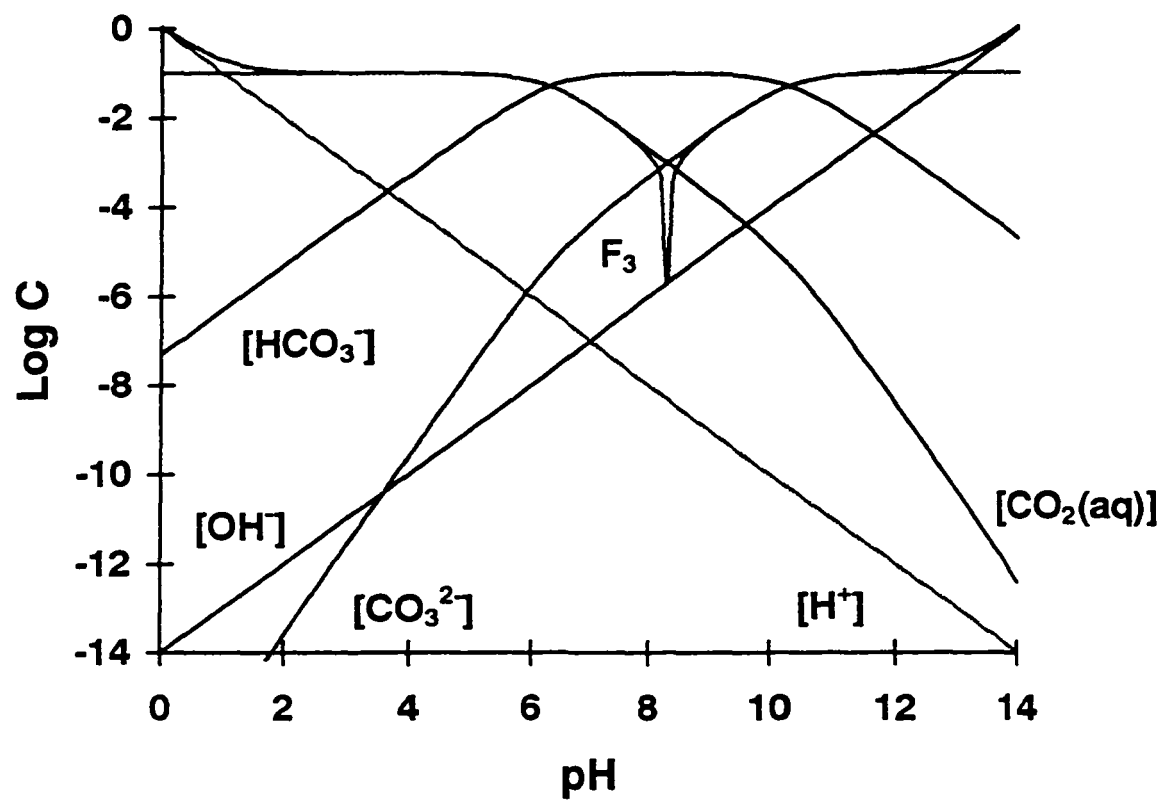
$$[H^+] = [HCO_3^-] + 2 [CO_3^{2-}] + [OH^-]$$

Since this equation is true at only one pH, a new function can be defined as:

$$f = [HCO_3^-] + 2 [CO_3^{2-}] + [OH^-] - [H^+]$$

At the pH of the solution $f = 0$. Since the f curve is continuous and $f = 0$ is the point at which the function changes from positive to negative, a log function can be used to find the pH. If $F = \log |f|$ is plotted, a sharp "point" will occur

Fig. 1.8: An Equiligraph for a Closed System $C_T = 0.1 \text{ M}$



where $f = 0$, due to the absolute value in the equation. If this is plotted on the equiligraph, the pH can be read directly from the graph or taken from the calculated values of F . Thus for CO_2 in H_2O :

$$F_1 = \text{Log} | [\text{HCO}_3^-] + 2 [\text{CO}_3^{2-}] + [\text{OH}^-] - [\text{H}^+] |$$

When this is plotted against pH on the equiligraph, a point appears at $\text{pH} = 3.8$ which is the pH of the solution. The advantage of this function is that it can be used for more complex problems as well. For 0.1 M of NaHCO_3 saturated with CO_2 at $P_{\text{CO}_2} = 1 \text{ atm}$ the overall charge balance becomes:

$$[\text{Na}^+] + [\text{H}^+] = [\text{HCO}_3^-] + 2 [\text{CO}_3^{2-}] + [\text{OH}^-]$$

$$F_2 = \text{Log} | [\text{HCO}_3^-] + 2 [\text{CO}_3^{2-}] + [\text{OH}^-] - [\text{Na}^+] - [\text{H}^+] |$$

The pH for this system is 6.8 as shown in Fig. 1.7. For the closed system of 0.1 M NaHCO_3 , shown in Fig. 1.8, the overall charge balance will be the same. The pointer function, F_3 , will also be the same; thus the pH is 8.3.

If this system is opened to a gas other than CO_2 , the $\text{CO}_{2(\text{aq})}$ will be purged from the system in order to maintain the Henry's Law equilibrium. This will result in a shift in the carbonate equilibrium to replace the lost $\text{CO}_{2(\text{aq})}$ and a lowering of the C_T due to a loss of carbonate species. Since C_T is

reduced and $[\text{Na}^+]$ remains the same, the pH of the system will rise as the overall charge balance is maintained. This is demonstrated in Fig. 1.9 and 1.10. In each instance the overall C_T has been reduced while the $[\text{Na}^+]$ is fixed at 0.1 M. Using the pointer function results in the equation:

$$F_4 = \text{Log} | [\text{HCO}_3^-] + 2 [\text{CO}_3^{2-}] + [\text{OH}^-] - [\text{H}^+] - 0.1 |$$

Figure 1.9 represents $C_T = 0.09$ M or 90% of the original NaHCO_3 concentration and based on the above function the pH is 9.4. Figure 1.10 represents a reduction of C_T to 75% of the original NaHCO_3 concentration, resulting in a pH of 10. From these figures it can be seen that the pH of a solution saturated with another gas such as N_2 or CO will increase over time. Although the depletion of carbonate species will be a slow process, it is apparent that opening the system to an atmosphere which contains no CO_2 will increase the pH of the system over time.

By knowing the pH of the system it is possible to determine the extent of the dissolution of the CO_2 . In acidic solutions the predominant species is aqueous CO_2 whereas the bicarbonate and carbonate species dominate as the solution pH increases. From these data, it has been demonstrated that solutions continuously saturated with CO_2 will behave differently than those exposed to other gases.

Fig. 1.9: An Equiligraph of a Closed System after C_T is Reduced to 0.09 M

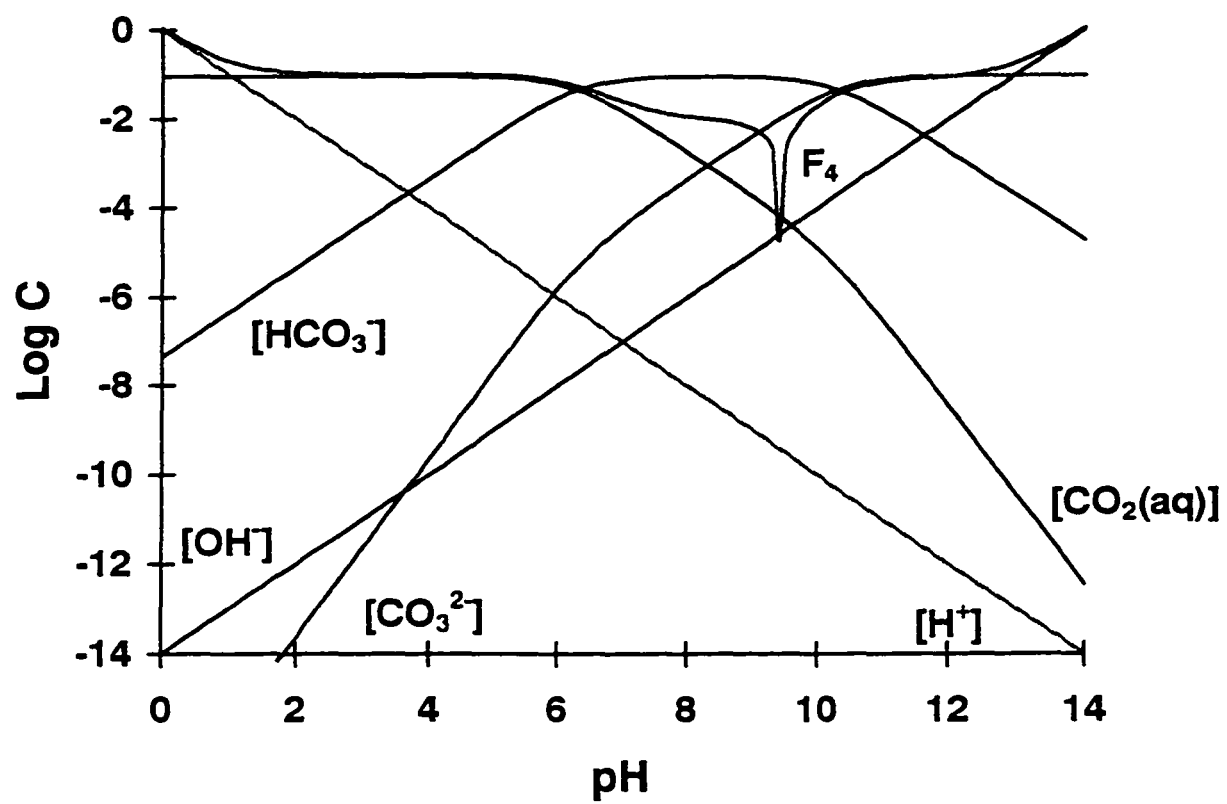
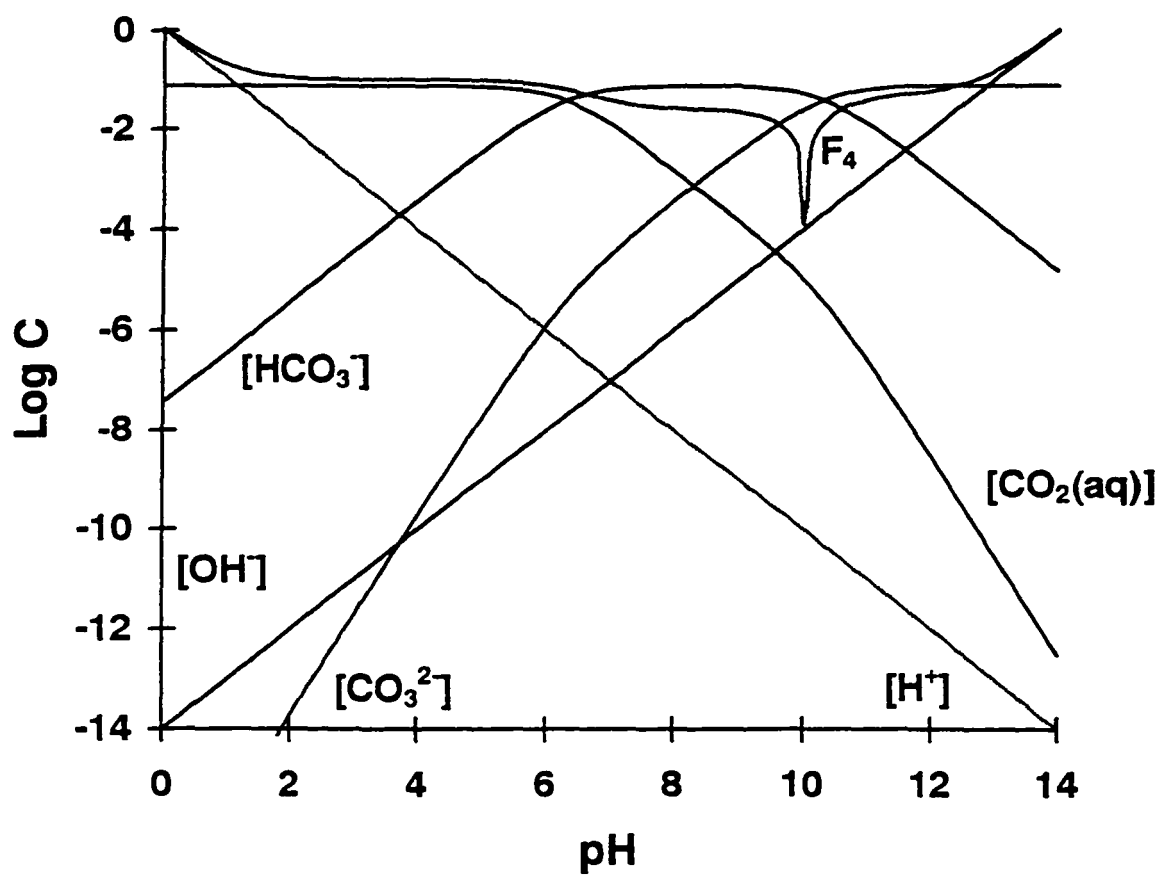


Fig. 1.10: An Equiligraph of a Closed System after C_T is Reduced to 0.075 M

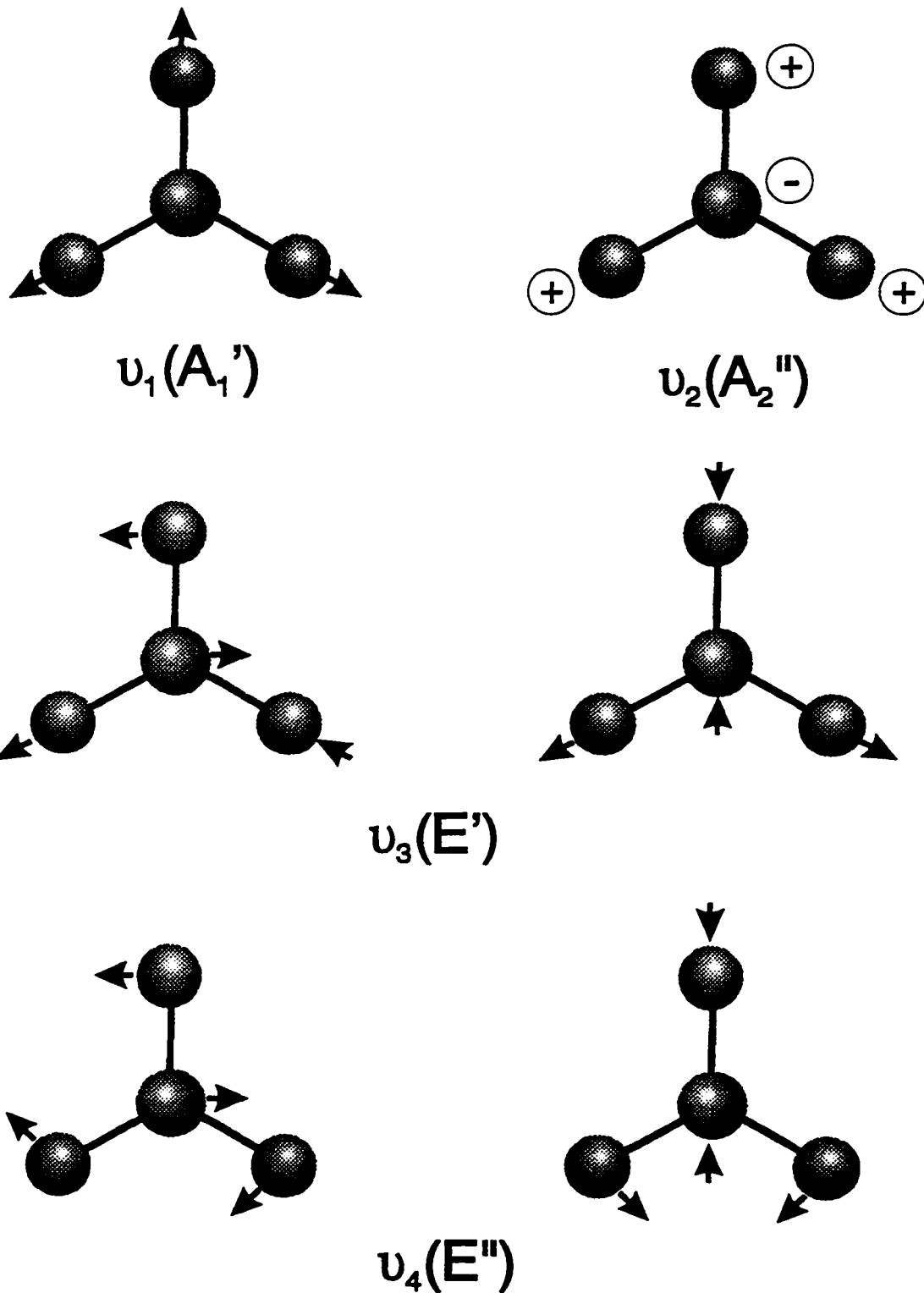


1.4.1 Vibrational Spectroscopy of CO₂/H₂O

Davis and Oliver [35] studied the CO₂/H₂O system using both IR and Raman spectroscopy. For the purpose of band assignment a Raman spectrum of gaseous CO₂ at 5 atm was collected. Bands were observed at 1266, 1286, 1390, and 1411 cm⁻¹ for gaseous CO₂. They stated that these results compared favourably to the results reported by Herzberg [36]. For CO₂ dissolved in H₂O at P_{CO₂} = 5 atm. [CO_{2(aq)}] = ca. 0.17 M, Davis and Oliver [35] observed two bands at 1276 and 1384 cm⁻¹. These bands were assigned to the Fermi resonance doublet observed for 2ν₂ and ν₁ of CO₂. They concluded that since no bands attributable to other species were observed, the predominant solution species was CO₂, not H₂CO₃. Thus CO₂ was essentially unperturbed and maintained its D_{∞h} symmetry.

Davis and Oliver [35] also studied 3.5 M KHCO₃ solutions and observed a number of bands, which were assigned based on C_s point group symmetry. It was observed that by increasing the pH, the conversion of bicarbonate into carbonate could be quantitatively measured. The carbonate ion, in an 8 M solution of K₂CO₃, was studied as well. An isolated carbonate ion, as illustrated in Fig. 1.11, is expected to have D_{3h} symmetry and 4 fundamental vibrational modes: ν₁(A₁') - Raman active and IR inactive; ν₂(A₂') - IR active and Raman inactive; ν₃(E'') and ν₄(E') - both Raman and IR active. However,

Fig. 1.11: An Illustration of the Vibrational Modes of a Planar Triangular Molecule (D_{3h}), e.g., CO_3^{2-}



they were able to observe bands from the ν_1 and ν_2 modes in both the IR and Raman spectra of 8 M K_2CO_3 . In both the IR and Raman spectra of this solution, the band from the $\nu_3(\text{E}'')$ mode was split into two components. They felt that the splitting of the band from the $\nu_3(\text{E}'')$ mode was caused by an environmental effect in the solution phase. They did not see a splitting of the band from the $\nu_4(\text{E}')$ mode. They suggested that the appearance of IR and Raman forbidden bands was due to a slight distortion of the D_{3h} symmetry in the solution combined with cation interactions.

For comparison purposes, spectra of 2 M KHCO_3 , 2 M K_2CO_3 and 0.1 M NaOH solutions were run. Table 1.2 compares these results with those observed by Davis and Oliver [35]. For the 2 M K_2CO_3 , no band at ca. 880 cm^{-1} ($\nu_2(\text{A}'')$) was observed. The differences may be related to the CO_3^{2-} concentration, since a 2 M solution was used, compared to Davis and Oliver who used 3.5 M KHCO_3 and 8 M K_2CO_3 . The observation of the ν_1 mode of CO_3^{2-} in the 2 M KHCO_3 solution is consistent with the findings of Davis and Oliver. The observation of a weak HCO_3^- shoulder at 1018 cm^{-1} in 2 M K_2CO_3 solution was not reported by Davis and Oliver.

Table 1.2: Band Assignments for HCO_3^- and CO_3^{2-} in H_2O

KHCO_3 3.5 M [35] Raman	KHCO_3 3.5 M [35] IR	KHCO_3 2 M Raman	NaHCO_3 0.1 M Raman	Species/Vibrational Description [35]
632		635		$\nu_7(\text{A}')(\text{OH})\text{CO}$ bend
672		674		$\nu_8(\text{A}')\text{CO}_2$ bend
841	840			$\nu_8(\text{A}'')\text{CO}_3$ op deformation
1017	1000	1017	1017	$\nu_5(\text{A}')\text{C-OH}$ stretch
1064	1064	1064		$\nu_1(\text{A}_1')\text{CO}_3^{2-}$ in solution
1302	1300	1307		$\nu_4(\text{A}')\text{COH}$ bend
1360	1355	1360	1360	$\nu_3(\text{A}')\text{sym. CO}$ stretch
1630	1620			$\nu_2(\text{A}')\text{asym. CO}$ stretch
1684				$(2\nu_8)(\text{A}')$
2650	2620	2648		$\nu_1(\text{A}')\text{OH}$ stretch

op = out-of-plane, sym. = symmetric, asym. = asymmetric

K_2CO_3 8 M [35] Raman	K_2CO_3 8 M [35] IR	K_2CO_3 2 M Raman	Assignment [35]
684		683	$\nu_4(\text{E}')$
880	880		$\nu_2(\text{A}_2'')$
		1018	$\nu_5(\text{A}')\text{C-OH}$ stretch*
1064	1056	1062	$\nu_1(\text{A}_1')$
1380	~1375	1364	$\nu_3(\text{E}')$
1436	~1430	1418	$\nu_3(\text{E}')$
1761			$2\nu_2(\text{A}_2'')$

* from HCO_3^{2-} in solution

1.5 Electrochemical Reduction of CO₂

Electrochemical reduction occurs when electrons are transferred, thereby reducing the oxidation state of an atom in the species. It has been observed that the electrochemical reduction of CO₂ can result in several different products. Table 1.3 lists the standard electrode potentials (E°) values for a number of possible reduction products from CO₂. All of these are possible species which need to be considered to understand the mechanism of CO₂ reduction in the electrochemical environment, even though not all are produced in any specific electrochemical reduction.

The most complete reductions are also the most thermodynamically favourable; CH₄ is the most favourable. Since it is unlikely that any process would involve the simultaneous transfer of 8 electrons, a number of intermediate steps have been proposed for the mechanism of CO₂ reduction. These require a very large negative overpotential. In fact the E° values for the formation of the postulated CO₂^{•-} radical ion are estimated to be -1.85 or -1.90 V (NHE) [37]. Hori et al. [38] have proposed a mechanism for the electrochemical reduction of CO₂. Figure 1.12 illustrates this proposed mechanism on Ag, Au, Cu, and Zn surfaces.

Table 1.3: Equilibrium Electrochemical Potentials (E°) for Possible CO_2 Reduction Products [37]

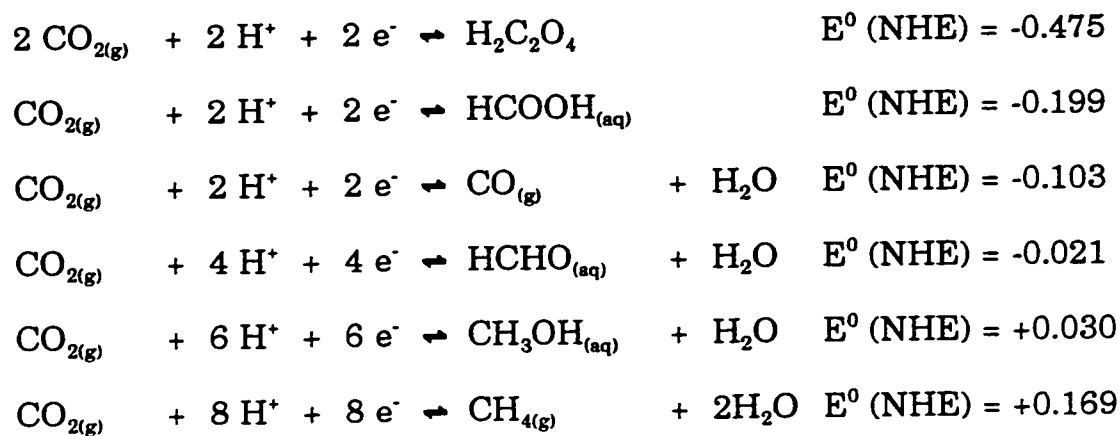
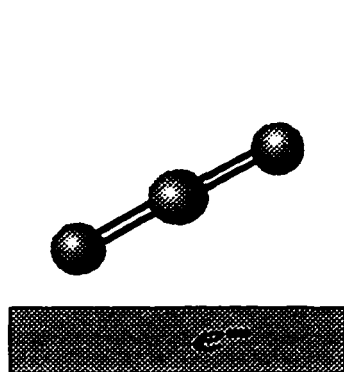
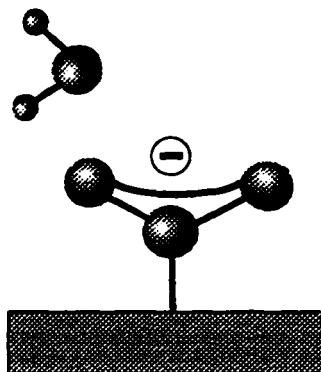


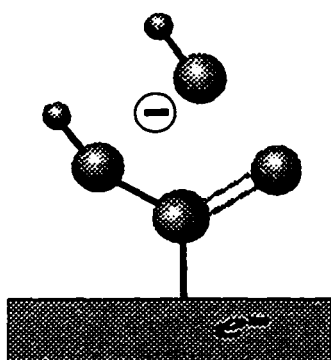
Fig. 1.12: The Proposed Mechanism for CO₂ Reduction on Ag, Au, Cu, and Zn Surfaces



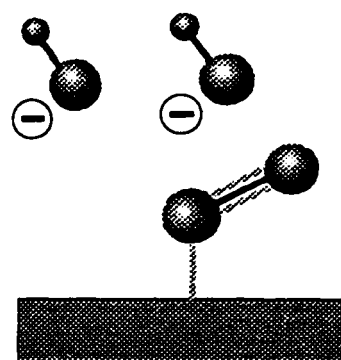
① CO₂ Accepts an Electron



② Intermediate is Protonated



③ Intermediate is Further Reduced



④ CO is Produced

In the case of Ag, Au, Cu, and Zn, the formation of a bent $\text{CO}_2^{\cdot-}$ radical ion occurs as the first step, when the CO_2 molecule accepts an electron. In the second step, this intermediate species is firmly attached to the electrode surface and the oxygen is protonated. In the third step, the intermediate species is further reduced as an electron is transferred to the COOH species. In the fourth step, CO is produced when an OH^- ion is released into solution. It has been observed that this CO can be further reduced on copper electrodes to various hydrocarbon species [39]. On the surface of other metals (eg. Hg) where the $\text{CO}_2^{\cdot-}$ is not strongly held it is proposed that the carbon atom acquires a proton resulting in the formation of a formate species [38]. The solvent system can also make a difference. For example it has been observed that oxalate species can be found as CO_2 reduction products in aprotic solvents. This has been ascribed to a coupling of the two $\text{CO}_2^{\cdot-}$ species in the absence of protons [37].

Chapter 2

Experimental Background

2.0 Scope

This chapter will describe the chemicals, cell design, and instruments used in the experiments. Initial experiments were performed on a Dilor OMARS 89 Raman Spectrometer. The arrival of a new Raman Spectrometer, a Renishaw System 1000 Raman Microscope, allowed for greater sensitivity and collection of better quality data. This chapter will describe and provide a comparison between these instruments.

2.1 Chemicals

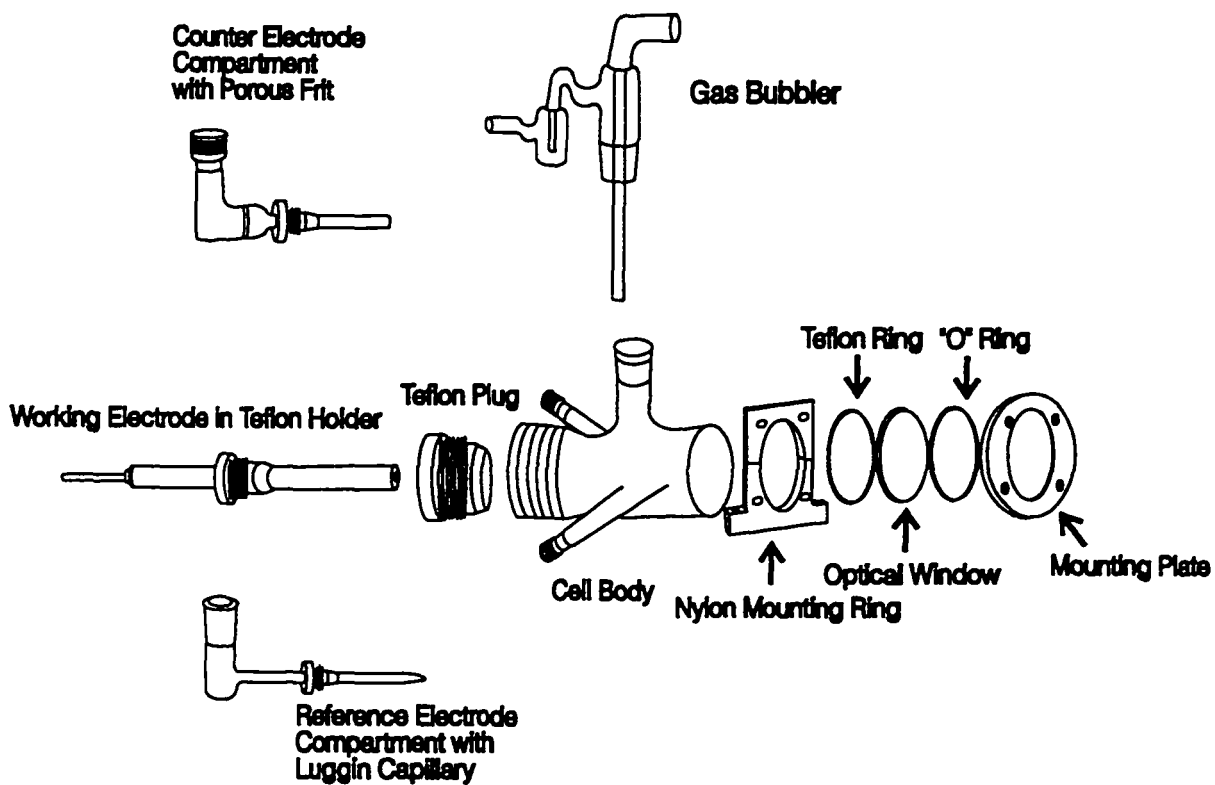
All chemicals used for the experiments were of reagent grade. The NaHCO_3 (BDH) and KHCO_3 (Fisher) were used as received without further purification. The CO , CO_2 , and N_2 (Linde/Praxair) were used without further purification. All solutions were prepared from Milli-Q water. KDCO_3 was synthesised by adding dry ice to a 5 M solution of K_2CO_3 (Baker) in D_2O (99.9% Cambridge). The precipitate was collected and washed with D_2O and stored in a desiccator. The Raman spectrum of the resultant material was taken and it compared favourably with the literature [40]. The electrodes were made from high purity Johnson Matthey copper rod.

2.2 Cell Design

In order to observe SERS it is necessary to design and construct a cell which combines good electrochemical and spectroscopic performance. Often the design criteria must be constrained by the nature and location of the spectrometer's collection and focusing optics. The electrochemical cell designed for these experiments can be used to observe systems in a conventional arrangement where the focusing and collection optics are in a plane parallel to the floor (the XY plane) and at 90° to each other. It has also been possible to use this cell with a 180° back-scattering geometry where the collection and focusing optics are the same, and normal to the surface. Although each glass cell will be slightly different when glass-blown, it is possible to construct readily interchangeable cells that allow several experiments to be carried out with a minimum of realignment work. The cell can be mounted in a standardized mounting ring. This ring can then be mounted on an XY translation stage (Optikon) and a rotation stage to allow for full rotation in the XY plane (Kinetic Systems). A tilt stage is provided (Kinetic Systems) along with a vertical (Z translation) adjustment stage (in-house). This allows for the angle of incident between the electrode and laser beam to be reproducibly set.

The body of the cell (Fig. 2.1) was formed from a 25 mm threaded Ace Glass connector; two 7 mm Ace Glass connectors were glass-blown onto the

Fig. 2.1: A Diagram of the Spectroelectrochemical Cell Used for SERS Experiments



sides to allow insertion of a Luggin capillary and a counter electrode. A 19/26 ground glass joint was fused to the top of the cell to allow for a gas bubbler, used for purging the cell. The cell was fitted with Teflon plugs and ferrules so that components could be easily attached and removed. Since the windows are only 3 mm thick, attaching them using glass-blowing techniques would distort them and attaching them using an epoxy adhesive introduces the risk of contaminating the electrolyte solutions. To avoid these two problems the cell window was attached with a specially designed plate which made a tight seal. The seal was achieved by placing a thin Teflon washer and a rubber O-ring seal on either side of the optical window. This ensured that the glass was not broken by the pressure applied by the screws, and only the Teflon seal was in contact with the solution.

The counter electrode was isolated from the main solution by a porous frit and the reference electrode was connected via a Luggin capillary tube. Epoxy cements were not used to seal the electrode into the Teflon holder because they would introduce the possibility of contamination when polishing and cleaning the electrode. Electrodes that are set into Teflon by heating still have gaps between the electrode and the holder which can trap solution. In both cases the electrode is not removable from the Teflon, making it impossible to clean. In order to overcome these problems the electrode and holder were machined so that the electrode could slide snugly in and out of the holder.

Although this arrangement did not prevent leakage of the solution around the sides of the electrode it allowed the electrode to be removed for cleaning. A brass rod was screwed into the back of the electrode in order to provide electrical contact. The portion of the brass rod inside of the holder which was not connected inside the electrode was covered in Teflon tape to help prevent it from reacting with any solution that might migrate past the sides of the electrode. The electrode was then threaded into the back of a 25 mm Teflon plug and mounted in the cell.

2.3 Electrochemical Instrumentation

All electrochemical experiments were performed using an EG&G PAR 273 potentiostat. Electrochemical data were collected/displayed via a Kipp and Zonen XYY' chart recorder, a comscope data acquisition board, or via a computer connected to the IEEE488 port of the potentiostat. All electrode potentials were measured relative to the Saturated Calomel Electrode (SCE) potential, but are quoted versus the Normal Hydrogen Electrode (NHE) scale where:

$$E_{\text{NHE}} = E_{\text{SCE}} - 0.24 \text{ V.}$$

2.3.1 Electrode Pretreatment

Copper electrodes were prepared by mechanically polishing the electrode with extra fine emery paper (Tech Met) and 0.5 μm alumina powder (Micro Metallurgica) slurry. The electrode was then rinsed in Milli-Q water and ultrasonically cleaned. The final surface preparation consisted of an anodic cleaning in 85% H_3PO_4 which removed any residual oxide layer. This cleaning did not polish the electrode, but instead it produced a surface that had a uniformly etched appearance. Since the subsequent SERS experiments involved roughening of the electrode the initial surface roughness is not as important a factor as the initial surface cleanliness. The electrode was then rinsed and transferred to the electrochemical cell, where the appropriate gas was bubbled through the cell at Open Circuit Potential (OCP).

2.3.3 Preparation of a SERS Active Surface

In order to observe SERS it is necessary to roughen the electrode; the surface features must be a suitable size and shape in order to produce good SERS. As a result it is necessary to experiment with the electrochemical pretreatment conditions of the oxidation reduction cycles (ORCs) to achieve the desired level of enhancement.

SERS active surfaces are commonly created using a halide electrolyte (e.g., KCl, KBr, NaCl, etc.). A halide film is formed during the anodic sweep and decomposed during the cathodic sweep of the ORC resulting in the deposition of metal atoms. This creates the SERS active surface. For copper, the use of halide electrolytes, such as KCl, have been shown to result in the creation of SERS active surfaces which have great temporal stability, even at very negative potentials [41]. In fact chloride environments have been shown to be so aggressive that a SERS active surface can be created at OCP through localised corrosion and redeposition of copper [42]. If halide media are used to generate SERS active surfaces, the SERS of both adsorbed halide and water coadsorbed with the halide can be observed readily. This was demonstrated by Oda et al. who used 3.5 M KCl to observe SERS of CO₂ reduction products on Cu and Ag electrodes [43].

Although the halide environments yield excellent SERS, creating SERS sites without the use of this type of electrolyte is desirable in order to correlate the spectroscopic data with electrochemical data obtained in non-halide environments. In the course of this research all of the SERS active surfaces were created without using halides for roughening. The specific roughening procedures and the results obtained will be discussed in conjunction with the experimental results.

2.4 Spectroscopic Instrumentation

During the course of this research two different spectrometers were used. This section will describe both systems and compare these two instruments. The Dilor OMARS 89 Spectrometer was used for experiments performed during the first three years of this research. This has since been superseded by a Renishaw System 1000 Raman Microscope. Due to the greater sensitivity of the Renishaw instrument many of the experiments were re-done on this instrument. Unless otherwise noted spectra shown are from the Renishaw System 1000 Raman Microscope. All spectra have been baseline corrected and peak areas determined by curve resolution.

2.4.1 Dilor OMARS 89 Raman Spectrometer

In the Dilor OMARS 89 Raman Spectrometer the Raman scattering is collected by a 50 mm lens at 90° to the incident laser. This allows the angle of incidence of the laser on the electrode to be varied considerably which can be useful in the study of SERS [44,45]. The scattered light enters a conventional double monochromator which is adjusted to send a broad band pass (~600 - 700 cm^{-1}) to the spectrograph. The spectrograph disperses this bandpass over the 512 channel intensified photodiode array (IPDA) which enables the recording of a region of about 500 cm^{-1} wide with green excitation and about

200 - 250 cm^{-1} with red excitation. This improves the sensitivity of the instrument since it is possible to collect and add many spectra, yielding an increased signal-to-noise ratio.

As only a 200 - 500 cm^{-1} region can be obtained on a single spectrum, it is necessary to collect between eight and twenty spectra in order to study the region from 50 to 4000 cm^{-1} . To obtain a complete spectrum each spectral range has to be baseline aligned to the adjacent ones, making comparisons between spectral ranges more difficult. As well, a considerable length of time is needed to collect this number of separate spectra.

As the Dilor uses a monochromator to remove Rayleigh scattering it can use any excitation source to collect spectra. A CR599 dye laser with DCM dye was used for the copper experiments. However, the monochromator suffers from a red limit that restricts the use of red excitation. The grating cannot be adjusted to send radiation below 13000 cm^{-1} to the detector. In order to study CO_2 reduction on copper the lowest energy excitation that can be used and still allow for the possibility of observing the Raman spectra from CH species (ca. 2900 cm^{-1}) is about 620 nm ($\sim 16000 \text{ cm}^{-1}$). This wavelength is troublesome as it is not long enough to provide good SERS intensity for Au and Cu [46,47]; it is at the blue limit for SERS on these metals. This wavelength is also at the blue limit for the DCM dye used in the CR599 dye laser. This reduces the

power available, thus reducing the scattering intensity. Thus this instrument is problematic for studying spectral features on Au and Cu above 2000 cm^{-1} .

2.4.2 Renishaw 1000 Raman Spectrometer

The Renishaw 1000 Raman Spectrometer uses a dedicated microscope system to focus the incident laser and collect the Raman scattering. This has been adapted to examine macroscopic samples. In this case the microscope objective is replaced by a mirror and a lens which deflects the beam by 90° so that it can be focused on a sample in a conventional cell or cuvette. This allows the electrochemical cell described earlier to be used. This configuration requires that the spectra be collected using a 180° back-scattering geometry along the electrode surface normal. Unfortunately this is not the ideal angle for SERS studies [21] and is problematic for conventional Surface Raman studies [5] since the electric field at the surface consists of only tangential components.

The scattered light is collected back through the microscope and two holographic notch filters are used to remove Rayleigh scattering. These filters are specific to the wavelength of the incident light and thus lasers with specific wavelengths are required. A Melles Griot HeNe laser (632.8 nm) was used as the excitation source. The HeNe laser is an ideal excitation source for SERS

spectra from both Cu and Au electrodes. The spectrometer can also accommodate an Ar⁺ laser as an excitation source. However, this has not yet been installed.

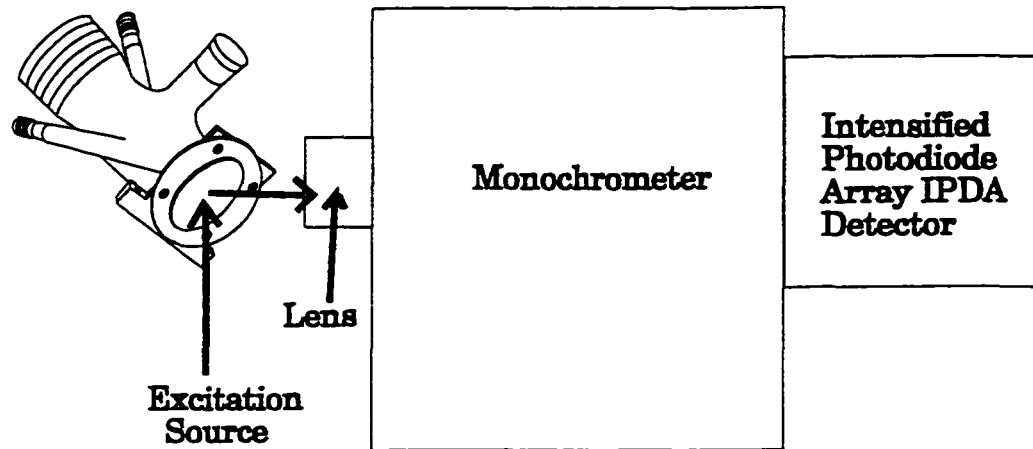
An extended scan mode can be used; the grating is moved so that the spectrum is scanned across the Charge Coupled Device (CCD) detector where the spectrum is recorded and accumulated. This allows the acquisition of a spectrum from 50 - 4000 cm⁻¹ at one time and permits easy comparison of features in different spectral regions. A fixed mode is available in which the grating is fixed so that about a 600 cm⁻¹ region, using red excitation, is collected.

2.4.3 Spectrometer Comparison

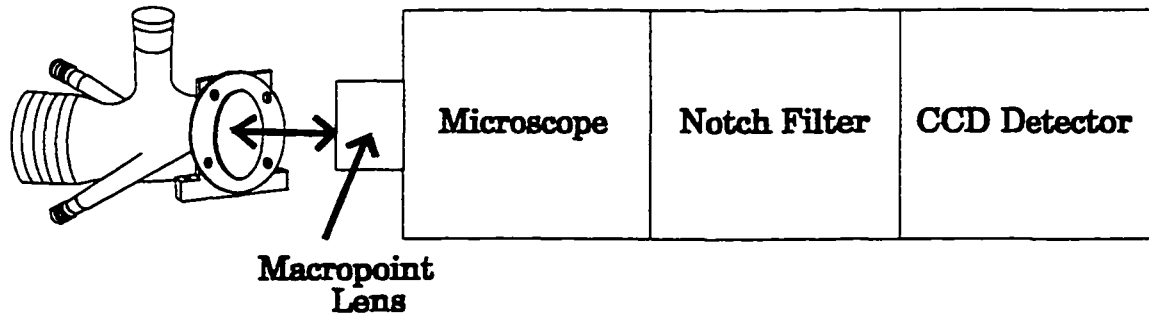
For comparison Fig. 2.2 shows a block diagram of both the Dilor and the Renishaw Raman spectrometers. The biggest advantage of the Dilor over the Renishaw is that the angle of incidence of the exciting light can be varied allowing for optimal SERS effects and the possible use of the Dilor in a variety of Raman scattering geometries. The Dilor also has a slightly better system for collecting scattering from macroscopic systems as it avoids the unnecessary use of a microscope.

Fig. 2.2: A Block Diagram Comparing the Renishaw and Dilor Instruments

Dilor



Renishaw

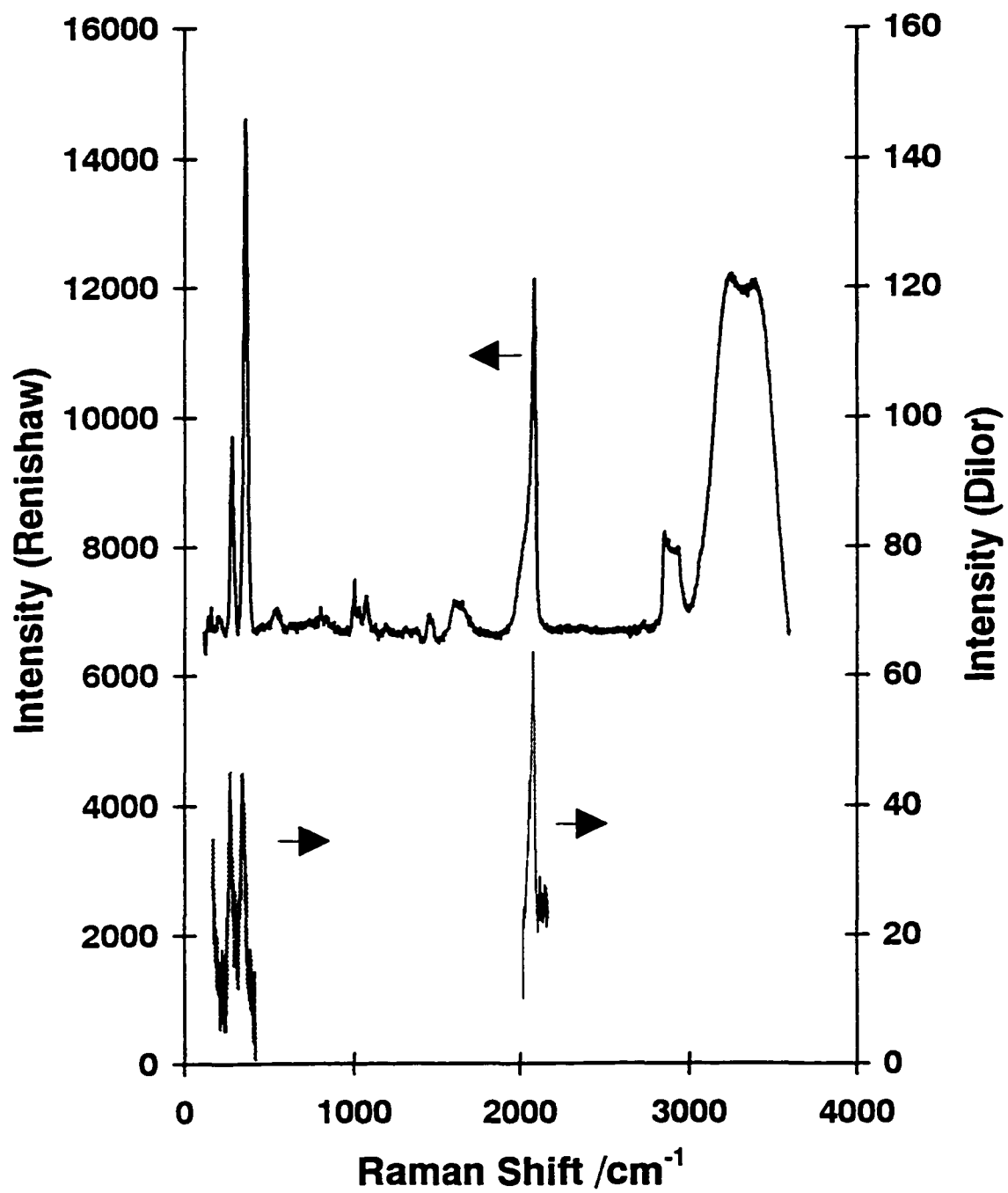


Since the Renishaw uses a holographic notch filter system to remove the Rayleigh scattering, the throughput is about 90% [16] compared to about 10% for a conventional monochromator system [5], which is used in the Dilor. As well the Renishaw's CCD detector is about 50 - 70% efficient [16] compared to the Dilor's IPDA system which is at most about 30% efficient [5]. Thus the Renishaw is able to detect and accumulate significantly more Raman scattering, making it a much more sensitive instrument. Since the Renishaw uses a HeNe laser which operates at 632.8 nm, it functions at an ideal wavelength for utilizing SERS to study Au and Cu surfaces [46,47].

An advantage of the Renishaw instrument is the ability to use the extended mode to collect large spectral regions. This allows for easier comparison between spectral regions separated by more than 500 cm^{-1} , which is the maximum that can be observed in a single spectrum on the Dilor instrument. As well, it takes less time to accumulate one spectrum covering the entire spectral range than it takes to accumulate as many as twenty individual ones.

Figure 2.3 shows the spectra of adsorbed CO on copper at -1.26 V obtained from the Renishaw and Dilor instruments. For the Dilor, the excitation power was ca. 100 mW at 619 nm (ca. 60 mW at the sample) and the sample position was optimized (ca. 63°) to get the best possible signal. For the

Fig. 2.3: A Comparison of the Modes of Adsorbed CO on Copper at -1.26 V between the Renishaw and Dilor Instruments



Renishaw the excitation power was ca. 35 mW at 632.8 nm (ca. 5 mW at the sample) and 180° back-scattering geometry was used. Although the intensity numbers in Figure 2.3 are not directly comparable, it is apparent that the Renishaw has a much greater signal-to-noise ratio than the Dilor and the sensitivity of the Renishaw instrument far outweighs the geometry/positioning capability advantage of the Dilor. As well the Dilor spectra required two separate accumulations to be able to observe the bands of adsorbed CO. In order to observe the entire spectral region between 50 and 4000 cm^{-1} using the Dilor, 18 additional spectra would have to be accumulated. Many experiments performed using the Renishaw use the water band (ca. 3400 cm^{-1}) as a convenient reference standard. The use of such a standard would be very difficult on the Dilor; the intrinsic width of the H_2O line is about 1000 cm^{-1} making it impossible to get the entire spectrum of the water band onto the Dilor's detector at one time.

Chapter 3

Literature Review

3.0 Scope

In order to discuss the spectroscopic observations contained in this thesis pertaining to the mechanism of CO₂ reduction at copper electrodes, several aspects of the scientific literature will be reviewed: the spectroscopy of solid and solution phase Cu species; a brief review of various related adsorbates on the surface of copper; the electrochemical reduction of CO₂ on copper as it relates to the mechanism of reduction.

3.1 Solids

In an electrochemical process a solid thin film often forms on the electrode surface. These deposits can be observed spectroscopically, and very thin layers of adsorbates can be observed using SERS. Some of the important substances that might be expected on copper are oxides, hydroxides, and carbonates.

3.1.1 Copper Oxides

Two forms of copper oxide that are reported to exist on the surface of the copper electrode, are Cu₂O and CuO. Both of these have been spectroscopically characterised. It has been proposed that the composition of the electrolyte

solution will have an impact on which species are formed and which ones are stable. It has been proposed, as well, that once formed, Cu₂O is quite difficult to reduce [48]. Table 3.1 lists the bands for Cu₂O and CuO, observed and calculated, as reported by the authors reviewed in this section.

Dawson et al. [49] measured Raman and IR spectra of single crystals to study the vibrational and dielectric properties of Cu₂O. They used Kr⁺ (647.1 nm) excitation. The structure of Cu₂O consists of an octahedral arrangement of Cu and O atoms of space group O_h⁴ (P_{n3m}; Z=2). They classified the vibrational modes as follows:

$$\Gamma = F_{2g} + 2F_{1u} + F_{2u} + E_u + A_{2u}$$

Cu₂O should possess only one Raman active mode - an F_{2g} corresponding to a Cu-O stretch. Two IR modes F_{1u} are also expected. The F_{2u}, E_u, and A_{2u} are expected to be both IR and Raman inactive. However they reported that the Raman spectrum of Cu₂O contained 15 lines, probably due to a lowering of the symmetry by imperfections in the lattice [49].

Cardona [50] provided a review of the principles of Resonant Raman scattering in solids and noted that all of the u modes, which are normally Raman inactive, have been observed in the Raman spectrum of Cu₂O. Cu₂O is a

Table 3.1: Band Assignments for Cu₂O and CuO

Cu ₂ O - Raman	Cu ₂ O - Calculated	CuO - Raman	CuO - IR	Ref.
110(F _{2u}), 122(E _u), 159(F _{1uTO}), 173(F _{1uLO}), 316(A _{2u}), 570(F _{2g}), 629(F _{1uTO}), 660(F _{1uLO})				[49]
86(F _{2u}), 110(E _u), 152(F _{1u}), 350(A _{2u}), 515(F _{2g}), 633(F _{1uTO}), 662(F _{1uLO})				[51]
106, 125, 150*, 160, 190, 192*, 204*, 220*, 300, 420, 485, 640*				[59]
297, 411, 492, 633, 786		250, 300, 347, 635		[60] [63]
	110(F _{2u}), 122(E _u), 159(F _{1uTO}), 173(F _{1uLO}), 316(A _{2u}), 570(F _{2g}), 629(F _{1uTO}), 660(F _{1uLO})			[62]
520, 585				[67]
148, 215, 641				[64]
520, 590				[68]
		296(A _g), 344(B _g), 629(B _g)	147(B _u), 163(A _u), 324(A _u), 444(A _u), 515(B _u), 586(B _u),	[71]

* in both single crystal and crushed samples

semi-conductor with a band gap of 2.17 eV (572 nm) [51]. At energies near this band gap it is possible to produce excitons. The excitation of the excitons can allow for the observation of Resonant Raman scattering from all of the odd parity phonons (i.e., the u modes). These excitons are classified as the yellow, green, blue, and indigo series, based on the energy of the incident light required to excite them [50].

Reimann and Syassen [51] conducted an investigation into the high pressure properties of single crystal Cu_2O . They tabulated the Cu_2O bands, which had been reported by Petroff et al. [52] and provided a pictorial description of the vibrational modes. Reimann and Syassen [51] also provided a conversion table between the various nomenclatures used to describe the phonon modes of Cu_2O , as well as their ambient pressure assignment, and a tabulation of the exciton energies. The lowest energy exciton is at 2.02 eV (613 nm) [51]. Thus the study of Dawson et al. [49], described earlier, should not have involved any exciton-induced resonance since the Kr^+ laser wavelength (647.1 nm) is below the energy of the first exciton series.

Of the several studies of the Raman spectrum induced by excitons [52-58] the most relevant to this research is the study of the blue exciton series. In this study Yu et al. [53] used the 488 nm line of an Ar^+ laser to observe the spectrum of Cu_2O . They observed that the most intense band of

the spectrum was the F_{1u} mode at 665 cm^{-1} . They also observed considerable enhancement of a mode at 308 cm^{-1} which they noted could be assigned to either a combination mode, or perhaps the A_{2u} phonon mode. They also observed the F_{2g} mode at 515 cm^{-1} . This mode is the only normally active Raman mode and in their spectrum it is one of the weakest bands. Compaan and Cummins [57], reported that this mode did not show any resonant enhancement from the yellow exciton series.

Taylor and Weichman [59] used the 647.1 nm (1.92 eV) line of a Kr^+ laser to obtain Raman spectra of both single crystal and crushed samples of Cu_2O . For the single crystal they observed five bands. For the crushed sample they observed these five bands as well as an additional seven. They attributed the observation of normally Raman inactive modes to defects of the lattice structure which caused a breakdown in the selection rules.

Mayer [60] used Raman spectroscopy to study compressed Cu_2O powder. He observed 5 bands which he attributed to various phonon modes that were active due to defects in the crystal structure. These bands are the same as those reported by Hamilton et al. [61]. In both of these studies the authors used the 488 nm line of an Ar^+ laser for the excitation source. As a result, a number of the observed bands were likely due a resonance enhancement of modes that normally would be Raman inactive.

Hoffman et al. [62] performed a theoretical calculation of Cu_2O phonons using a rigid ion model. They measured the IR spectrum in the UHV of a single crystal of Cu(100) onto which they had coadsorbed oxygen and potassium in order to study alkali-promoted oxidation. As well as a band attributable to a K-O vibration (203 cm^{-1}), they observed three bands attributed to Cu_2O at 629 cm^{-1} ($F_{1u}TO$), 659 cm^{-1} ($F_{1u}LO$), and 124 cm^{-1} (E_u). They stated that the E_u mode, normally IR inactive, was observed due to a lowering of the symmetry of the thin film on the surface. Based on the observed IR bands, they modified the force constants in their calculation and determined the expected band positions associated with the other phonon modes.

The formation of Cu_2O has been observed during anodic cycling of electrodes in hydroxide solutions. The formation of anodic copper oxide films was studied by both Mayer and Muller [63], and Hamilton et al. [61]. Both groups used Raman spectroscopy and 488 nm excitation to observe Cu_2O and $\text{Cu}(\text{OH})_2$ films on the surface of the copper electrode. Hamilton et al. [61] attributed their ability to observe these bands to the excitation used. They proposed that the enhanced signal resulted from a resonance Raman scattering effect caused by the blue excitation. Mayer and Muller observed the same bands and concurred with this mechanism of signal enhancement [63].

Melendres et al. [64] recorded the Raman spectra of anodic films formed on copper in SO_4^{2-} solution. They also used 488 nm excitation. However they did not comment on whether or not a resonance Raman process was occurring. They observed three bands, at 148, 215, and 641 cm^{-1} , which they attributed to Cu_2O formed on the electrode. They also analyzed the film using XRD and confirmed that the film was Cu_2O . Their observation of IR active bands led them to the conclusion that the film on the surface was considerably distorted from its crystalline structure. However they did not take into account that there may have been a resonance effect due to the excitation used.

More recently, Melendres et al. [65] studied the oxidation of Cu in 0.1 M NaOH using synchrotron IR radiation. They observed bands at 630 and 1110 cm^{-1} which they attributed to the presence of a Cu_2O film. The IR spectrum of Cu_2O , formed as a copper corrosion product in clean moist air, has been reported by Persson and Leygraf [66]. They reported a single band at 645 cm^{-1} which they attributed to Cu_2O .

The SERS from oxide films on copper has been reported in conjunction with studies involving corrosion inhibitors on copper surfaces [67,68]. In both of these studies the authors used the 647.1 nm line of a Kr^+ laser as the excitation source. Carron et al. [67] used SERS to study the films formed on exposed copper. They observed that the Cu_2O film produced two broad bands

bands at 520 and 585 cm^{-1} . They assigned these bands to the symmetric and anti-symmetric stretches of Cu_2O . They estimated that the film they observed grew at such a rate as to reach a limiting thickness of roughly six monolayers in 1 hour. These conclusions were supported by Xue and Zhang [68], who observed two broad SERS bands, at 520 and 590 cm^{-1} , which were also attributed to a symmetric and anti-symmetric stretch of Cu_2O . They also observed a growth of the oxide film with time.

Nanba and Martin [69] observed SERS from oxides on copper smokes, using the 647.1 nm line of a Kr^+ laser. The smokes were prepared by heating copper metal and depositing it on a cooled substrate. These films were compared with those obtained by heating copper metal in oxygen and it was concluded that the observed spectrum was indicative of an amorphous Cu_2O layer on the surface of the metal. The bands attributed to Cu_2O , between 300 and 700 cm^{-1} , were considerably broadened, similar to those obtained in the electrochemical studies of Carron et al. [67] and Xue and Zhang [68].

Hagemann et al. [70] performed a thorough analysis of the vibrational modes of CuO . CuO is monoclinic C_{2h}^6 ($\text{C}2/c$; $Z=2$). The vibrational modes were classified as follows:

$$\Gamma = A_g + 2B_{2g} + 3A_u + 3B_u$$

There will be 3 Raman active modes, 1 A_g and 2 B_{2g} modes, and 6 IR active modes, 3 A_u and 3 B_u . Using Raman spectroscopy of oriented single crystals, they observed modes at 297 (A_g), 344 (B_g), and 629 (B_g) cm^{-1} [70].

Narang et al. [71] studied the IR spectra of powdered CuO. They combined their observations with the IR and Raman data on CuO reported by several other authors. Based on these data, they performed a normal coordinate analysis of CuO and provided a pictorial representation of the various vibrational modes.

None of the authors who reported observing Cu_2O films on the electrode, reported the observation of CuO films. Mayer [60] and Hamilton et al. [61] both reported Raman spectra of CuO powder and observed bands at 250, 300, 347, and 635 cm^{-1} in this reference sample. However, they noted that the Raman scattering was quite weak.

3.1.2 Copper Hydroxide

$\text{Cu}(\text{OH})_2$ has (4+2) coordination with 4 short (1.94 Å) and 2 long (2.63 Å) Cu-O bonds. It is difficult to prepare as a single crystal [72]. The Raman spectrum of $\text{Cu}(\text{OH})_2$ was reported for solution and the solid state by both Mayer and Muller [63] and Hamilton et al. [61]. The Raman spectrum of

reported by Hamilton et al. [61] contains a broad band consisting of at least two components at 488 cm^{-1} and a smaller band at 292 cm^{-1} . Mayer and Muller [63] observed these bands as well as one at 450 cm^{-1} .

3.1.3 Copper Carbonates

Although the simple copper carbonate solid CuCO_3 can be prepared in the solid state, it is not stable under normal conditions of temperature and pressure [72]. The stable mineral forms of copper carbonate are azurite ($2\text{CuCO}_3 \cdot \text{Cu}(\text{OH})_2$) and malachite ($\text{CuCO}_3 \cdot \text{Cu}(\text{OH})_2$) [72]. An IR spectrum of an amorphous malachite mineral, Georgeite, has been reported. However none of its bands were tabulated or assigned [73]. Malachite and azurite have both been the subject of detailed vibrational spectroscopic studies, including a normal co-ordinate analysis of both the internal and lattice modes [74]. The band assignments for copper carbonates are presented in Table 3.2. Reference spectra of malachite and azurite mineral samples are shown in Fig. 3.1.

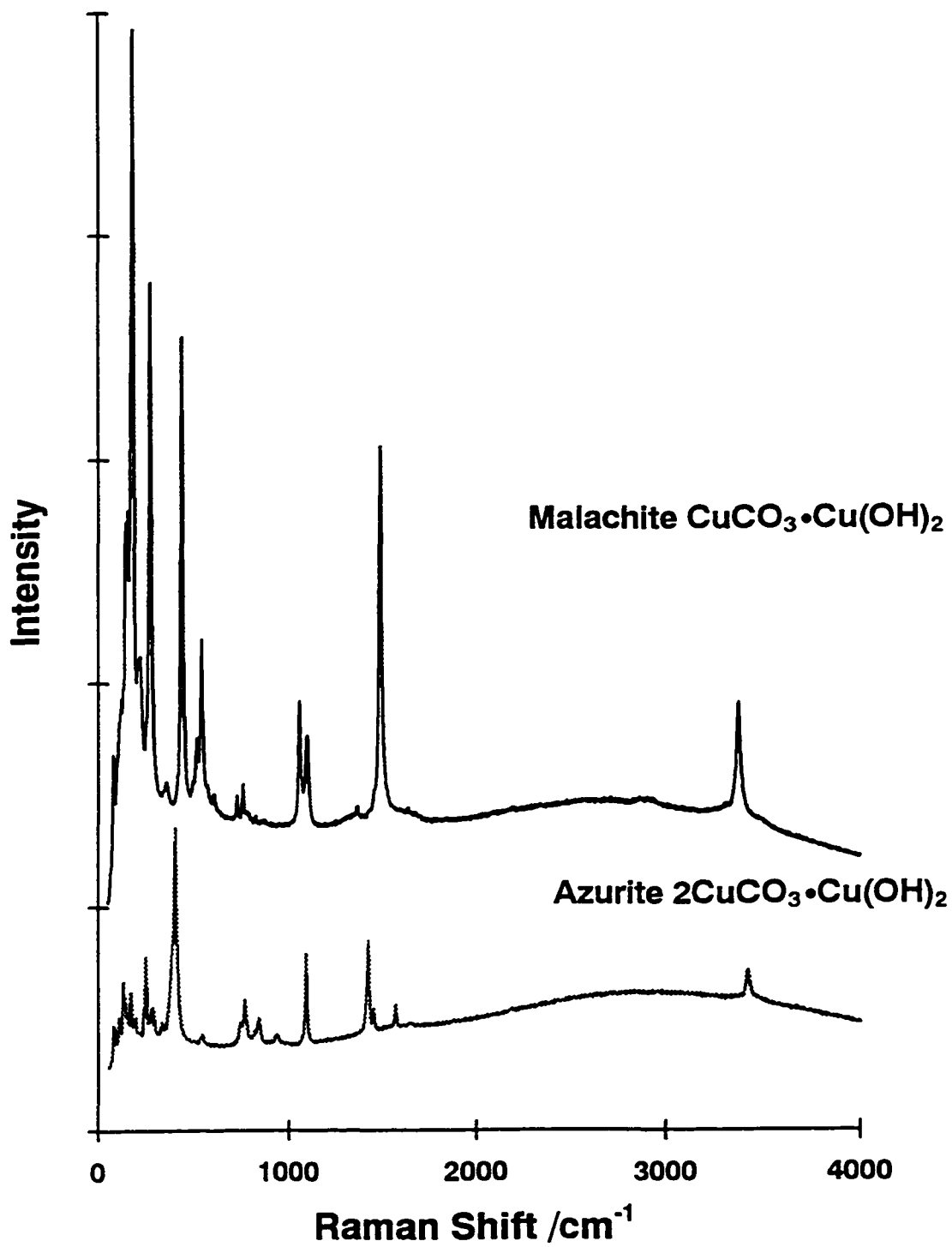
Goldsmith and Ross [74] carried out a complete study of the IR spectrum of malachite and azurite. They performed a normal coordinate analysis for both minerals and presented a table of band assignments. Schmidt and Lutz [75] used Raman spectroscopy to study malachite as part of a study of

Table 3.2: Band Assignments for Copper Carbonates

$\text{CuCO}_3 \cdot \text{Cu}(\text{OH})_2$		$2\text{CuCO}_3 \cdot \text{Cu}(\text{OH})_2$		$\text{Na}_2[\text{Cu}(\text{CO}_3)_2] \cdot 3\text{H}_2\text{O}$	
IR [74]	Raman	IR [74]	Raman	Salt [77]	Ion [77]
3400(ν_{OH}) 3320(ν_{OH})	3381	3425(ν_{OH})	3430	3570($\nu_{\text{H}_2\text{O}}$)I 3450($\nu_{\text{H}_2\text{O}}$)I 3440($\nu_{\text{H}_2\text{O}}$)R 3225($\nu_{\text{H}_2\text{O}}$)R 3220($\nu_{\text{H}_2\text{O}}$)I	
1800($\nu_1 + \nu_4 \text{CO}_3^{2-}$)		2560($\nu_1 + \nu_3 \text{CO}_3^{2-}$) 2490($\nu_1 + \nu_3 \text{CO}_3^{2-}$) 1830($\nu_1 + \nu_4 \text{CO}_3^{2-}$) 1670($2\nu_2 \text{CO}_3^{2-}$)	1576	1675($\delta_{\text{H}_2\text{O}}$)I 1672($\delta_{\text{H}_2\text{O}}$)R 1605($\delta_{\text{H}_2\text{O}}$)I 1599($\delta_{\text{H}_2\text{O}}$)R 1525($\nu_3 \text{CO}_3^{2-}$)I 1523($\nu_3 \text{CO}_3^{2-}$)R 1395($\nu_3 \text{CO}_3^{2-}$)R 1385($\nu_3 \text{CO}_3^{2-}$)I 1355($\nu_3 \text{CO}_3^{2-}$)I 1330($\nu_3 \text{CO}_3^{2-}$)B 1071($\nu_1 \text{CO}_3^{2-}$)R 1070($\nu_1 \text{CO}_3^{2-}$)I 1055($\nu_1 \text{CO}_3^{2-}$)I	1550($\nu_3 \text{CO}_3^{2-}$)R
1500($\nu_3 \text{CO}_3^{2-}$) 1400($\nu_3 \text{CO}_3^{2-}$)	1493	1490($\nu_3 \text{CO}_3^{2-}$) 1415($\nu_3 \text{CO}_3^{2-}$)	1457 1429	1525($\nu_3 \text{CO}_3^{2-}$)I 1523($\nu_3 \text{CO}_3^{2-}$)R 1395($\nu_3 \text{CO}_3^{2-}$)R 1385($\nu_3 \text{CO}_3^{2-}$)I 1355($\nu_3 \text{CO}_3^{2-}$)I 1330($\nu_3 \text{CO}_3^{2-}$)B 1071($\nu_1 \text{CO}_3^{2-}$)R 1070($\nu_1 \text{CO}_3^{2-}$)I 1055($\nu_1 \text{CO}_3^{2-}$)I	
1095($\nu_1 \text{CO}_3^{2-}$)	1100	1090($\nu_1 \text{CO}_3^{2-}$)	1094	1071($\nu_1 \text{CO}_3^{2-}$)R 1070($\nu_1 \text{CO}_3^{2-}$)I 1055($\nu_1 \text{CO}_3^{2-}$)I	
1045(op_{OH}) 875(op_{OH}) 820($\nu_2 \text{CO}_3^{2-}$) 803($\nu_2 \text{CO}_3^{2-}$)	1058 818	1035(op_{OH}) 952(op_{OH}) 837($\nu_2 \text{CO}_3^{2-}$) 817($\nu_2 \text{CO}_3^{2-}$) 769($\nu_4 \text{CO}_3^{2-}$) 747($\nu_4 \text{CO}_3^{2-}$)	934 837 817 763 740	855($\nu_2 \text{CO}_3^{2-}$)I 766($\nu_4 \text{CO}_3^{2-}$)R 750($\nu_4 \text{CO}_3^{2-}$)B 700($\nu_4 \text{CO}_3^{2-}$)I 697($\nu_4 \text{CO}_3^{2-}$)R 645($\nu_4 \text{CO}_3^{2-}$)I 625-525($\rho_{\text{H}_2\text{O}}$)R 570($\rho_{\text{H}_2\text{O}}$)I	755($\nu_4 \text{CO}_3^{2-}$)R
748($\nu_4 \text{CO}_3^{2-}$) 710($\nu_4 \text{CO}_3^{2-}$)	750 720	747($\nu_4 \text{CO}_3^{2-}$)	740	766($\nu_4 \text{CO}_3^{2-}$)R 750($\nu_4 \text{CO}_3^{2-}$)B 700($\nu_4 \text{CO}_3^{2-}$)I 697($\nu_4 \text{CO}_3^{2-}$)R 645($\nu_4 \text{CO}_3^{2-}$)I 625-525($\rho_{\text{H}_2\text{O}}$)R 570($\rho_{\text{H}_2\text{O}}$)I	
580(A_g, ν_{CuO}) 570(A_g, ν_{CuO}) 528(A_g, ν_{CuOH}) 522(A_g, ν_{CuOH}) 505(B_{3u}, ν_{CuO}) 485($B_{2u}, \nu_{\text{CuOH}}$) 425(A_g, ν_{CuX}) 418(A_g, ν_{CuX}) 337(B_{1u}, ν_{CuX})	598 566 536 512 491 434 352	495(A_g, ν_{CuO}) 455(A_g, ν_{CuOH}) 400(B_{3u}, ν_{CuO}) 345($B_{2u}, \nu_{\text{CuOH}}$)	537 399 336 330 324	500($W_{\text{H}_2\text{O}}$)I 355($W_{\text{H}_2\text{O}}$)I 330(ν_{CuO})R 325(ν_{CuO})I	350(ν_{CuOCO_2})I
325($B_{1g}, \delta_{\text{OCuOH}}$) 295($B_{3u}, \delta_{\text{OCuOH}}$) 278($B_{2u}, \delta_{\text{OCuOH}}$)	271	305($B_{1g}, \delta_{\text{OCuOH}}$)	280 264	325(ν_{CuO})I 280(ν_{CuO})I 275(ν_{CuO})R	320(ν_{CuOCO_2})I 310(ν_{CuOCO_2})R
206($B_{3g}, \delta_{\text{OHCuX}}$) 176($B_{2g}, \delta_{\text{OCuX}}$) 176($B_{1u}, \delta_{\text{OCuX}}$) 152($B_{1u}, \delta_{\text{OHCuX}}$) 132($B_{2u}, \delta_{\text{OHCuX}}$) 132($B_{3u}, \delta_{\text{OCuX}}$)	215 205 181 170 155 145 120 80	240($B_{2u}, \delta_{\text{OCuOH}}$) 240($B_{3u}, \delta_{\text{OCuOH}}$) 194(B_{1u}, op) 170(B_{1u}, op)	247 237 193 170 153 141 132 112 84		

I=Infrared, R=Raman, B=Both Infrared & Raman, op=out-of-plane bend, X=distant oxygen

Fig. 3.1: Spectra from Azurite and Malachite Mineral Samples



hydrogen bonding in crystalline compounds. They only reported assignments for the internal modes of malachite. Burgio et al. [76] used Raman spectroscopy to study azurite and malachite pigments. They identified azurite as a blue pigment with a characteristic band ca. 401-406 cm^{-1} and malachite as a green pigment with a characteristic band at ca. 432 cm^{-1} . A complete Raman spectrum of the azurite mineral does not seem to have been reported in the literature.

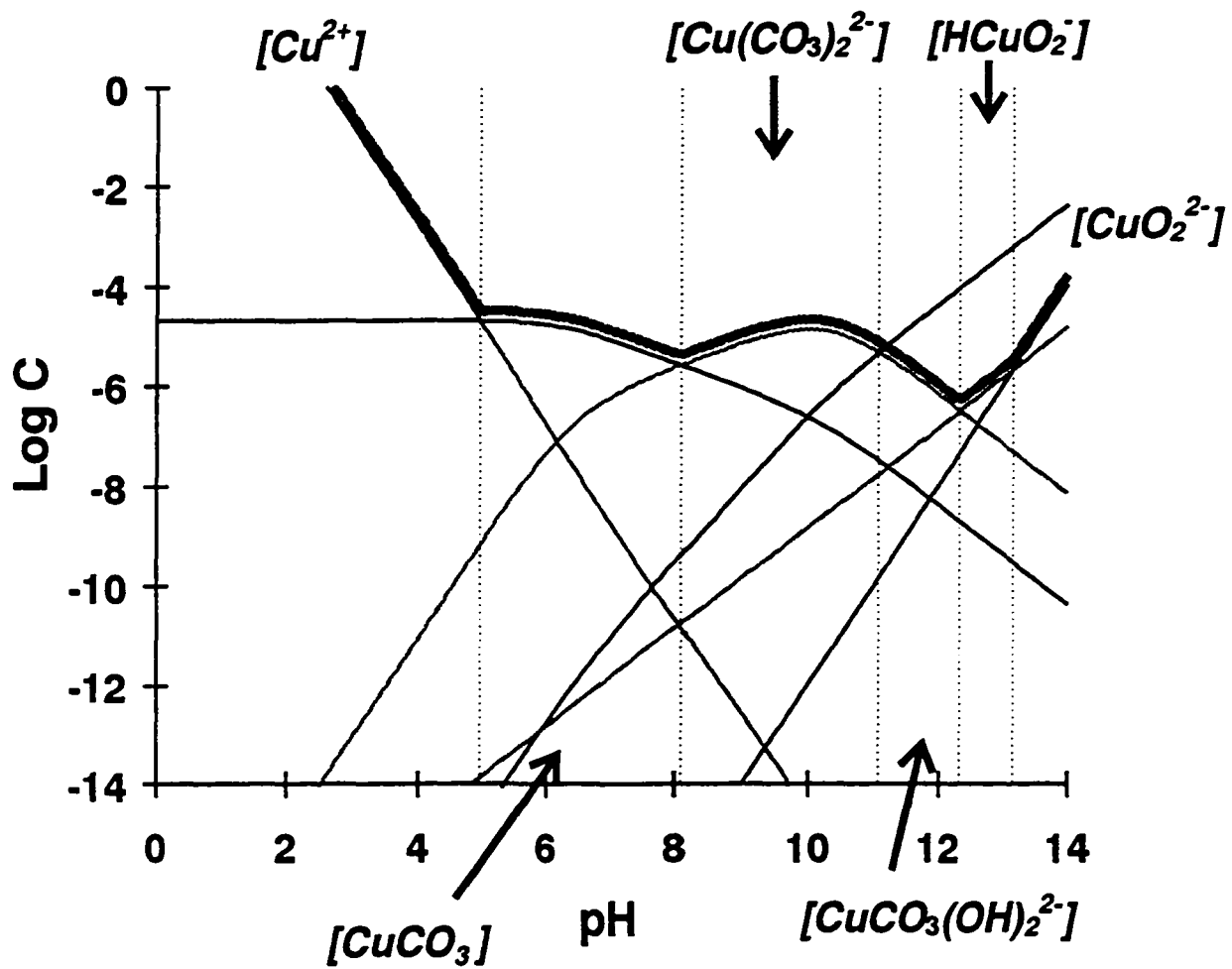
It is also possible to prepare double salts of carbonates, such as $\text{Na}_2[\text{Cu}(\text{CO}_3)_2] \cdot 3\text{H}_2\text{O}$ [72]. Taravel et al. [77] obtained the IR and Raman spectrum from this salt, its deuterated analog, and the soluble $[\text{Cu}(\text{CO}_3)_2]^{2-}$ ion. The Raman and IR bands of this salt which were assigned based on the modes of free CO_3^{2-} are shown in Table 3.2. In order to obtain the spectrum of the complex ion they added copper nitrate to a K_2CO_3 solution. Unfortunately the bands of the nitrate ion (1044 cm^{-1}) and the free carbonate obscured those of the copper carbonate complex ion. They were, however, able to detect two IR bands at 350 and 320 cm^{-1} and a Raman band at 310 cm^{-1} that they assigned to the vibrational modes of Cu-OCO_2 . They also observed two Raman bands at 755 and 1550 cm^{-1} which were assigned to the $\nu_4(\text{CO}_3^{2-})$ and $\nu_3(\text{CO}_3^{2-})$ modes of the copper carbonate complex ion.

3.2 Solutions

The Cu/CO₂/H₂O system can be quite complex and it is possible for a number of solution phase species to be formed. The Cu⁺ ion is not stable in solution and disproportionates to Cu²⁺ and Cu⁰ in aqueous solution [48]. A number of Cu²⁺ ions have been considered as solution components [78]: CuCO₃, Cu(CO₃)₂²⁻, CuCO₃(OH)₂²⁻, HCuO₂⁻, and CuO₂²⁻. The concentrations of these ions in solution will depend on the total concentration of Cu²⁺ and the pH of the solution. According to both Pourbaix [78] and Stumm and Morgan [79] the Cu²⁺ ion concentration in solution will be determined by the solubility of the two most stable solids, CuO and CuCO₃Cu(OH)₂ (Malachite).

By using the equilibrium relationships between these species it is possible to prepare a log C versus pH plot, similar to those presented in chapter 1. The plot presented in Fig. 3.2 is based on Pourbaix's equilibrium equations [78]. This figure demonstrates that as the pH is increased, the predominant solution species shifts: from Cu²⁺, below a pH of 5; to CuCO₃, between a pH of 5 and 8.1; to Cu(CO₃)₂²⁻, between a pH of 8.1 and 11.2; to CuCO₃(OH)₂²⁻, between a pH of 11.2 and 12.3; to HCuO₂⁻, between a pH of 12.3 and 13.2; to CuO₂²⁻ above a pH of 13.2. In CO₂-saturated 0.1 M HCO₃⁻ (pH = 6.8) Cu²⁺ will be present predominantly in the form of a CuCO₃ complex.

Fig. 3.2: The Distribution of Cu^{2+} Species as a Function of pH

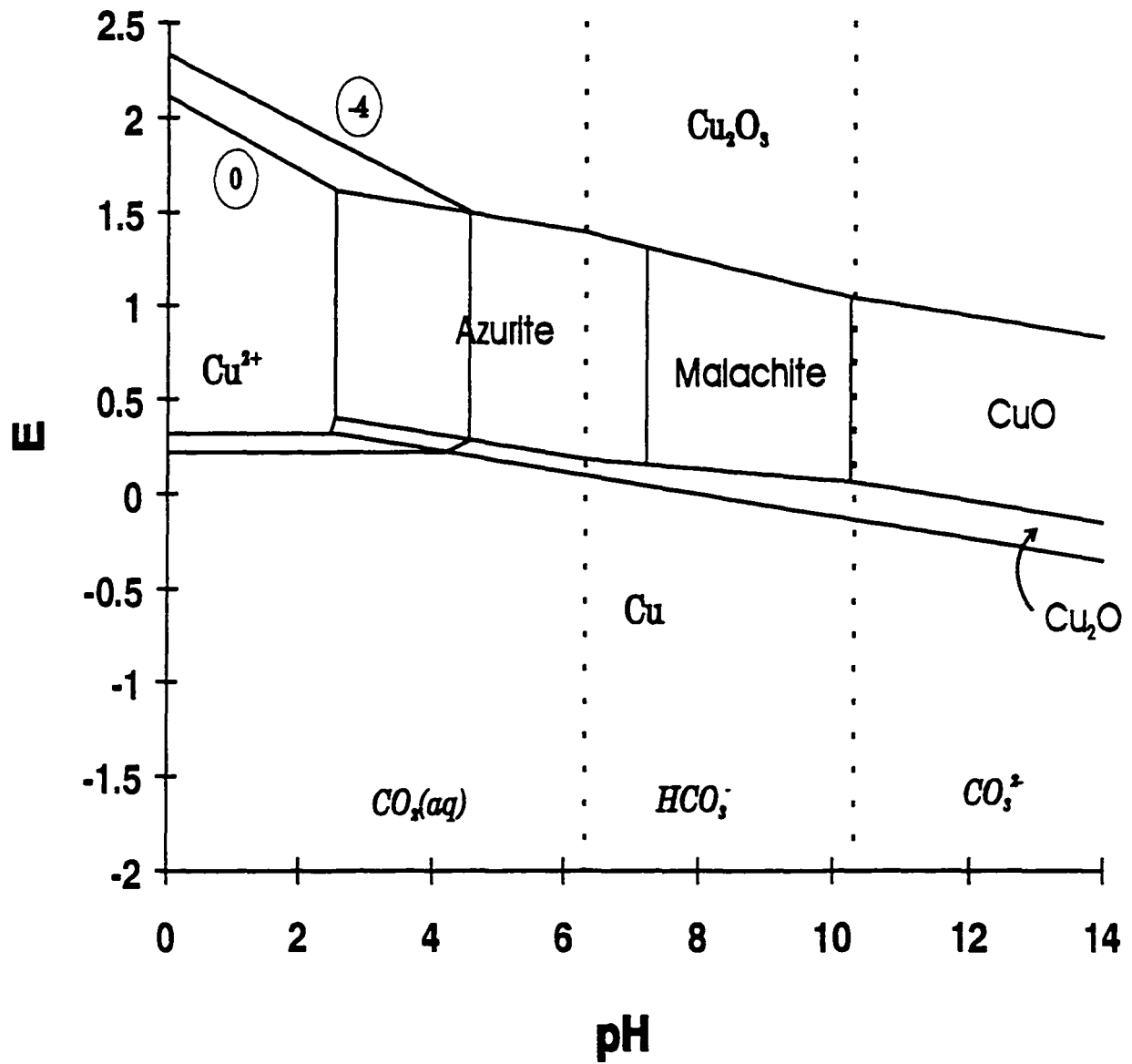


3.3 Electrodes in Bicarbonate Solution

In order to summarize the solid and solution phase products expected in an electrochemical system, it is useful to examine their stability as a function of potential and pH. The result is known as a Pourbaix diagram and it represents the thermodynamically favourable species at different potential and pH values.

Pourbaix [78] has produced diagrams showing the substances that might be expected at different total carbonate concentrations. Figure 3.3 is an abbreviated diagram based on the equations used by Pourbaix for the Cu/CO₂/H₂O system where $C_T(\text{CO}_2) = 0.1 \text{ M}$ (i.e., 0.1 M HCO₃⁻) [78]. This diagram shows the substances expected to be stable at different pH levels. For acidic solutions, pH below 2.5, the dissolution of the electrode as Cu²⁺ ions is expected as the potential is increased. Between pH 2.5 and 4.5, based on the concentration of Cu²⁺ ions in solution, either the dissolution of the electrode as Cu²⁺ ions, or Cu₂O followed by azurite is expected as the potential becomes more positive. In Fig. 3.3 the "0" line represents a Cu²⁺ concentration of 1 M and the "-4" line represents 10⁻⁴ M. For a pH above 4.5, it is expected that as the potential increases, Cu₂O will be formed initially. The subsequent product will be azurite, for pH between 4.5 and 7.2, malachite for pH between 7.2 and 10.3, or CuO for pH above 10.3. Further increases in potential are proposed to

Fig. 3.3: A Pourbaix Diagram for the Cu/CO₂/H₂O System at 0.1 M Total Carbonate Concentration



produce Cu_2O_3 . It is also possible for the solids at the various potentials to be in equilibrium with the solution components shown in Fig. 3.2.

Perez-Sanchez et al. [80] have studied the cyclic voltammetry of copper electrodes in 0.1 M NaHCO_3 solutions. They concluded that the passive layer, formed on copper during the anodic sweep, is composed of a complex mixture of Cu_2O , CuO , hydroxides, and carbonates. The initial film formation step was the creation of a Cu_2O layer. At more positive potentials the formation of a thicker Cu_2O layer occurred. This was followed by the formation of a CuO/OH/carbonate layer. The voltammetric features observed during the cathodic sweep were assigned to the reduction of CuO-Cu(OH)_2 to Cu_2O and from Cu_2O to Cu . They also found a feature that was assigned to "a soluble copper carbonate containing Cu ionic species originated at the reaction interface" [80]. They compared this to alkaline solutions, NaClO_4 with a pH of 9.1 and 11, where they observed features attributable to the formation of oxide and hydroxide layers as well as the dissolution of Cu^{2+} ions.

3.4 Adsorbates

Since the electrochemical reduction of CO_2 can lead to a number of products there are a wide variety of species that might be observed on the electrode surface. The literature review will be limited to the SERS, IR and

HREELS spectra primarily from copper in the UHV and electrochemical environments. As well, in this section the SERS and HREELS spectra of adsorbed water on metal surfaces will be discussed.

3.4.1 Adsorbed CO

Oda et al. [43] used SERS to study CO₂ reduction on copper in CO₂-saturated and CO-saturated 3.5 M KCl. Their electrolyte was saturated with CO for 30 seconds at -0.6 V, then cycled from -0.2 V to 0.7 V and back to a working potential at a rate of 5 mV/s. At -0.2 V, they observed a weak band at ca. 1940 cm⁻¹. Stronger bands at 2092 and 1958 cm⁻¹ were observed at -0.4 V. At -0.6 V these bands shifted to 2084 and 1934 cm⁻¹. They attributed these bands to two types of linearly adsorbed CO molecules.

When Oda et al. [43] saturated the KCl electrolyte with CO₂ for five minutes and performed the cycling as described above, they did not observe any CO bands until -1.4 V. At -1.0 V, a Cu-Cl mode was observed at 283 cm⁻¹. As the Cu-Cl band disappeared at -1.4 V, it was replaced by bands observed at 2046/1998 cm⁻¹, attributed to an adsorbed CO stretching mode, and at 360 cm⁻¹ attributed to a Cu-CO stretching mode. At -1.6 V the Cu-CO mode remained at 360 cm⁻¹, the adsorbed CO mode shifted to 2082/2037 and a band at 277 cm⁻¹

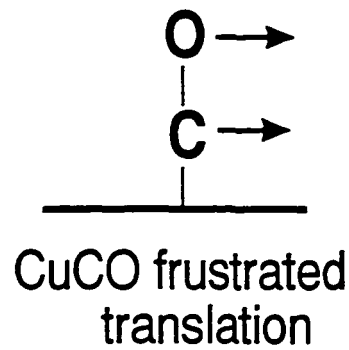
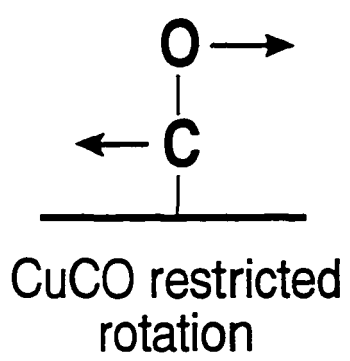
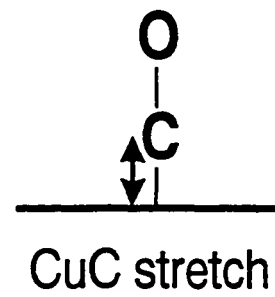
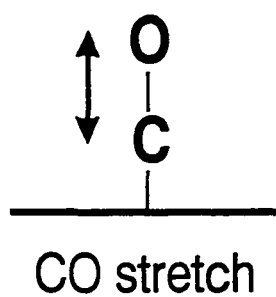
was observed but not assigned. At -1.8 V no bands were observed. They believed this indicated a quenching of SERS active sites.

Oda et al. [43] also studied the SNIFTERS spectrum of CO₂-saturated Na₂SO₄ on a copper electrode. They used a working potential of -0.7 V and a reference potential of -0.3 V. They observed that CO was adsorbed at -0.7 V and present (i.e., had not desorbed) at -0.3 V.

Akemann and Otto [81] used SERS in a UHV environment to study CO adsorbed on disordered copper. They observed four modes assigned as follows: the CO stretching mode at ca. 2102 cm⁻¹; the Cu-CO stretching mode at ca. 355 cm⁻¹; the restricted rotation of bound CO at ca. 282 cm⁻¹; the frustrated translation of the bound CO at ca. 24 cm⁻¹. A pictorial representation of these modes is given in Fig. 3.4.

Akemann and Otto [81] also considered the possibilities for the symmetry of the site on which the CO was adsorbed. For a low symmetry site, C_{2v}, each rotational and translational mode would be split into two components having B₁ and B₂ symmetry. For a higher symmetry site, C_{4v}, these modes would be doubly degenerate and have E symmetry. As they observed only one band for each of these modes, they thought that the CO must be adsorbed on a site of high symmetry, at least C_{3v}. They noted that the splitting of the

Fig. 3.4: A Illustration of the Vibrational Modes of an Adsorbed CO



spectral bands attributed to these modes might be too small to observe. Thus the symmetry of the site could not be assigned with certainty.

Akemann and Otto [81] thought that the observation of intense modes from the restricted rotation and frustrated translation was a clear indication that the SERS did not result from a macroscopic enhancement of the electric field at the surface. Using the terminology outlined in chapter 1, the SERS resulted from a CT type mechanism, not an EM type mechanism. If the EM mechanism was dominant then the rotation and translation modes, which are parallel to the surface, should be several orders of magnitude lower in intensity than the metal-carbon stretch and the CO stretch.

Akemann and Otto [81] noted that the apparent position of the bands changed, depending on the surface coverage. As the CO coverage was shifted from 0.1 L to 10 L the frequency of the restricted rotation shifted from 278 cm^{-1} to 286 cm^{-1} , while the metal-carbon stretch shifted from 346 cm^{-1} to 360 cm^{-1} . The CO stretching mode did not seem to show as great a shift. Based on the graph they presented, it appears that the frequency remained at 2102 cm^{-1} over a wide range of exposures. Because of the location of the CO stretch at 2102 cm^{-1} , they concluded that the frequency of this vibration was too great to be associated with the CO on a bridging site and that the CO was adsorbed in an on-top site.

Akemann and Otto [81] commented that the position of 2102 cm^{-1} was quite high even for an adsorbed CO on an on-top site. They reported IR vibrational frequencies for higher index surfaces at 2098 cm^{-1} for Cu(755), 2100 cm^{-1} for Cu(211) and 2102 cm^{-1} for Cu(311). They stated that the frequency of the CO stretching mode was higher for CuCO^+ ions than for CuCO surface adsorbates. According to Rack et al. [82] for a $\text{Cu}(\text{CO})^+$ cation the CO stretching mode range is 2062 to 2178 cm^{-1} , depending on its associated anion.

Akemann and Otto [81] interpreted the high frequency of the CO stretch as indicating that the electron density "smeared out" the contours of the atomic scale defects of the roughened surface. This created localized surface sites which were slightly electron deficient onto which the CO was adsorbed. They also stated that based on empirical evidence, the frequency of the observed CO adsorbates will increase as the electron density on copper is reduced. Otto et al. [23] subsequently assigned the adsorption site for CO on copper to an E type site.

Hirschmugl et al. [83] used IR to study CO adsorbed on Cu(100) in UHV and observed a CO stretch at $2079 - 2085\text{ cm}^{-1}$, a Cu-CO stretch at $343 - 345\text{ cm}^{-1}$, and a Cu-CO frustrated rotation at $283 - 285\text{ cm}^{-1}$, dependent on surface coverage. They also observed the Cu-CO rotational mode at 281 cm^{-1}

on Cu(111). They proposed that CO was adsorbed on a linear on-top site. Their spectra show a symmetrical band shape for the CO stretching mode.

Hori et al. [84,85] used IR to study CO-saturated phosphate buffer, CO-saturated 0.2 M KHCO₃, and CO₂-saturated 0.1 M KHCO₃ on copper. They observed a band at 2087 cm⁻¹ at a potential of -0.95 V, and 2085 and 2081 cm⁻¹ at a potential of -1.0 V. Westerhoff and Holze [86] used RAIRS to study adsorbed CO on copper in KClO₄ at potentials of -0.85 V and -1.05 V and observed a band at 2110 cm⁻¹. In both of these studies, all the bands are skewed to the lower wavenumber region of the spectra. Since these IR studies used a polycrystalline electrode, the surface was not uniform. However, Hirschmugl et al. [83] used single crystal Cu(100) (i.e., a uniform surface) and observed symmetrical bands. This suggests that the band skew reported for polycrystalline electrodes may be due to subtle changes in the surface adsorption sites.

The skewing of the CO stretching mode band is also apparent in the spectra published by Oda et al. [43] and Akemann and Otto [81]. This may be related to the adsorption sites on the copper. The surface disorder, needed to observe SERS, may result in slightly different on-top adsorption sites causing asymmetry in this band. This would indicate that asymmetry is not a

fundamental feature of the band, but is related to the disordered nature of the surface.

3.4.2 Adsorbed CO_2 and CO_2^-

Akemann and Otto [87,88] have recorded the spectrum of CO_2 adsorbed on copper in UHV. After 1 L of exposure, they observed bands at 650 and 1368 cm^{-1} . Due to the similarity between these bands and the gas phase frequencies, they were attributed to a non-activated adsorbed CO_2 on the copper surface. They also observed bands at 768 and 1182 cm^{-1} . These were shifted considerably from the gas phase frequencies and resembled the adsorbed CO_2 bands which had been observed on K. As a result, these bands were assigned to the presence of an activated adsorbed CO_2^- ion. Akemann and Otto [88] assigned the non-activated CO_2 and activated CO_2^- bands to E_1 and E_2 adsorbate sites, respectively. By increasing the exposure to 20 L, sharp bands at 1275 and 1382 cm^{-1} were observed. These were assigned to the Fermi resonance doublet of CO_2 on an N site.

Akemann and Otto [87,88] also studied the effect of temperature on the copper substrate. If the copper substrate was pre-annealed at 120 K, cooled to 40 K and exposed to CO_2 , bands attributed to both E_1 and E_2 sites were observed. When the copper substrate was then heated to 100 K, only bands

from the E_2 site, activated CO_2^- , remained. If the copper substrate was pre-annealed to 200 K, cooled to 40 K, and exposed to CO_2 , only bands attributed to non-activated CO_2 , E_2 site, were observed. The interpretation given was that once the activated CO_2^- was adsorbed, the chemisorption bond was strong and annealing the copper substrate to 120 K desorbed the non-activated CO_2 which was weakly bound. Since the activated CO_2^- was not observed when the copper substrate was annealed to 200 K, they reasoned that the adsorption of this anion occurs only at atomic scale defect sites (i.e., not on a smooth surface). They proposed that between 150 K and 200 K, the defect sites are destroyed preventing the adsorption of this anion.

3.4.3 Adsorbed Oxygen

The cathodic formation of hydroxides on copper has been reported. Hartinger et al. [89] used SERS to study Cu(111) electrodes in 0.5 M NaOH. At -1.06 V a large band at 700 cm^{-1} was observed and assigned to a surface CuOH formed at cathodic potentials. The frequency of this band was observed to shift to 725 cm^{-1} upon deuteration. They explained this upward shift upon deuteration by considering the CuOH(D) to be located in a three fold hollow site. This makes the isotopic shift complex since the coupling between the CuOH(D) and the internal O-H(D) modes changes. They concluded that while the mass change would shift the vibrational frequencies downward, as noted for

the O-H(D) modes, the coupling changes would shift the frequency upwards in accordance with their observations. They postulated that this formation might be linked to subsurface oxygen initially present in the electrode.

Yu et al. [90] used HREELS to study CO on Cu(100) in UHV. Bands for the CO stretch at 259 meV (2089 cm^{-1}) and the Cu-CO mode at 42 meV (338 cm^{-1}) were observed for the adsorbed CO. They also observed atomically adsorbed oxygen on the copper surface at 37 meV (298 cm^{-1}), which they believed stabilized the CO on the copper surface. As well, the oxygen was proposed to react with the CO to form CO_2 .

HREELS techniques have also been used to measure the chemisorption of oxygen on Cu(110) [91,92]. These studies have revealed a number of possible adsorption sites for the oxygen on the copper surface. Baddorf and Wendelken [92] recorded the HREELS spectra for Cu(110) exposed to oxygen. They identified several Cu-O vibrational features. When oxygen was initially added to the system a feature at 50 meV (403 cm^{-1}) was observed. The further addition of oxygen lead to the observation of two new features at 41 meV (330 cm^{-1}) and 62 meV (500 cm^{-1}). At the highest oxygen coverages two bands at 19 meV (153 cm^{-1}) and 81 meV (653 cm^{-1}) dominate the spectrum. They also presented a spectrum in which the count rate of electrons was low, which they attributed to the presence of a disordered surface. In this spectrum

a broad band at 62 meV (500 cm^{-1}) was seen to dominate the spectrum. They assigned the 50 meV (403 cm^{-1}) band to the presence of oxygen adsorbed on a long bridge site in accordance with previous research. Mundenar et al. [91] used EELS to study oxygen adsorption on Cu(110). They also observed a 41 meV (330 cm^{-1}) band which they assigned to an adsorbed oxygen on a four co-ordinated site. The 19 meV (153 cm^{-1}) and 81 meV (653 cm^{-1}) bands were assigned to bulk Cu_2O in accordance with the IR data. The band at 62 meV (500 cm^{-1}) was not fully assigned although it was attributed to some form of atomically adsorbed oxygen present on the Cu_2O .

3.4.4 Adsorbed CH Groups

Urban [11] provides a comprehensive review of the vibrational modes expected from a variety of adsorbed hydrocarbons. The bands of adsorbed methyls are listed as being in the $2750 - 2975\text{ cm}^{-1}$ region for the ν_s bands of CH and in the $2000 - 2175\text{ cm}^{-1}$ region for the ν_s bands of the deuterated analog.

On silver electrodes, bands in this region have been associated with carbonaceous contamination due to CO_2 reduction [20]. Mahoney et al. [111] studied SERS from silver electrodes in 0.1 M KF in the presence of CO_2 . They attributed a band at ca. 2900 cm^{-1} to CH_x species and bands at ca. 1360 and

1580 cm^{-1} to graphitic carbon. They attributed these bands to the decomposition of atmospheric CO_2 contaminating the silver surface. Inchinohe et al. [112] used SERS to study silver electrodes in 0.1 M potassium bicarbonate saturated with CO_2 . They observed CH bands at ca. 2700 - 2900 cm^{-1} . The band at 2870 cm^{-1} was assigned to the C-H stretch of a formate species while the band at 2750 cm^{-1} was assigned to an O-C-O overtone and a C-H stretch of a formate species.

3.4.5 Adsorbed Water

The SERS from the OH stretching modes of water coadsorbed with halide yields a very distinctive and specific band ca. 3500 cm^{-1} . Studies of the SERS of water have been virtually restricted to Ag electrodes. Pettinger [9] noted in his review of SERS that water became a focal point for the research concerning the nature of SERS as a molecularly specific technique. The fact that the SERS of water did not overwhelm the other bands became an important issue in this research. The author reported that SERS of water was readily observed when a halide, or pseudohalide, was present in the electrolyte. This was attributed to the coadsorption of halide and water in the interface. The author provided a summary of the research using concentrated (i.e., 1 M or greater) halide solutions. Most of this research has focused on the OH stretching region (ca. 3500 cm^{-1}).

From copper in halide media, Pettinger et al. [93] only observed weak bands in the OH stretching region. The only other SERS study of H₂O and D₂O on copper electrodes is by Chen and Tian [94]. They studied a copper electrode in 1.0 M Na₂SO₄ solution during the hydrogen evolution reaction. Intense spectra of the bending mode of water, ca. 1613 cm⁻¹, at -1.26 V was observed. They assigned a broad band at ca. 573 cm⁻¹ to the librational modes of adsorbed water. A weak band, ca. 3426 cm⁻¹, attributable to an O-H stretch was also observed. They used a potential difference technique to obtain the spectra, which involved the subtraction of a reference spectrum collected at a potential where SERS was not observed. This allowed the bulk water features to be removed from their spectra.

Chen and Tian [94] also examined the spectra of water adsorbed on Ag and Au electrodes under similar conditions. On Ag, they observed an increase in intensity of the bending mode at ca. 1612 cm⁻¹ and an intense mode at 526 cm⁻¹ attributed to a water libration. On Au electrodes, only a weak band at 1604 cm⁻¹, attributed to the bending mode of water, was reported. They said that the substitution of D₂O for H₂O shifted the peaks by a factor of about 1.3. They reported that this shift was consistent with the expected shift for a librational mode of water. They thought that the observation of some form of water structure at very negative potentials indicated that there was some

unique aspect of the SERS mechanism at work not readily explainable by either the CT or EM mechanisms.

Chen and Tian's study [94] was the only report found for copper electrodes in the absence of halides. Iwasaki et al. [95] studied Ag in 0.5 M NaOH solution. Although the primary focus was the study of anodic oxide films, they observed bands at negative potentials due to the presence of water molecules. An intense bending mode of water at ca. 1615 cm^{-1} and a broad band at ca. $500\text{ -}700\text{ cm}^{-1}$ were observed. These were both attributed to the presence of adsorbed interfacial water.

Dorain [96,97] found that for Ag electrodes in a solution of 0.1 M NaCl to which $50\text{ }\mu\text{M}$ KMnO_4 had been added, an 'AgMn' phase formed at -1.33 V . This phase had several oxides and hydroxides associated with it. The peak observed at 615 cm^{-1} was assigned to surface oxygen. The peak at 500 cm^{-1} was assigned to surface OH. A band at 415 cm^{-1} was assigned to adsorbed OH_2 . A band at 465 cm^{-1} was assigned to the metal oxygen vibration of dioxonium (O_2H_3). A band at 800 cm^{-1} was assigned to the OHO breathing mode of this dioxonium. These bands were assigned with the aid of D_2O isotopic substitution experiments.

In a subsequent paper Dorain [98] reported observing spectra of OH⁻ ions adsorbed on Mg²⁺ sites on the Ag surface from 10⁻² to 10⁻³ M MgCl₂ solution which contained trace amounts of KMnO₄ or Cl₂ as an oxidizing agent. The oxidizing agent was believed to provide a constant reformation of the surface due to a diffusion-controlled oxidation process. A peak at 533 cm⁻¹ was assigned to a Mg-OH mode associated with hydrogen evolution. A peak at 458 cm⁻¹ was assigned as in Dorain's previous experiments [96,97] to (Ag,Mn)-OH₂. It was noted that prolonged electrolysis would increase the interfacial pH through the production of OH⁻ and a corresponding increase in the SERS intensity would be observed. Deuteration produced a shift in the peak positions consistent with those expected for an OH group.

Pockrand [99,100] studied the SERS spectrum of H₂O and D₂O under UHV conditions. In these experiments the ratio of the bands due to the stretching and bending mode were similar to those expected for an ice-like surface phase.

Ibach and Lehwald [101] have studied the HREELS adsorption of water on a Pt surface. For low coverages (i.e., 0.5 L) the authors observed a number of unique features. The stretching modes of water were considerably weaker than the bending modes. Normally the stretching mode is more intense. The disproportional increase in the bending mode ca. 1630 cm⁻¹ was thought to

result from an increased dipole at the surface. Bands at 460 cm^{-1} and 570 cm^{-1} , which they attributed to a Pt-oxygen interaction, were also observed. On deuteration these two bands were replaced by a single larger band at 470 cm^{-1} . Thus it appeared that the 570 cm^{-1} band shifted and the 460 cm^{-1} band did not. These modes were assigned to adsorbed water and adsorbed oxygen respectively. As the exposure was increased to 10 L these low wavenumber bands were replaced by a broad band at 840 cm^{-1} . This was attributed to the formation of an ice-like surface structure.

3.5 Electrochemical Reduction of CO_2 on Copper

The electrochemical reduction of CO_2 on copper has been the subject of extensive investigations since 1985 [38,39,102,103]. Hori et al. [105] used chromatographic techniques to analyze the reaction products from 0.5 M KHCO_3 solution, continually saturated with CO_2 . They reported an analysis of the reaction products produced by the electrochemical reduction of CO_2 . They observed that the Faradaic efficiency for the formation of CH_4 from copper electrodes in 1 M KHCO_3 at -1.39 V was around 37 - 40%. The other products from this process included small amounts of CO, at 1.5 - 3.1% Faradaic efficiency and H_2 , at 32 - 33% Faradaic efficiency. In a later chromatographic study [105] the temperature of this reaction was varied. At 40° C they reported that CO_2 could also be reduced to produce C_2H_4 with an efficiency approaching 20%.

Hori et al. [106] subsequently used chromatography to study the electrochemical reduction of CO on copper as a function of electrode potential. In this study 0.1 M KHCO₃ saturated with CO₂ was used. The Faradaic efficiencies observed for copper electrode products in 0.1M KHCO₃ solution depended strongly on the reduction potential. H₂ was formed in excess of 80% efficiency at a potential of ca. -0.8 V. This efficiency decreased to around 20% as the electrode potential was lowered to -1.4 V. The Faradaic efficiency of CO was found to peak at ca. 20 % at about -1.2 V and decrease towards -1.4 V. At -1.4 V the Faradaic efficiency was found to be ca. 45% for CH₄ and 20% for C₂H₄. They observed that the Faradaic efficiency for the formation of CHOO⁻ was similar to the potential profile for CO. They concluded that CO₂ is initially reduced to CO and CHOO⁻, at potentials more positive than -1.1 V. The CHOO⁻ is not further reduced. However, the CO is further reduced and is the intermediate in subsequent reductions. They concluded, based on measurements with Cu and Pt electrodes, that CO is not as strongly bound to Cu as it is to Pt.

Since CO₂ interacts with water to form HCO₃⁻ and CO₃²⁻ ions, Kim et al. [107] used chromatographic techniques to study the gaseous products from the electrochemical reduction of copper in 0.5 M KHCO₃. They reported that when the electrolyte was not saturated with CO₂ there was no observable production of CO or CH₄. These experiments were repeated with K₂CO₃

electrolyte and in the absence of CO_2 no CO or CH_4 was observed. This indicates that the reduction of the solvated CO_2 molecule is the initial step and that the direct reduction of carbonate or bicarbonate does not occur.

Much research has focused on the unique ability of copper electrodes to produce high yields of hydrocarbons [39]. However, few authors have addressed the question of cathode poisoning which occurs during early stages of the electrolysis [39,102,103]. In general, the rate of production of the CO_2 reduction products, including methane, ethylene, and ethanol, rapidly decreases about 30 minutes after the start of electrolysis. These products are replaced by increasing amounts of hydrogen. The process of deactivation is not significantly affected by the degree of purity or the pretreatment of the copper electrode, or the pre-electrolysis of the solution [103].

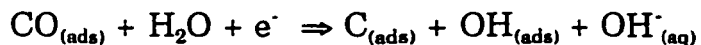
In order to further identify the species that may be present on the surface of the electrode during the electrochemical reduction of CO_2 it is helpful to examine some background information regarding the mechanism of this reaction. As outlined in chapter 1 the first step in the electrochemical reduction of CO_2 is the formation of the $\text{CO}_2^{\cdot-}$ ion which is then further reduced to CO [38]. For copper this adsorbed CO can be further reduced to methane. The participation of CO as the intermediate in the production of hydrocarbons has been demonstrated by Frese [39] who used chromatographic techniques to

observe that CO could be reduced to methane in CO-saturated 0.5 M KHCO_3 . Since the same products are obtained in CO_2 -saturated solution it was concluded that CO must be an intermediate step in the production of CH_4 . He also demonstrated that the reduction of CO_2 occurs by direct reduction of the solution phase CO_2 , not the reduction of bicarbonate or carbonate ions. The fact that it was not possible to observe any reduction product from N_2 -saturated bicarbonate or carbonate solution demonstrated that the reaction proceeds through the reduction of the solvated CO_2 .

The mechanism by which the methane is produced from the adsorbed CO has been the subject of some discussion. DeWulf et al. [102] applied XPS and AES techniques to study copper electrodes, used in the study of the reduction of CO_2 in 0.5 M KHCO_3 . The onset of methane production was observed at a potential of -1.36 V and the optimum Faradaic efficiency occurred at -1.76 V. At -1.76 V, with prolonged reaction time, a black film was observed on the electrode surface, attributed to graphitic carbon. They suggested that CO was reduced to a surface formyl Cu-HCO , which converted to a surface carbene Cu=CH_2 and finally to methane. These authors also proposed that the poisoning of the electrode was due to the generation of surface graphitic carbon from the reduction of COOH intermediates, produced from $\text{CO}_2^{\cdot-}$, as well as from a slight amount of CO splitting.

Another possible poisoning species might be a copper carbide. In methanation and Fisher Tropsch synthesis two forms of carbon have been proposed: a reactive graphitic species and a carbidic species which poisons the catalyst. The existence of the latter on Cu(110) and Cu(100) was deduced from AES peak positions after sample exposure to CO in UHV [108]. However, cluster calculations show that copper carbide would be unstable [109]. Although, Ivanov-Omskii and Frolova [110] reported observing copper carbides using Raman scattering, these carbides were deduced from changes occurring in the graphitic bands. No direct observation of a copper-carbon stretching mode was reported.

Frese [39] used X-Ray and EDAX analysis to study copper electrodes used in the reduction of CO₂ in 0.5 M KHCO₃. It was postulated that a thin Cu₂O film was formed which would affect the reaction and may be kinetically stable in the potential region where CO₂ reduction occurs. As well, based on thermodynamic arguments, he suggested that CO splitting was the major pathway to hydrocarbons and proposed the following mechanism:



The adsorbed carbon was then thought to be progressively hydrogenated to form CH_4 . He also proposed that the splitting of CO can result in the formation of an adsorbed oxygen.

Jermann and Augustynski [103] used chromatographic techniques to analyze the reaction products from the electrochemical reduction of CO_2 on copper. They investigated the effect of potential cycling on the poisoning of the reaction. Based on their findings they developed a methodology for prolonging the activity of the copper electrode and maintaining high rates of hydrocarbon production for extended periods of time. They reported that at -1.72 V the current efficiency for CH_4 production falls quite dramatically after 30 min of electrolysis. However, if the electrode was subjected to periodic anodic cycling ORCs, consisting of 3 scans to 1.3 V at 5 V/s every 5 minutes, then the catalytic activity of the electrode could be prolonged and the Faradaic efficiency for CH_4 production could be maintained at ca. 40% for up to 48 hours. They also demonstrated that this method was effective in regenerating a poisoned electrode. They showed that if a copper electrode was allowed to be poisoned, after 50 min of reaction time without periodic activation, it could be reactivated by the application of the periodic cycles described above. Since this process led to the creation of a rough surface it provided a unique opportunity to see if SERS sites were created and could be used to identify the intermediates at the copper surface during CO_2 reduction.

Chapter 4

Experimental Results and Discussion

4.0 Scope

In this chapter the experimental results for the Cu/CO₂/H₂O system are described. These include SERS characterization, time dependence, and voltammetry studies. The primary focus of the research has been to identify the intermediates found on the copper electrode surface during the electrochemical reduction of CO₂. This constitutes the majority of the chapter. During the course of these experiments information was obtained about the products formed on the electrode surface, at potentials other than those of interest for CO₂ reduction, and these will also be discussed.

Initial experiments on the Cu/CO₂/H₂O system were conducted using the Dilor instrument. These experiments demonstrated that the spectral bands attributed to adsorbed CO could be observed from Cu electrodes in 0.1 M NaHCO₃ [20,113]. Spectra of this adsorbate were measured and an initial estimate of the CO stretching band intensity decay over time was obtained. The conditions for which experimental data could be obtained were significantly broadened and the speed at which data could be accumulated increased dramatically with the arrival of the Renishaw instrument. As a result, the study of the electrochemical reduction of CO₂ on Cu was greatly expanded.

4.1 Experimental Results

The experimental results are divided into the following categories:

1) the relationship between ORCs and the creation of SERS active surfaces; 2) the voltammetry of CO₂-saturated solutions; 3) the effect of potential on the SERS spectra of CO₂-saturated solutions; 4) the effect of time on the SERS spectra during electrochemical reduction in CO₂-saturated and CO-saturated solutions; 5) the effect of time on the SERS spectra of the build up of a "poisoning species". All experiments relate to the species observed at the copper electrode surface. These sections are followed by a discussion of the band assignments.

4.1.1 The Creation of SERS Active Surfaces

In order to use SERS to study CO₂, it was first necessary to create a SERS active surface. In these experiments the SERS active surface has been created in gas-saturated 0.1 M H(D)CO₃⁻ without the use of halide. This electrochemical environment was chosen in order to closely mirror those used by Jermann and Augustynski [103].

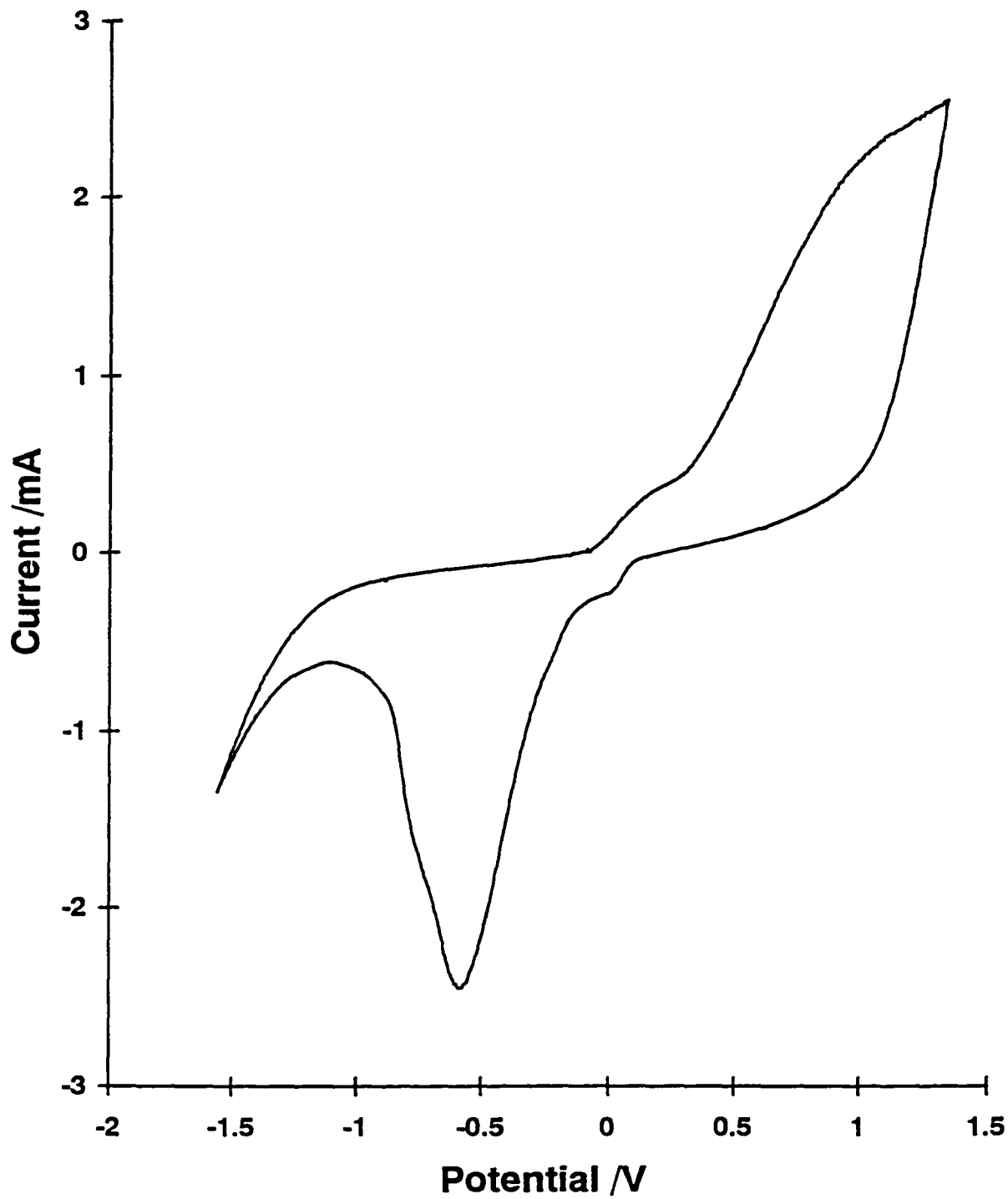
Using the Dilor it was possible to obtain a SERS spectrum from CO₂-saturated 0.1 M NaHCO₃ by stepping from OCP to a more negative

potential. Inconsistent and weak SERS spectra were observed. This indicated that although there was some film formation at OCP, it was not consistent enough to create a reliable SERS active surface. As a result potential cycling ORCs were employed to discover a suitable method for producing a SERS active surface.

Better quality SERS spectra were obtained if the potential was scanned at 10 mV/s. Increasing the anodic limit was also found to improve the SERS intensity. An upper potential limit of 1.3 V was established in order to be close to the potential limits used by Jermann and Augustynski [103] for their electrochemical reduction experiments. It was observed that this limit produced consistently intense SERS. The cathodic limit of -1.56 V was chosen as it was well into the region where CO₂ reduction occurs and at this point it was expected that the film formed during the anodic portion of the ORC would be reduced.

Jermann and Augustynski [103] found that fast cycling (i.e., 5 V/s) of the electrode removed the poisoning species. Thus fast cycling was incorporated into the pretreatment method for the copper electrode. Since the PAR 273 potentiostat is not capable of sweeping in excess of 1 V/s, this speed was used. It was observed that after several of these cycles a reproducible voltammogram was obtained, Fig. 4.1. This reproducibility, while not a guarantee of

Fig. 4.1: A Cyclic Voltammogram from CO₂-Saturated 0.1 M NaHCO₃/Cu at 1 V/s from -1.56 to 1.3 V

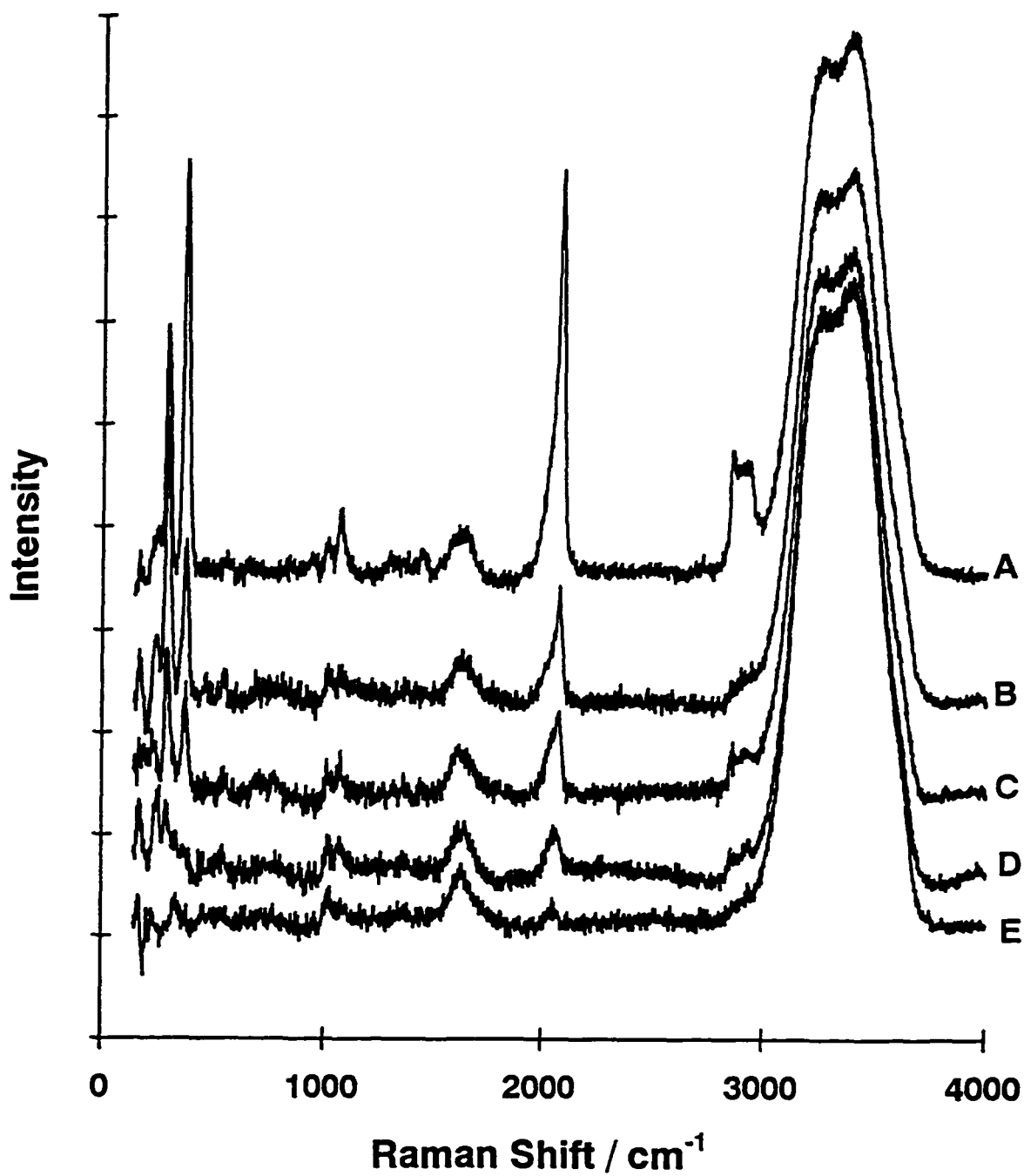


cleanliness, provided a reference point from which to examine the SERS of the system.

Unfortunately, the ORC sweep rate of 1 V/s did not create a surface that yielded intense SERS. Apparently, scanning at 1 V/s strips the poisoning species formed during the cathodic reduction of CO₂, but is not conducive to the formation of the small scale roughness required for SERS. One slower ORC of 10 mV/s was usually sufficient after these rapid cleaning ORCs to establish well defined SERS. However it was found that a second ORC at 10 mV/s resulted in consistently intense SERS spectra. As a result, a series of 15 fast ORCs at 1 V/s followed by 2 slow ORCs at 10 mV/s was established as the standard pretreatment method with the anodic and cathodic limits set at 1.3 V and -1.56 V respectively.

A further examination of the effect of ORC sweep rate on SERS intensity was performed. The electrode was prepared as described above, after which the electrode was held at a potential of -1.06 V for 5 minutes, while a spectrum was recorded. It was then subjected to a cleaning cycle consisting of three rapid scans at 1 V/s from -1.06 V to +1.3 V and back, where the potential was held for 5 minutes, while a spectrum was recorded. This duplicates, as closely as possible, the experimental cleaning procedure employed by Jermann and Augustynski [103]. Figure 4.2 presents spectra for CO₂-saturated 0.1 M

Fig. 4.2: Spectra from the Cu Electrode at -1.06 V in CO₂-Saturated 0.1 M NaHCO₃, where each Cycle Represents 3 ORCs at 1 V/s
A) after initial preparation (t=3 min.) B) after 3 cycles (t=19 min.)
C) after 6 cycles (t=35 min.) D) after 9 cycles (t=51 min.)
E) after 11 cycles (t=61 min.)



NaHCO₃ after these cycles were performed. Bands at ca. 1640 and 3500 cm⁻¹ are attributable to the OH bend and OH stretch of bulk water, and are not SERS bands. The SERS bands at ca. 280, 358 and 2089 cm⁻¹ are attributable to adsorbed CO and at ~2900 cm⁻¹ to CH_x. Bands at ca. 1010 - 1075 cm⁻¹ are attributable to an interfacial carbonate species. The assignment of these bands is discussed in Section 4.2. The spectra shown in Fig. 4.2 (B-D) show a decrease in intensity of the SERS features after 3, 6 and 9 such cycles. After 11 of these cleaning cycles very little SERS intensity was observed (Fig. 4.2E). This demonstrates that it is not possible to observe SERS of the electrochemical reaction over an extended period of time in conjunction with 1 V/s cleaning cycles.

In order to assess the effect of the potential sweep rate on the SERS spectrum, a subsequent single cycle with the same potential limits was performed at 10 mV/s. This restored the SERS active surface as shown in Fig. 4.3A. Figure 4.3 (B-E) shows an increase in SERS intensity after each subsequent 10 mV/s ORC cycle.

Although cycling at 10 mV/s provides intense SERS, it is inefficient from an electrochemical standpoint. It takes 8 minute to complete a slow ORC cycle for each 5 minutes of reaction time. Fig. 4.4 compares the fast 1 V/s cleaning cycle waveforms to the 10 mV/s cleaning cycle waveforms. It can be seen that

Fig. 4.3: Spectra from the Cu Electrode at -1.06 V in CO₂-Saturated 0.1 M NaHCO₃, where each Cycle Represents 1 ORC at 10 mV/s (performed immediately following the cycles reported in Fig. 4.2)
A) after 1 cycle (t=74 min.) B) after 2 cycles (t=87 min.)
C) after 3 cycles (t=100 min.) D) after 4 cycles (t=113 min.)
E) after 5 cycles (t=126 min.)

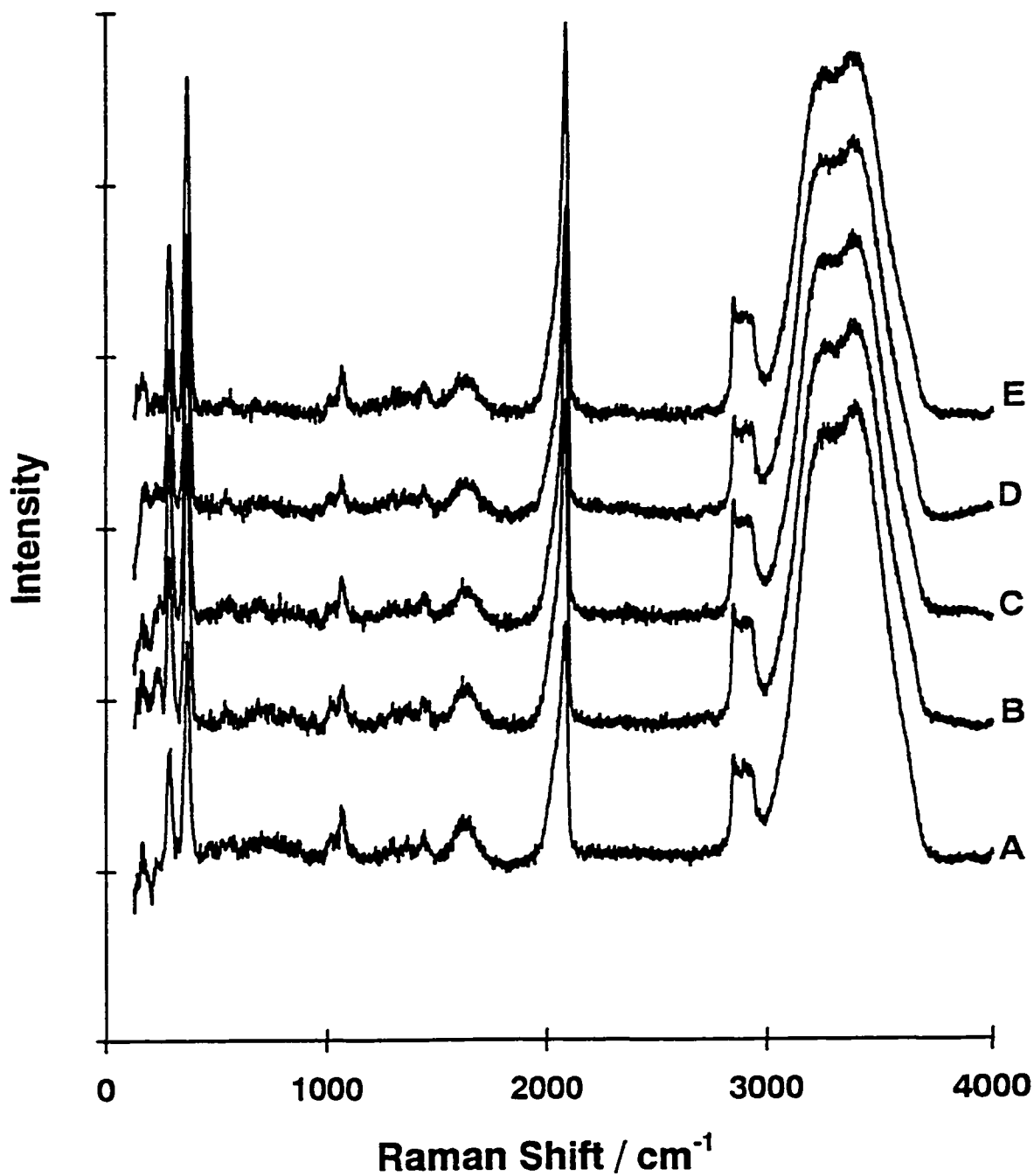
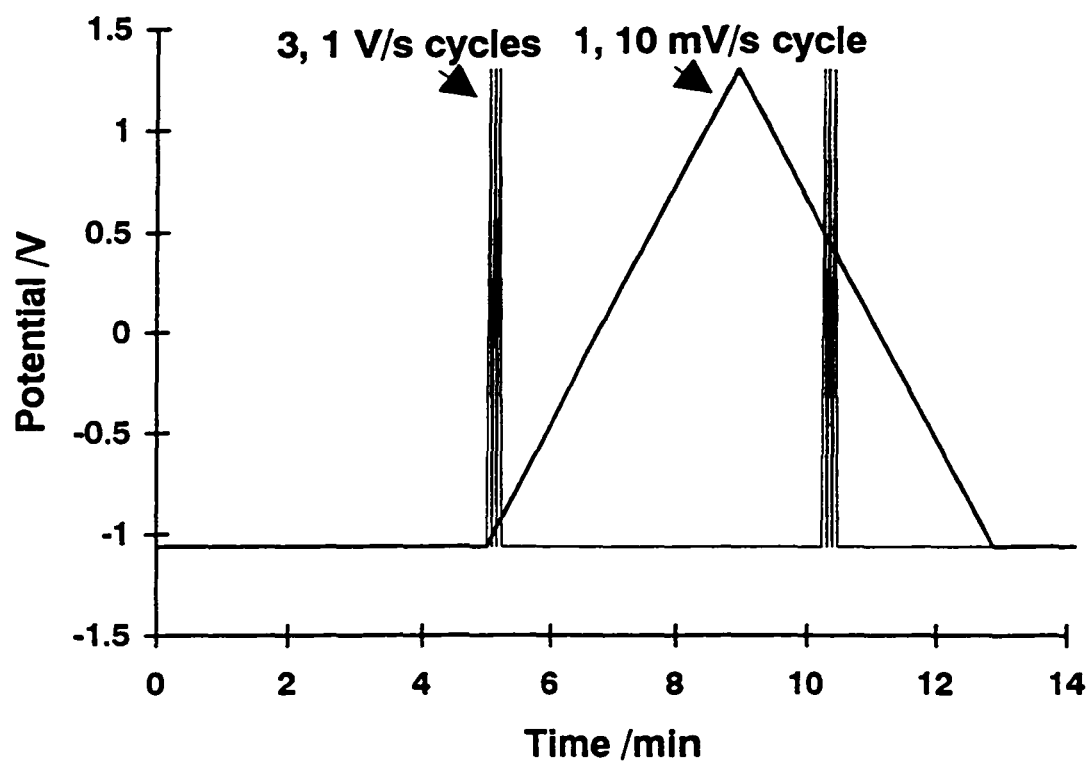


Fig. 4.4: A Comparison between 10 mV/s and 1 V/s Cleaning Cycles



with slower cycles considerably more time is spent sweeping the potential than is spent at the desired potential. Although 10 mV/s cycles are valuable for creating a SERS active surface, the time factor limits their usefulness as a method of cleaning the electrode for prolonging catalytic activity.

4.1.2 Voltammetry

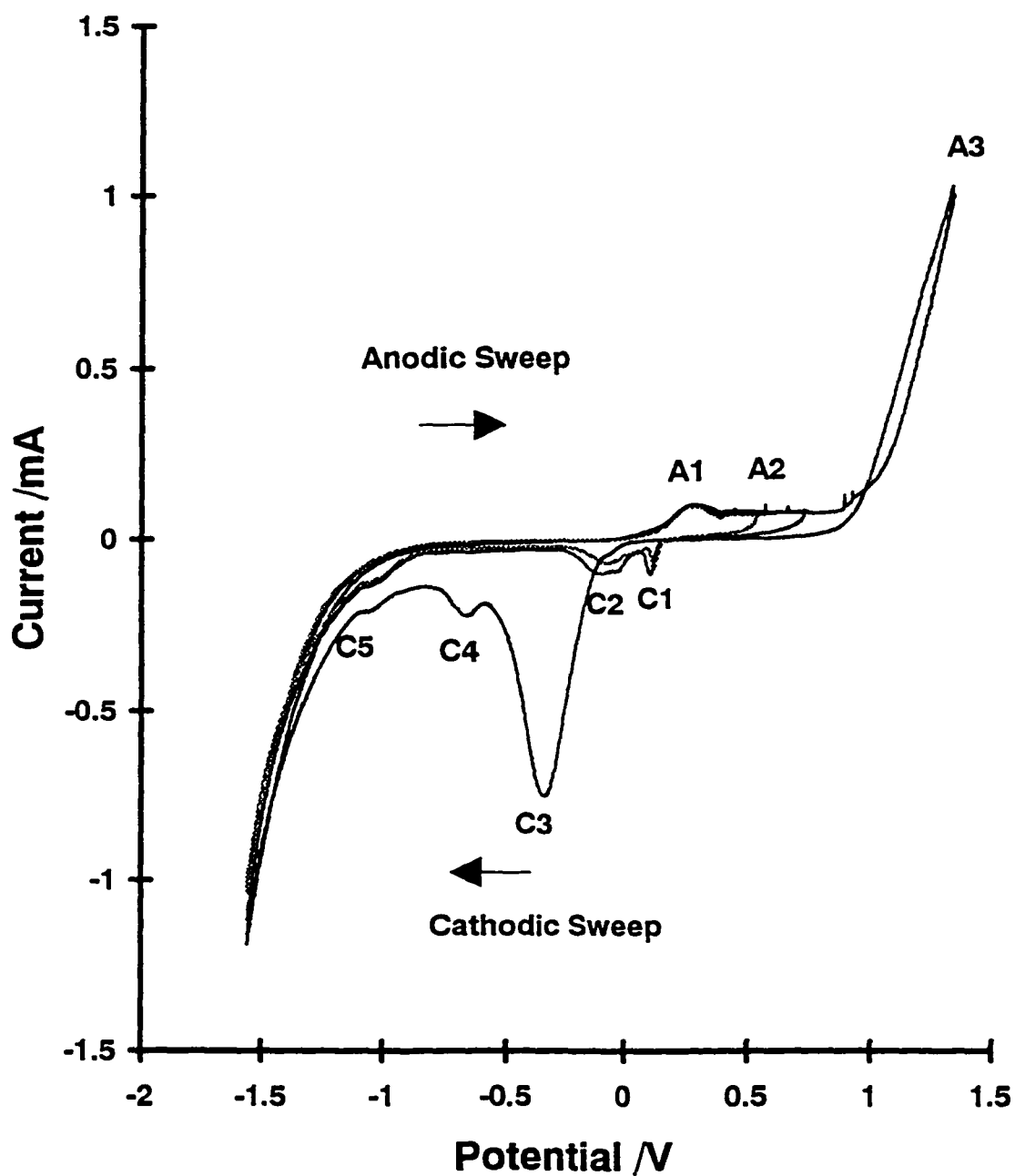
An intriguing aspect of this research was the ability to study the SERS of the films that were decomposing on the electrode surface. As noted previously, in order to produce SERS it is necessary to remove some metal from the surface and redeposit it on the electrode as a series of small features. For example, if silver is roughened in a perchlorate medium [114], the SERS active metal surface is expected to be formed by the dissolution of ions followed by their redeposition at more negative potentials. If a halide electrolyte is used the SERS active surface is created by the formation and decomposition of a halide film. It is often possible to observe the spectrum of the anion on the surface and this is well documented for halides [115]. Studying the decomposing film becomes more complex in other electrolytes, but may provide valuable information.

Because of the complexity of the Cu/CO₂/H₂O system, it is useful to examine the roughening process involved in the formation of the SERS active

surface. In this system, the SERS active surface is created by the formation and decomposition of a carbonate layer on the electrode. Figure 4.5 presents a set of 3 voltammograms run at 10 mV/s with different anodic limits. These voltammograms were run in the spectroelectrochemical cell in 0.1 M NaHCO₃, continuously saturated with CO₂ to duplicate the experimental conditions. After preparing the electrode by using the previously established pretreatment procedure, voltammograms were run with the anodic limits of 1.3, 0.74 and 0.54 V. The features recorded during the anodic scan of the voltammogram are labelled A1, A2, and A3. The A3 feature occurs only in the voltammogram where the upper limit was 1.3 V. The features A1 and A2 are present in all three voltammograms. The features observed during the cathodic scan are labelled as C1, C2, C3, C4, and C5. The large C3 and C4 features were only observed during the cathodic scan when the anodic limit was 1.3 V. The features C1 and C2 were only observed when the anodic limit was 0.74 or 0.54 V. The C5 feature was observed to some degree regardless of the anodic potential.

The voltammetric features are assigned in accordance with the literature [80]. The anodic peak (A1) at 0.29 V is assigned to the formation of a Cu⁺ oxide or hydroxide film. The subsequent plateau (A2) is assigned to its conversion to a CuO/Cu(OH)₂/basic copper carbonate layer. It appears that this process was followed by the dissolution of copper, occurring through the

Fig. 4.5: A Set of 3 Voltammograms Run at 10 mV/s with Anodic Limits of 1.3, 0.74 and 0.54 V for CO₂-Saturated 0.1 M NaHCO₃/Cu



carbonate layer, as indicated by the sharp rise in the anodic current at the anodic limit (A3). The large cathodic peak (C3) at -0.36 V and the feature (C4) at -0.66 V are assigned to the subsequent reduction of the layer formed during the anodic sweep. This results in the redeposition of copper, thus creating the SERS active surface.

The voltammograms with anodic limits of 0.74 and 0.54 V are similar to those reported by Perez-Sanchez et al. [80]. Based on their assignments, the peak labelled as C1 at ca. 0.1 V is attributed to the electroreduction of a CuO/Cu(OH)₂ to Cu₂O. The C2 peak (two overlapping peaks) is assigned to a soluble carbonate species at ca. -0.2 V and the electrochemical reduction of Cu₂O to Cu metal at ca. -0.3 V. These assignments are confirmed by the spectral results presented in Section 4.2.

A feature (C5) was observed at -1.06 V in all three of these voltammograms. According to Hori et al. [84,85], in this potential range for CO-saturated solution, there should be roughly 90% surface coverage of CO. It was found that this potential region provided a wealth of Raman spectral data, including bands attributable to adsorbed intermediates from both CO₂-saturated and CO-saturated solutions. These suggest that there is indeed a good surface coverage of intermediate species at this potential.

4.1.3 Potential Dependence

In order to further understand the electrochemical processes occurring during the ORC, potential dependence experiments were performed. In these experiments the electrode was cleaned as described in Chapter 2. No ORCs or potential cycling were used to prepare the surface. The electrode was held at fixed potentials, chosen based on the features observed from the voltammetry of the system (Fig. 4.5), while the SERS spectra were accumulated. By stepping to potentials in the A2 plateau region, it was anticipated that a surface film would be created. Stepping to potentials where the film was being decomposed was expected to create SERS active sites and provide information about the interfacial species.

This experiment was performed using two different solutions. The first solution was CO₂-saturated 0.1 M NaHCO₃. In this case the potential step sequence was:

OCP (ca. 0.14 V) → 0.24 V (a) → 0.64 V (a) → 0.04 V (a) → -0.36 V (a) →
-0.71 V (a) → 0.14 V → 0.24 V (b) → 0.64 V (b) → 0.04 V (b) →
-0.36 V (b) → -0.71 V (b) → -1.06 V → -1.76 V

The second solution was CO₂-saturated 0.1 M KHCO₃. In this case the potential step sequence was:

OCP (ca. 0.14 V) → 0.64 V (a) → 0.04 V (a) → -0.36 V (a) → -0.71 V (a) →
0.14 V → 0.24 V → 0.64 V (b) → 0.04 V (b) → -0.36 V (b) →
-0.71 V (b) → -1.06 V → -1.36 V → -1.76 V → -2.16 V → -2.56 V

4.1.3.1 CO₂-Saturated 0.1 M NaHCO₃

In Fig. 4.6 the spectra for the potential step sequence outlined for CO₂-saturated 0.1 M NaHCO₃ solution are shown, except the 0.24 V (a and b) spectra which were almost identical to the spectrum at OCP. The OH stretching band of bulk water consistently appeared as a broad band between ca. 2800 and 3800 cm⁻¹. Many of the bands observed were complex and contained overlapping components. This combined with the low intensity of some bands made it difficult to estimate the precise band position. This accounts for some apparent changes in band position. Where peak position is poorly defined a range of wavenumbers is provided. Table 4.1 lists the approximate band positions and tentative band assignments. The data from these experiments will be used in Section 4.2, where band assignments are discussed.

Fig. 4.6: Spectra from the Cu Electrode in CO₂-Saturated 0.1 M NaHCO₃ for Potential Step Experiments

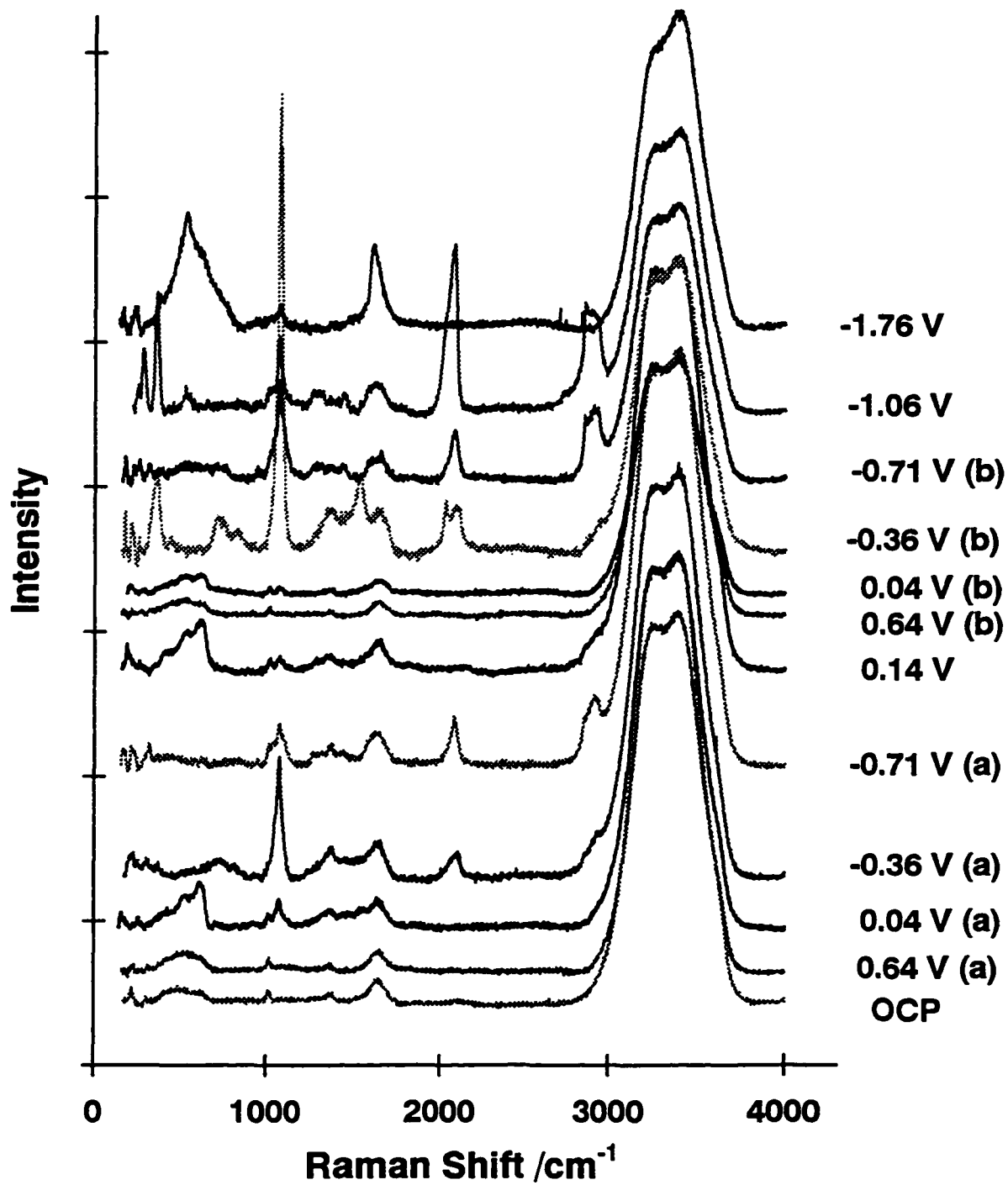


Table 4.1: Band Assignments from CO₂-Saturated 0.1 M NaHCO₃/Cu for Potential Step Experiments

	Cu-CO	Cu-OCO ₂	Cu-O	Poison	HCO ₃ ⁻	CO ₃ ²⁻	Unassigned	C _{gr}	H ₂ O	CO	CH
OCP			320-680		1015		1350-1390		1640		
0.64 V (a)			320-680		1015		1350-1390		1640		
0.04 V (a)			398 520 615		1015	1073	1368	1400-1590	1635		
-0.36 V (a)					1015	720 820 1049 1071	1369		1635	2045 2096	~2900
-0.71 V (a)					1010	1049 1071	1290-1485		1626	2034 2080	~2900
0.14 V			408 527 615		1015	1072	1290-1485		1645		~2900
0.64 V (b)			320-680		1015		1350-1390		1640		
0.04 V (b)			320-680		1015	1074	1350-1390		1640		
-0.36 V (b)		356			1015	720 829 1049 1073	1365	1531	1645	2028 2092	~2900
-0.71 V (b)					1015	1049 1071	1220-1480		1626	2028 2079	~2900
-1.06 V	275 356			525	1020	1067	1280		1620	2075	1440 ~2900
-1.76 V				525	1015	1072			1608		

At OCP and 0.64 V (a) all of the bands were low in intensity. The broad band ca. 320 - 680 cm^{-1} may be from a copper oxide species. A small band at ca. 1015 cm^{-1} is attributable to the solution phase HCO_3^- ion. A broad band, possibly consisting of two components, at ca. 1350 - 1390 cm^{-1} may arise from either HCO_3^- or CO_3^{2-} . At ca. 1640 cm^{-1} a small band attributable to the HOH bend of water was observed. Although the voltammogram (Fig. 4.5) indicated that a film was formed at these potentials (A2), the only spectral feature associated with this surface film was the band at ca. 320 - 680 cm^{-1} which was weak in intensity.

By stepping the potential to 0.04 V (a) (just past Fig. 4.5 (C1)), where the film is reduced, it was possible to observe the SERS spectrum of the reduction products. The band which had been observed ca. 320 - 680 cm^{-1} increased in intensity and appeared to be composed of three peaks. New bands appeared at ca. 1073 cm^{-1} , attributed to a carbonate, and ca. 1400 - 1590 cm^{-1} (two components), possibly related to graphitic carbon.

When the potential was lowered to -0.36 V (a) (Fig. 4.5 (C3)), another series of bands appeared. Four of the new bands which appeared were a broad band at ca. 720 cm^{-1} and a small band at ca. 820 cm^{-1} , associated with a carbonate, two weak bands at ca. 2045 and 2096 cm^{-1} , attributed to a CO stretch, and a weak band at ~ 2900 cm^{-1} , related to the CH stretching mode of

an adsorbed CH_x . The band at ca. 1071 cm^{-1} appeared as an intense peak with a small shoulder at ca. 1015 cm^{-1} and a larger shoulder at ca. 1049 cm^{-1} . The new shoulder at ca. 1049 cm^{-1} is related to carbonate. The increased band intensity indicates a high concentration of carbonate ions in the interface. No bands attributable to a CuO stretch or graphitic carbon were observed.

At -0.71 V (a) (just past Fig. 4.5 (C4)), the intensity of the bands in the carbonate region decreased. This decrease in intensity suggests that the film was being removed. The bands at ca. 720 and 820 cm^{-1} were not observed. A weak band, possibly made up of three components, was observed at ca. $1290 - 1485\text{ cm}^{-1}$, but not assigned. The band attributed to the HOH bend of water shifted to ca. 1626 cm^{-1} . The band at ca. 2096 cm^{-1} (-0.36 V (a)) shifted to ca. 2080 cm^{-1} and became more intense. The intensity $\sim 2900\text{ cm}^{-1}$ band also increased. This is just *before* the region where the onset of CO_2 reduction would be expected.

When the potential was stepped to 0.14 V (just before Fig. 4.5 (A1)) many of the band positions were similar to those observed at 0.04 V (a). The major differences at 0.14 V were the observation of a weak band at $\sim 2900\text{ cm}^{-1}$, the bands at ca. 1368 and $1400 - 1590\text{ cm}^{-1}$ (0.04 V (a)) were replaced by a broad band at $1220 - 1485\text{ cm}^{-1}$, and the intensity of the ca. 1072 cm^{-1} band decreased.

Bands at 0.64 V (a) and 0.64 (b) (Fig. 4.5 (A2)) were almost identical, as were the bands at 0.04 V (a) and 0.04 V (b). However, at 0.04 V (b) all bands were less intense than at 0.04 V (a). As well, at 0.04 V (b), the peaks in the ca. 320 - 680 cm^{-1} band were less defined than at 0.04 V (a). The band at ca. 1400 - 1590 cm^{-1} (0.04 V (a)) was not observed at 0.04 V (b).

Comparing -0.36 V (a) and -0.36 V (b), the relative intensity of all the bands, except the band at ~ 2900 , increased greatly at -0.36 V (b). At -0.36 V (b) additional bands, not seen at -0.36 V (a), were observed at ca. 356 cm^{-1} , attributed to a Cu-OCO₂ and at ca. 1531 cm^{-1} , which may be related to graphitic carbon. The band at ca. 356 cm^{-1} was similar to the band that was assigned to the Cu-OCO₂ mode for [Cu(CO₃)₂]²⁻ ion in solution [77]. The 2045 cm^{-1} shoulder (-0.36 V (a)) sharpened and appeared at 2028 cm^{-1} (-0.36 V (b)).

At -0.71 V (b) many of the bands were similar to those observed at -0.71 V (a). However, at -0.71 V (b) the band at ca. 1071 cm^{-1} was much more intense with less distinct shoulders than at -0.71 V (a). Numerous changes occurred between -0.36 V (b) and -0.71 V (b). At -0.71 V (b), the bands at ca. 356, 720, 829, and 1531 cm^{-1} disappeared. The band at 1365 cm^{-1} (-0.36 V (b)) was replaced by a broad band at ca. 1220 - 1480 cm^{-1} . The ca. 1071 cm^{-1} band was less intense than at -0.36 V (b). The peaks assigned to CO (2028 and

2092 cm^{-1} at -0.36 V (b)) appeared as almost a single band at ca. 2079 cm^{-1} as the ca. 2028 cm^{-1} shoulder became less prominent. The band at ~2900 cm^{-1} became more intense than at -0.36 V (b). The band at ca. 1640 cm^{-1} (-0.36 V (b)) shifted to ca. 1626 cm^{-1} .

As the potential was lowered to -1.06 V (Fig. 4.5 (C5)) three bands at ca. 275, 356, 525 cm^{-1} appeared. The ca. 2079 cm^{-1} (-0.71 V (b)) band shifted to ca. 2075 cm^{-1} and became more prominent. The intensity of the broad band at ~2900 cm^{-1} also increased from -0.71 V (b). The broad 1220 - 1480 cm^{-1} feature (-0.71 V (b)) appeared as a broad band at ca. 1280 cm^{-1} and a weak band at ca. 1440 cm^{-1} . The new band at 1440 cm^{-1} may be related to a CH_x species.

At the lowest potential, -1.76 V, the band at ca. 525 cm^{-1} became broad and more intense. The bands ca. 275, 356, 1280, 1440, 2075, and ~2900 cm^{-1} disappeared. As well, the 1620 cm^{-1} (-1.06 V) was replaced by a strong band at 1608 cm^{-1} which may be due to the enhanced bending mode of water as discussed by Chen and Tian [94].

4.1.3.2 CO_2 -Saturated 0.1 M KHCO_3

Spectra of the potential step sequence using CO_2 -saturated 0.1 M KHCO_3 solution are shown in Fig. 4.7. As in the previous solution, the band from the

Fig. 4.7: Spectra from the Cu Electrode in CO₂-Saturated 0.1 M KHCO₃ for Potential Step Experiments

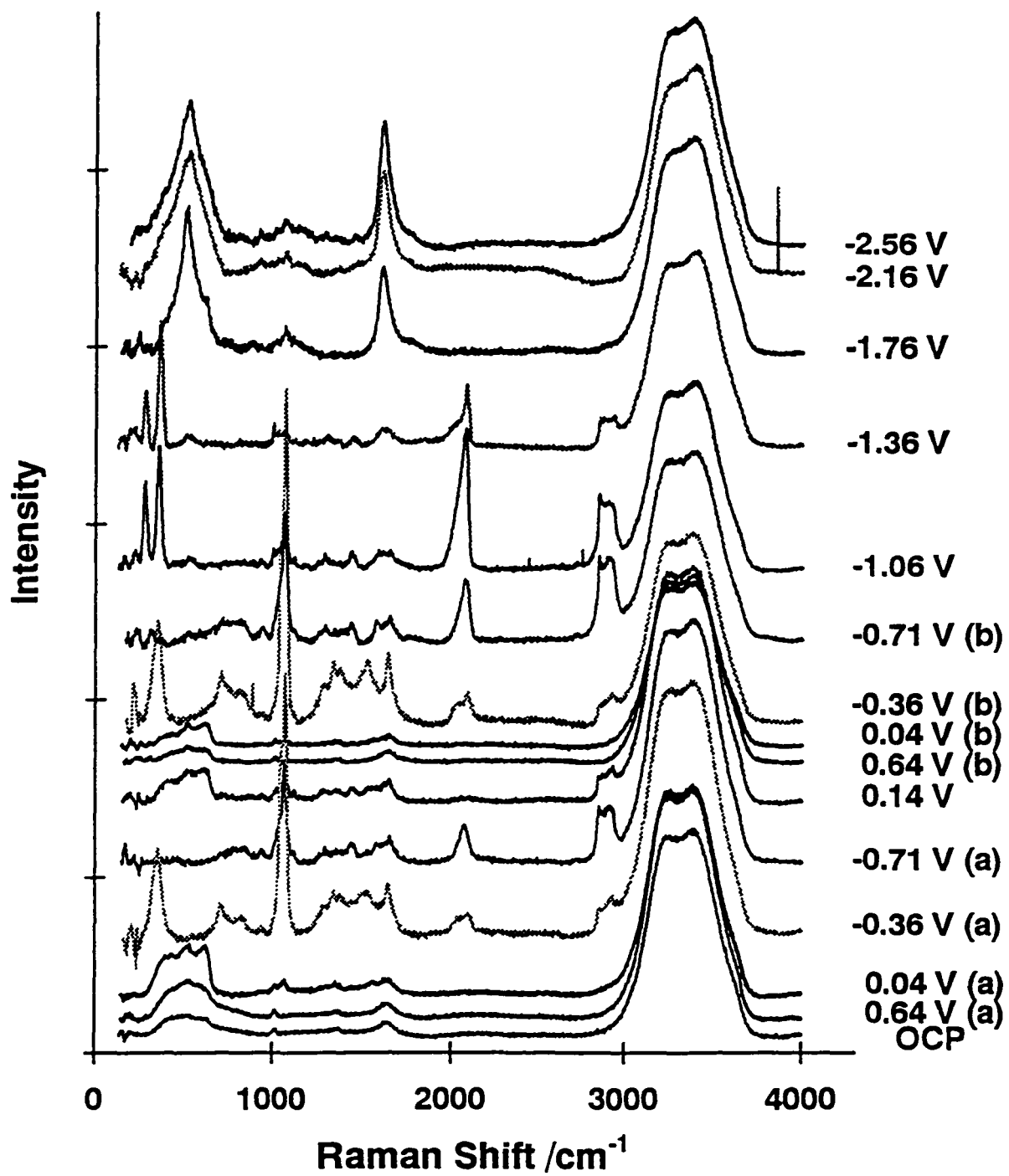


Table 4.2: Band Assignments from CO₂-Saturated 0.1 M KHCO₃/Cu for Potential Step Experiments

	Cu-CO	Cu-OCO ₂	Cu-O	Poison	HCO ₃ ⁻	CO ₃ ²⁻	Unassigned	C ₂	H ₂ O	CO	CH
OCP			320-680		1013		1350-1390		1633		
0.64 V (a)			320-680		1012		1350-1390		1640		
0.04 V (a)			398 520 615		1012	1064	1352	1400- 1590	1635		
-0.36 V (a)		347			1013	702 824 1050 1071	1290 1343 1385	1400- 1590	1644	2033 2092	-2900
-0.71 V (a)					1013	1044 1069	1290-1485	1573	1645	2032 2074	-2900
0.14 V			395 519 615		1020	1067	1296 1362		1650		1443 -2900
0.64 V (b)			320-680		1012		1350-1390		1640		
0.04 V (b)			390 518 615		1013	1070	1350-1390		1640		
-0.36 V (b)		348			1013	705 813 1049 1070	1285 1342 1379	1528	1649	2027 2085	-2900
-0.71 V (b)					1013	1048 1070	1297	1579	1650	2080	1435 -2900
-1.06 V	276 355			527	1013	1065	1298	1592	1655	2077	1436 -2900
-1.36 V	279 359			516	1013	1069			1620	2008 2082	1434 -2900
-1.76 V				380 507 620	1013	1069			1608		

OH stretch of bulk water consistently appeared as a broad band between ca. 2800 and 3800 cm^{-1} . Table 4.2 lists the approximate band positions and tentative band assignments. Because of the complex, overlapping, and low intensity of some bands, the band positions were estimated and where peak position was poorly defined ranges are given. This accounts for some apparent changes in band position. The data from these experiments will be used in Section 4.2, where band assignments are discussed.

At OCP, 0.64 (a), 0.04 (a), -0.71 (a), and 0.14 V the bands were similar to those presented for CO_2 -saturated 0.1 M NaHCO_3 solution. However, with CO_2 -saturated 0.1 M KHCO_3 solution at these potentials some notable differences exist. At 0.04 V (a) the lower wavenumber component of the ca. 320 - 680 cm^{-1} band was more intense from CO_2 -saturated 0.1 M KHCO_3 . Also from this solution at -0.71 V (a) the band which may be attributed to graphitic carbon was observed, and the band envelope at ca. 1071 cm^{-1} was more intense. At 0.14 V the band at ca. 1290 - 1485 cm^{-1} appeared as three components at ca. 1296, 1362 and 1443 cm^{-1} and the band at ~ 2900 cm^{-1} was more intense from CO_2 -saturated 0.1 M KHCO_3 .

Spectra from the potential steps at 0.64 (b), 0.04 (b), -0.71 (b), -1.06, and -1.76 V were also very similar for both solutions. However, some differences with CO_2 -saturated 0.1 M KHCO_3 solution occurred for these potentials as well.

At 0.04 V (b) the band at ca. 320 - 680 cm^{-1} appeared as three peaks at ca. 390, 518 and 615 for CO_2 -saturated 0.1 M KHCO_3 . For this solution at -0.71 V (b) the band at 1220 - 1480 cm^{-1} appeared as two components at ca. 1297 and 1435 cm^{-1} . As well, bands were observed at ca. 1579 and 1592 at -0.71 V (b) and -1.06 V respectively. At -1.76 V the band at 525 cm^{-1} appeared as three peaks at ca. 380, 507, and 620 cm^{-1} for CO_2 -saturated 0.1 M KHCO_3 .

Spectra from CO_2 -saturated 0.1 M NaHCO_3 and KHCO_3 solutions at -0.36 V (a and b) show a number of differences. At -0.36 V (a) for the CO_2 -saturated 0.1 M KHCO_3 solution, bands at ca. 347 and 1400 - 1590 cm^{-1} appeared. These bands do not appear until -0.36 V (b) for CO_2 -saturated 0.1 M NaHCO_3 solution. At -0.36 V (a and b) the bands at ca. 1369/1365 cm^{-1} appeared as three components at ca. 1290/1285, 1343/1342, and 1385/1379 cm^{-1} for CO_2 -saturated 0.1 M KHCO_3 solution. All bands except the band at ca. 2085 cm^{-1} were more intense from CO_2 -saturated 0.1 M KHCO_3 solution.

The potential was decreased to -1.36, -2.16, -2.56 V only with CO_2 -saturated 0.1 M KHCO_3 solution. At -1.36 V the bands at ca. 279 and 359 cm^{-1} became prominent and a small band at ca. 516 cm^{-1} was still present. The band ca. 1069 cm^{-1} decreased but the shoulder component was still present. The band at ca. 2082 cm^{-1} had a shoulder at 2008 cm^{-1} and intensity of this band decreased. The band intensity ca. 2900 cm^{-1} has decreased as well. As

the potential was further lowered to -2.16 and -2.56 V, only some weak bands in the carbonate stretching region and two intense bands at ca. 525 and 1608 cm^{-1} remained.

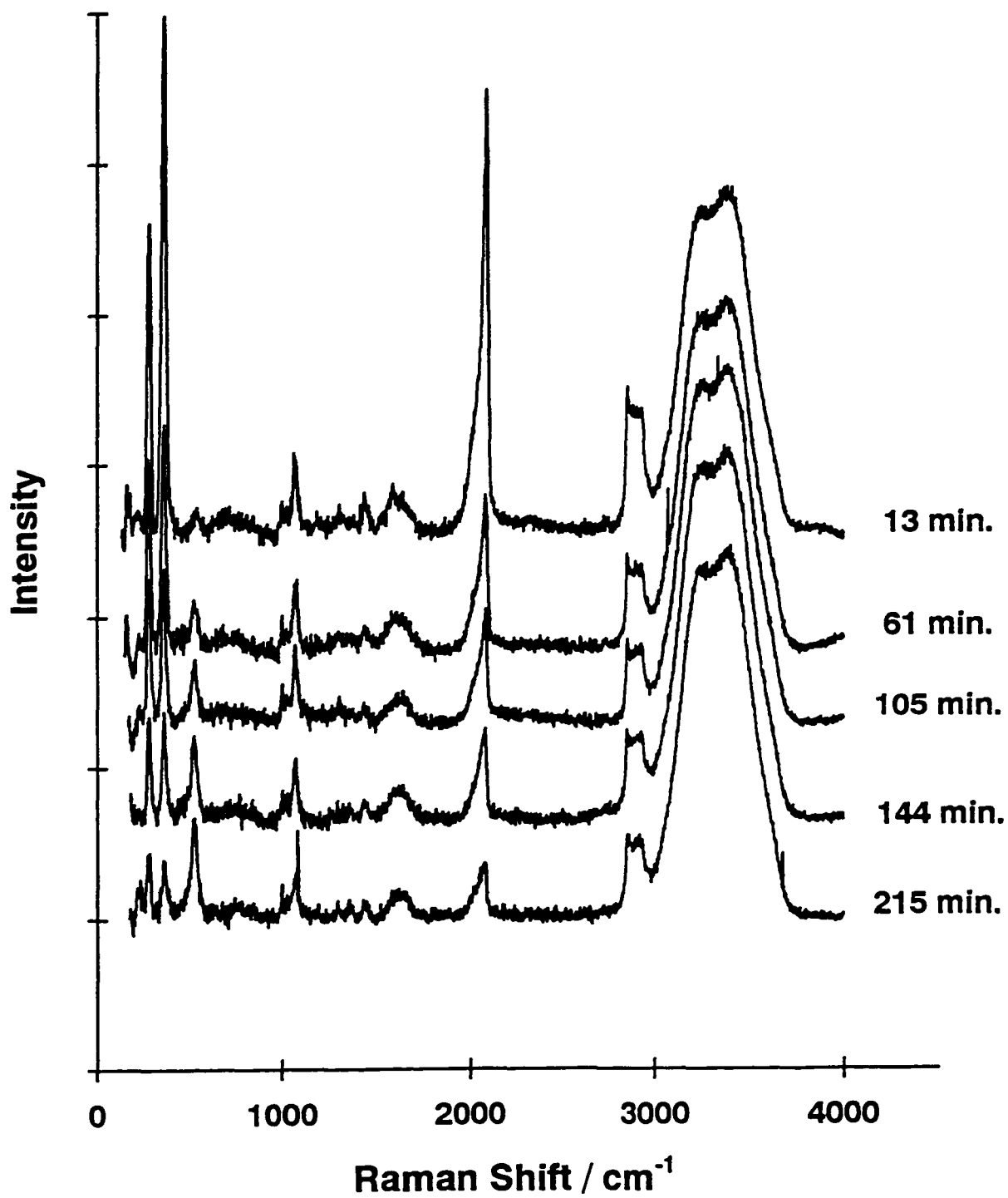
4.1.4 Time Dependence

Jermann and Augustynski [103] established that the CO_2 reduction reaction is readily poisoned. To explore this poisoning, experiments were undertaken to determine how the spectra of CO_2 reduction changed over time. The data from these experiments will be further discussed in relationship to band assignments in Section 4.2.

For all time dependence experiments, the electrode surface was prepared using the previously established pretreatment process, i.e., fifteen 1 V/s ORCs followed by two 10 mV/s ORCs, in order to ensure consistency. During the cathodic sweep of the final slow ORC the potential was stopped at -1.06 V and held while the Raman spectra were collected. The electrolytes used for these experiments were CO_2 -saturated 0.1 M NaHCO_3 , CO-saturated 0.1 M NaHCO_3 , and CO_2 -saturated 0.1 M KDCO_3 solutions.

Figure 4.8 presents spectra of the CO_2 -saturated 0.1 M NaHCO_3 solution accumulated after 13, 61, 105, 144, and 215 minutes of reaction time. Bands at

Fig. 4.8: Time Dependence Spectra from the Cu Electrode at -1.06 V in CO₂-Saturated 0.1 M NaHCO₃



ca. 280, 358, and 2089 cm^{-1} are assigned to the Cu-CO frustrated rotation, the Cu-CO stretch, and CO stretch of an adsorbed CO. Based on the spectra, it is apparent that as the length of reaction time increased the intensity of all these bands decreased. The rate at which the intensity decreased was greatest for the CO stretch and least for the Cu-CO frustrated rotation. The band at $\sim 2900 \text{ cm}^{-1}$, attributed to CH_x , also showed a very slight decrease in intensity over time. The band at ca. 523 cm^{-1} is related to the poisoning of the reaction. The intensity of this band increased with the length of reaction time. All other bands remained virtually unchanged over time.

Similar spectral bands were observed from CO-saturated 0.1 M NaHCO_3 solution. Spectra accumulated after 13, 30, and 60 minutes of reaction time are shown in Fig. 4.9. The adsorbed CO bands at ca. 281, 357, and 2091 cm^{-1} all showed a decrease in intensity over time. The band at $\sim 2900 \text{ cm}^{-1}$, attributed to CH_x , also showed a very slight intensity decrease over time. The intensity of the poisoning band at ca. 527 cm^{-1} increased with the length of reaction time. The reaction time has no significant effect on the other bands.

The spectra recorded for CO_2 -saturated 0.1 M KDCO_3 solutions show similar spectral band changes. Figure 4.10 presents spectra recorded after 14, 61, 104, and 143 minutes of reaction time. Adsorbed CO bands at ca. 280, 356, and 2089 cm^{-1} showed a decrease in intensity over time similar to the

Fig. 4.9: Time Dependence Spectra from the Cu Electrode at -1.06 V in CO-Saturated 0.1 M NaHCO₃

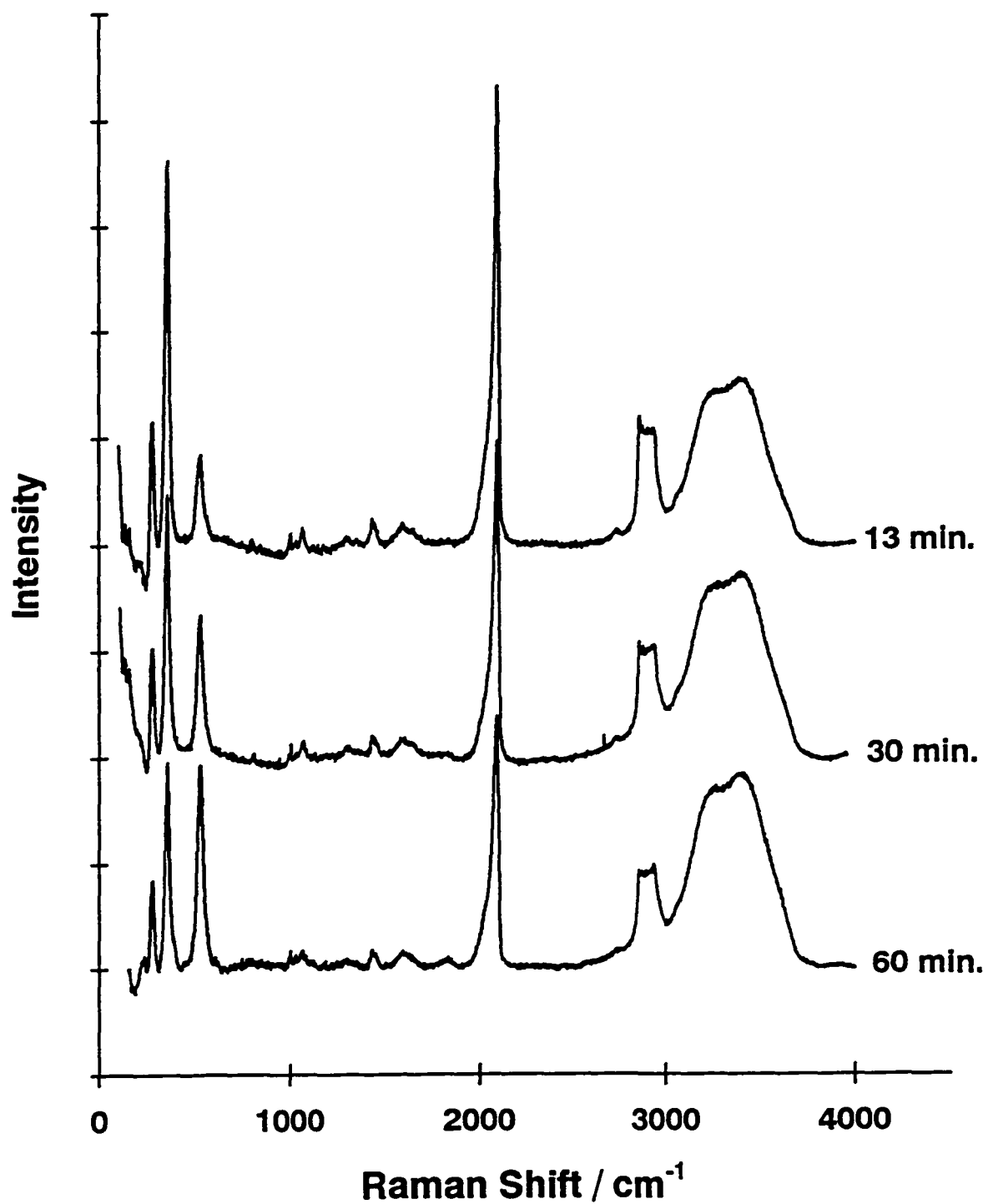
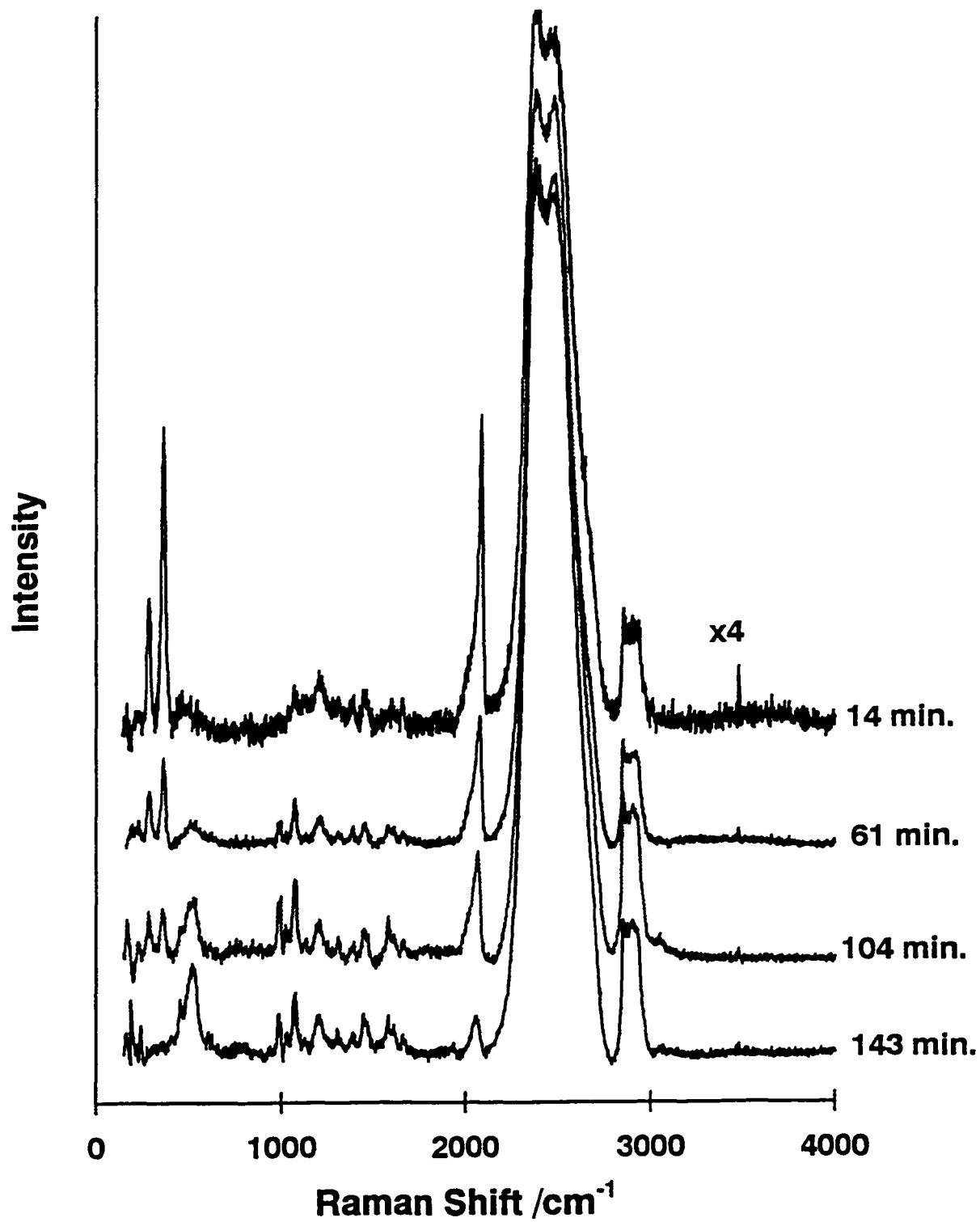


Fig. 4.10: Time Dependence Spectra from the Cu Electrode at -1.06 V in CO₂-Saturated 0.1 M KDCO₃



CO-saturated and CO₂-saturated 0.1 M NaHCO₃ solutions. The band for the poisoning species appeared to be composed of two peaks at ca. 452 and 515 cm⁻¹. The intensity of this band increased over time. It also appears that the band at ~2900 cm⁻¹ increased with reaction time. The other bands showed no significant variation in intensity.

4.1.5 Poisoning Species

In order to identify the poisoning species, further experiments were performed using CO₂-saturated 0.1 M NaHCO₃. After creating a SERS active surface using the standard pretreatment procedure, the final working potential was held at -1.76 V for 163 minutes. This resulted in a large build up of the poisoning species. The potential was then stepped to 1.0 V, in 0.1 V increments. It was subsequently stepped from 1.0 to -0.6 V, in 0.2 V increments. After this the potential was stepped to -1.26 and -1.76 V.

Figure 4.11 presents the spectra recorded at selected potentials. The band positions associated with the poisoning species are listed in Table 4.3. These spectra show that the shape and position of the poisoning band changes with potential. The spectra also show the region between ca. 250 and 400 cm⁻¹, where bands attributed to the Cu-CO frustrated rotation and Cu-CO stretch of adsorbed CO occur.

Fig. 4.11: Spectra of the Poisoning Species from the Cu Electrode at Various Potentials in CO₂-Saturated 0.1 M NaHCO₃

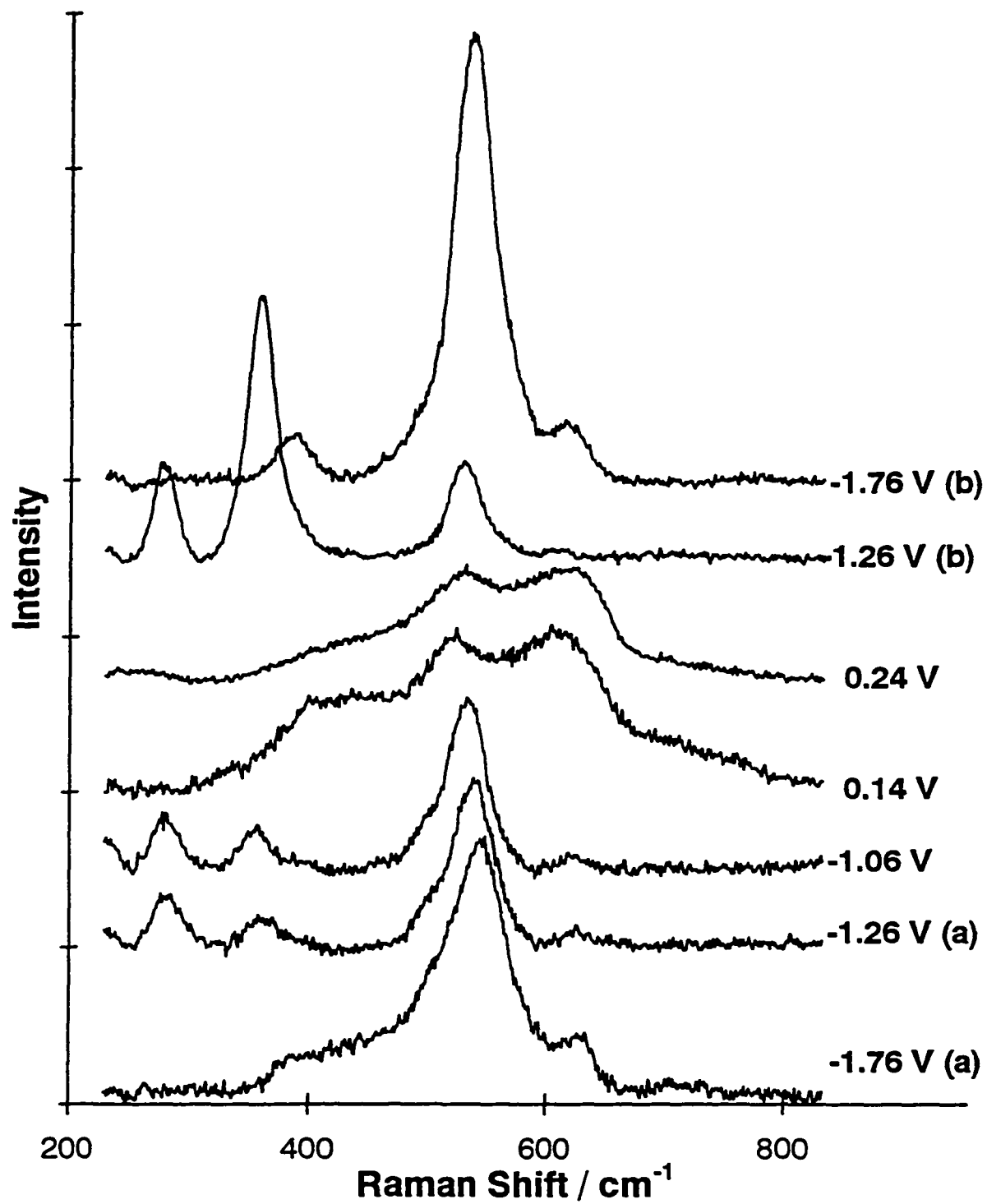


Table 4.3: Band Assignments for the Poisoning Species at Various Potentials from Figure 4.11; CO₂-Saturated 0.1 M NaHCO₃/Cu

Potential	Cu-CO	Poison			
-1.76 V		390	500	542	625
-1.26 V	280 360	500	536	625	
-1.06 V	280 360	495	530	623	
+0.14 V		400	518	603	
+0.24 V		400	529	616	
-1.26 V	280 360		527	610	
-1.76 V		390	534	616	

Initially, at -1.76 V (a), the band from the poisoning species was observed as an intense band at ca. 542 cm^{-1} with two lower wavenumber shoulders at ca. 390 and 500 cm^{-1} , and a higher wavenumber shoulder at ca. 625 cm^{-1} . No bands from adsorbed CO were observed.

These poisoning bands decreased in intensity as the potential was stepped to -1.26 (a) and -1.06 V and adsorbed CO bands were observed at ca. 280 and 360 cm^{-1} . The poisoning band shifted to ca. 536 cm^{-1} , the shoulder at ca. 390 cm^{-1} disappeared. The shoulder at ca. 500/495 cm^{-1} showed little change and the shoulder at ca. 625 cm^{-1} decreased in intensity.

At 0.14 and 0.24 V, the intensities of the poisoning bands changed and no CO bands were observed. For 0.14 V, the poisoning band shifted to ca. 518 cm^{-1} and was less intense. Only one of the low wavenumber shoulders, ca. 400 cm^{-1} , was apparent. The higher wavenumber shoulder shifted to ca. 603 cm^{-1} and its intensity relative to the main poisoning band increased dramatically. For 0.24 V, the poisoning band shifted to ca. 529 cm^{-1} . The shoulder at ca. 400 cm^{-1} became very weak. The higher wavenumber shoulder shifted to ca. 616 cm^{-1} .

During the second step to -1.26 V (b), the intensity of the poisoning bands relative to the adsorbed CO bands, ca. 280 and 360 cm^{-1} , decreased

significantly. The poisoning band was at ca. 527 cm^{-1} , and neither of the lower wavenumber shoulders was apparent. The higher wavenumber shoulder shifted to ca. 610 cm^{-1} and decreased in intensity.

At -1.76 V (b), the poisoning band was very intense and the CO bands disappeared. The poisoning band shifted to ca. 534 cm^{-1} and the second lower wavenumber shoulder was not apparent. The first lower wavenumber shoulder appeared as a band at ca. 390 cm^{-1} . The higher wavenumber shoulder shifted to ca. 616 cm^{-1} and its intensity increased.

4.2 Discussion of Band Assignments

The experiments previously described yielded a series of interrelated results which are helpful in assigning the observed spectral bands. The voltammetry of the copper electrode in the bicarbonate media identified potentials where changes in the $\text{Cu}/\text{CO}_2/\text{H}_2\text{O}$ system were expected. Using this information, the SERS spectra of the adsorbed species at various potentials were collected and compared. As well spectra of the reaction were obtained over time in order to assess the time dependence of the reaction.

In this section the experimental results are compared with the literature as presented in Chapter 3. Experiments specific to the identification of the

observed bands are introduced. Band assignments are made for adsorbed CO, CH_x species, carbonate and bicarbonate, oxides, and poisoning species.

4.2.1 Adsorbed CO

According to the literature CO is believed to be an intermediate in the reduction of CO₂ on copper [38,39,102]. For both CO₂-saturated 0.1 M NaHCO₃ (Fig. 4.6) and KHCO₃ (Fig. 4.7), one or three bands attributed to adsorbed CO were observed; their position depended on potential and electrolyte solution. The band, between ca. 2074 and 2096 cm⁻¹, assigned to the CO stretch, had a shoulder at between ca. 2008 and 2045 cm⁻¹. The band attributed to the Cu-CO frustrated rotation was observed between ca. 275 and 279 cm⁻¹. The band attributed to the Cu-CO stretch was recorded between ca. 355 and 359 cm⁻¹. These band positions are similar to those presented in the literature as discussed in Chapter 3.4.1. Thus, the vibrational modes have been assigned in accordance with this literature.

The potential dependence experiments showed that bands attributable to the CO stretch of adsorbed CO were observed at all negative potential steps more positive than -1.76 V in both CO₂-saturated 0.1 M NaHCO₃ and KHCO₃ solutions. Spectra illustrating differences in shape and intensity of the CO stretching band with changes in potential are shown in Fig. 4.12

(CO₂-saturated 0.1 M NaHCO₃) and Fig. 4.13 (CO₂-saturated 0.1 M KHCO₃). These spectra were acquired concurrently with those in Fig. 4.6 and Fig. 4.7 using the fixed grating mode. For both these solutions this band became very intense around -1.06 V, which is where the C5 feature of the voltammogram (Fig. 4.5) appears.

At -0.36 V (a and b) and -0.71 V (a) for both solutions, the CO-stretching band had a shoulder, between ca. 2008 and 2045 cm⁻¹. At -0.71 (b) and -1.06 V, the band shoulder diminished although the band continued to be skewed to lower wavenumbers. For CO₂-saturated 0.1 M KHCO₃ the shoulder intensity increased when the potential was stepped to -1.36 V. The asymmetry of this band is consistent with the band shape reported in the literature for disordered and polycrystalline copper surfaces [43,81,84-86]. Bands attributed to the Cu-CO frustrated rotation and Cu-CO stretch were seen at a potential of -1.06 V from both solutions and -1.36 V with CO₂-saturated 0.1 M KHCO₃

These results are similar to those presented by Oda et al. [43]. However, they did not observe any adsorbed CO bands until -1.4 V, where the Cu-Cl band disappeared. Also, the band that they observed at ca. 1934 to 1980 cm⁻¹ was not observed in this work. Since their study used 3.5 M KCl as the electrolyte, it is probable that Cl⁻ blocked the adsorption site for CO at potentials above -1.4 V. As well, the ca. 1934 to 1980 cm⁻¹ band may be related

Fig. 4.12: Spectra from the Cu Electrode in CO₂-Saturated 0.1 M NaHCO₃ for the CO Stretching Region

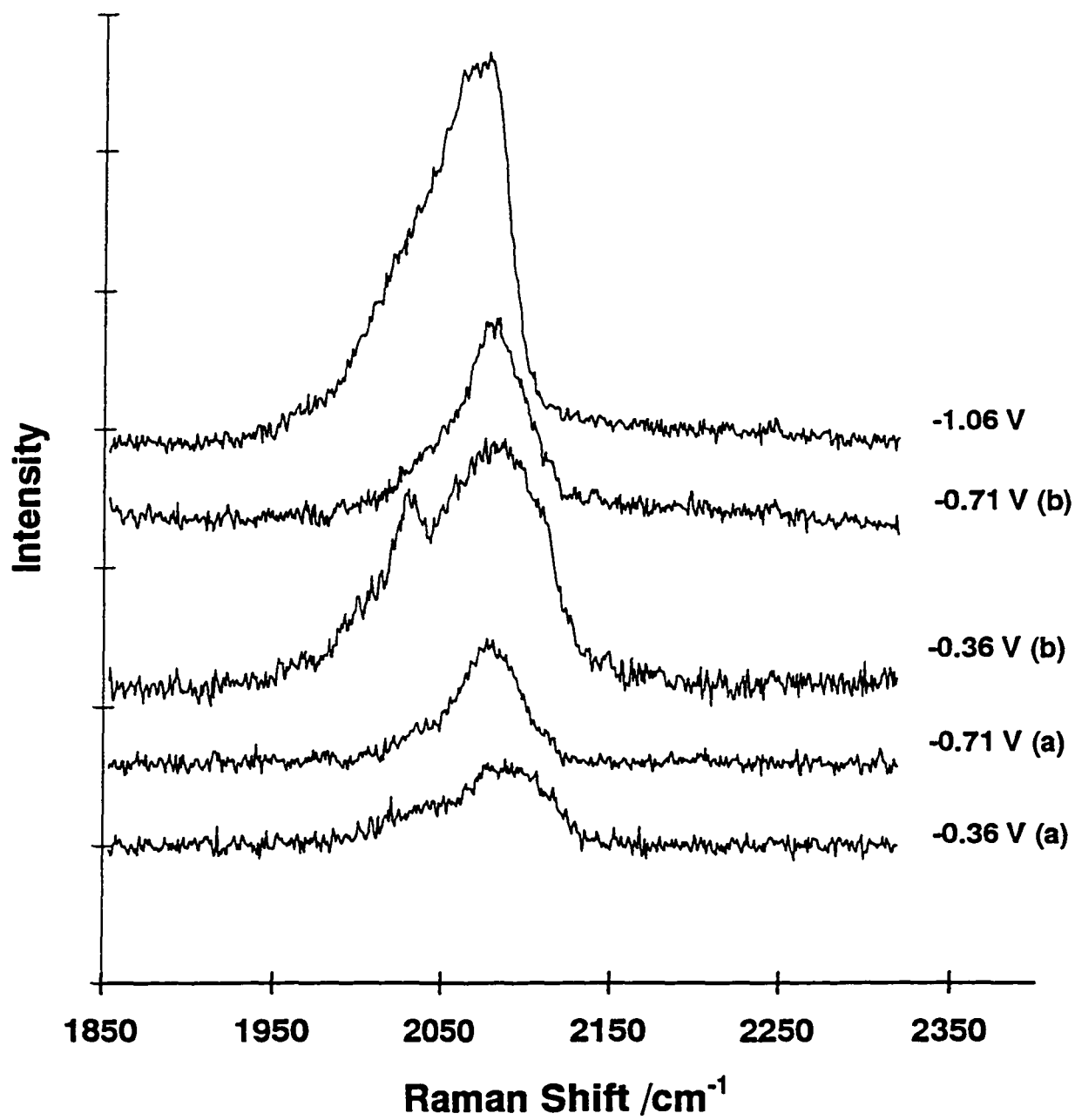
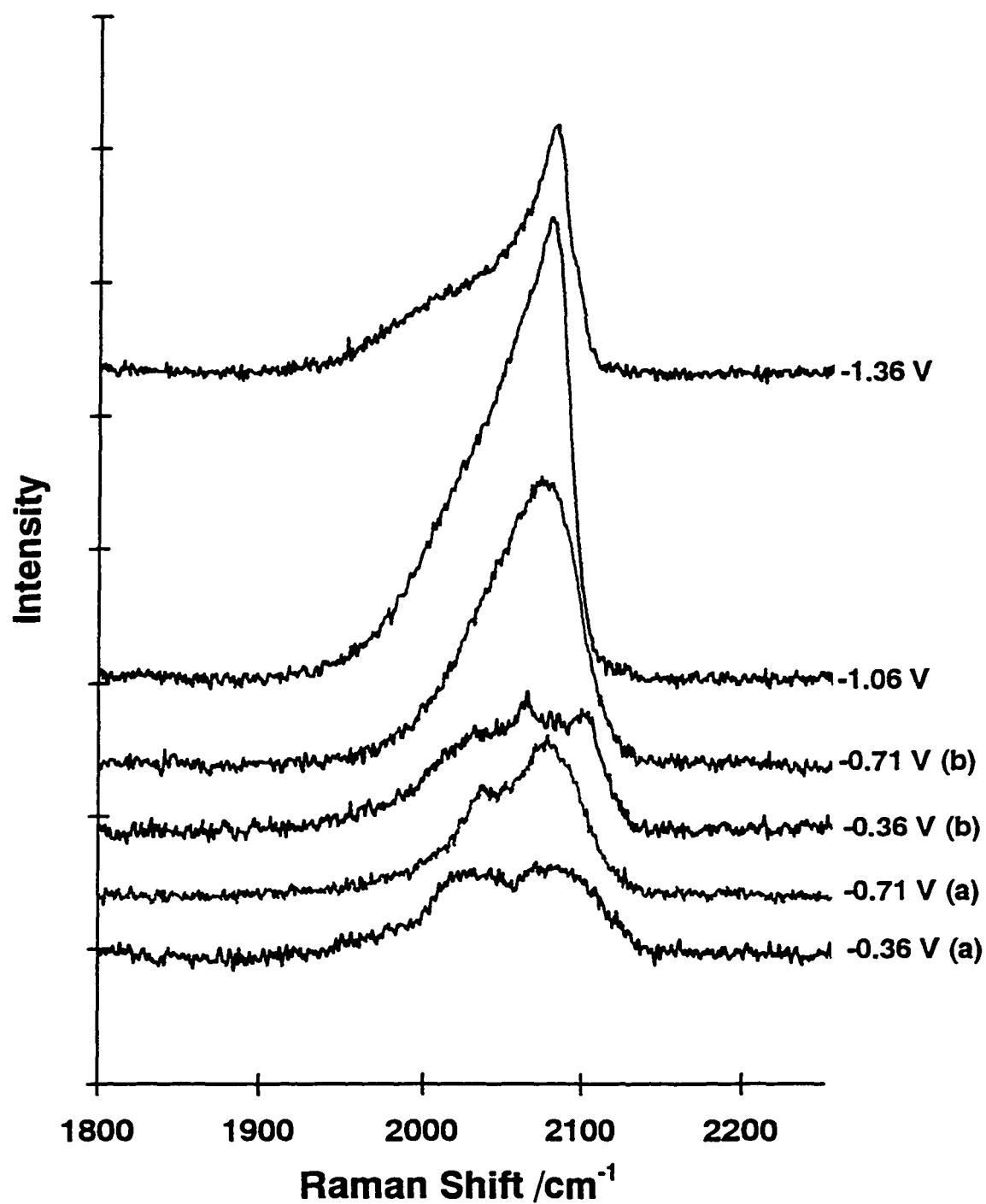


Fig. 4.13 Spectra from the Cu Electrode in CO₂-Saturated 0.1 M KHCO₃ for the CO Stretching Region



to some form of co-adsorption of CO with the chloride in the electrolyte on the copper surface.

For CO₂-saturated 0.1 M NaHCO₃ (Fig. 4.8), CO-saturated 0.1 M NaHCO₃ (Fig. 4.9) and CO₂-saturated 0.1 M KDCO₃ (Fig. 4.10), at -1.06 V, the intensity of the adsorbed CO bands decreased with reaction time. The decay of the intensity of the CO stretch was more rapid than that of the Cu-CO stretching and rotational bands. The intensity change for the time decay of the CO stretching band for the three solutions has been quantified (Fig. 4.14). Each spectrum was baseline corrected and curve fitted to determine the area under the CO stretching band (I_s). The ratio of this area was divided by the intensity of the bulk water band (I_w). All three solutions show similar time decays for the CO stretch. Since the reaction is poisoned over time, the bands from the intermediate species should decrease. Thus, the decay of the CO stretching band is consistent with CO being the intermediate in this reaction.

To confirm that the observed CO adsorbate was indeed the intermediate in the reduction of CO₂ on copper, an experiment was performed using N₂-saturated 0.1 M NaHCO₃. After preparing the surface using the previously defined pretreatment process, the potential was stopped at -1.21 V. Figure 4.15 shows a spectrum at this time (A) and after approximately 5 minutes of reaction time (B). After this second spectrum was recorded, the N₂

Fig. 4.14: Time Dependence of the Intensity of the CO Stretching Band from the Cu Electrode at -1.06 V in Gas-Saturated 0.1 M Electrolyte

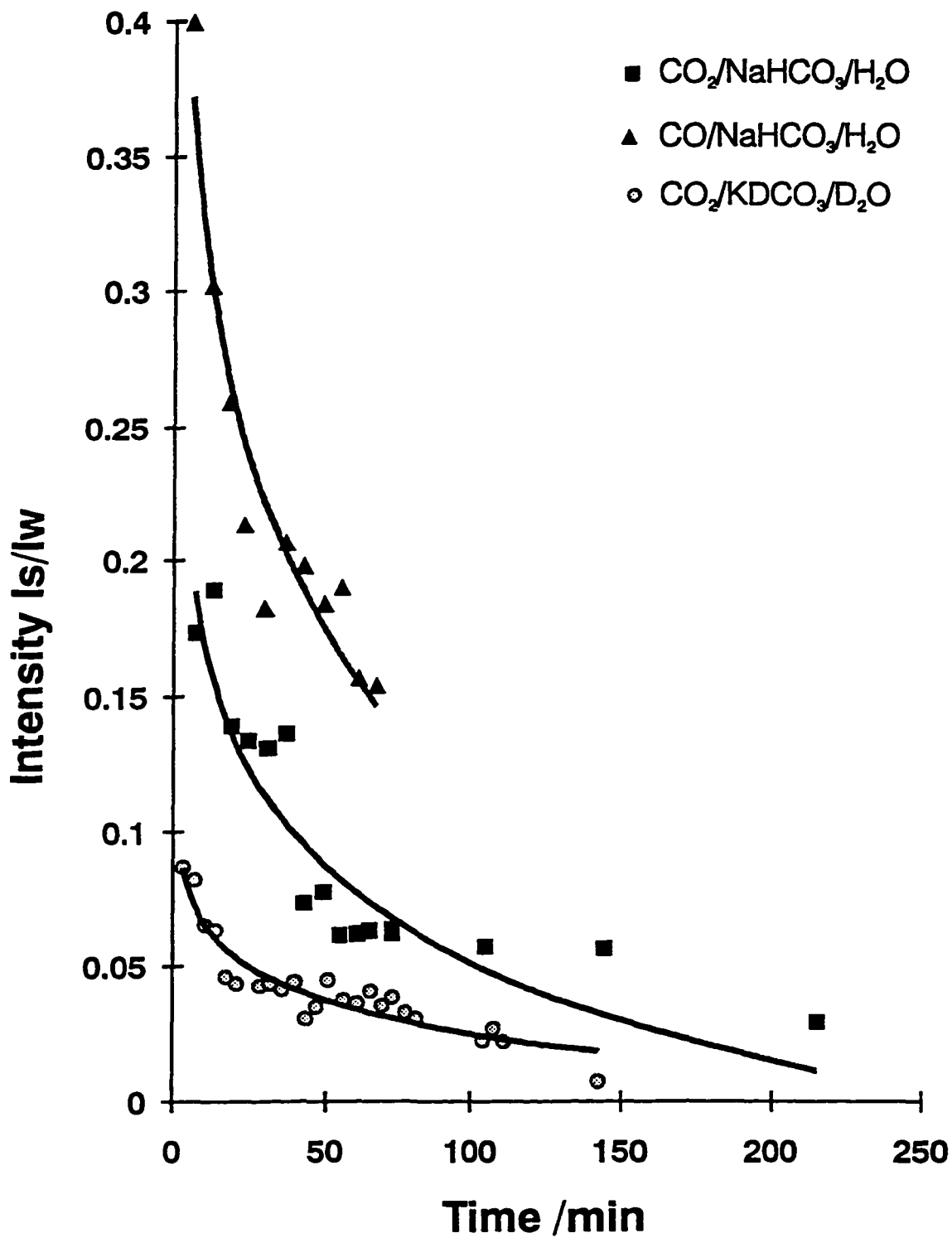
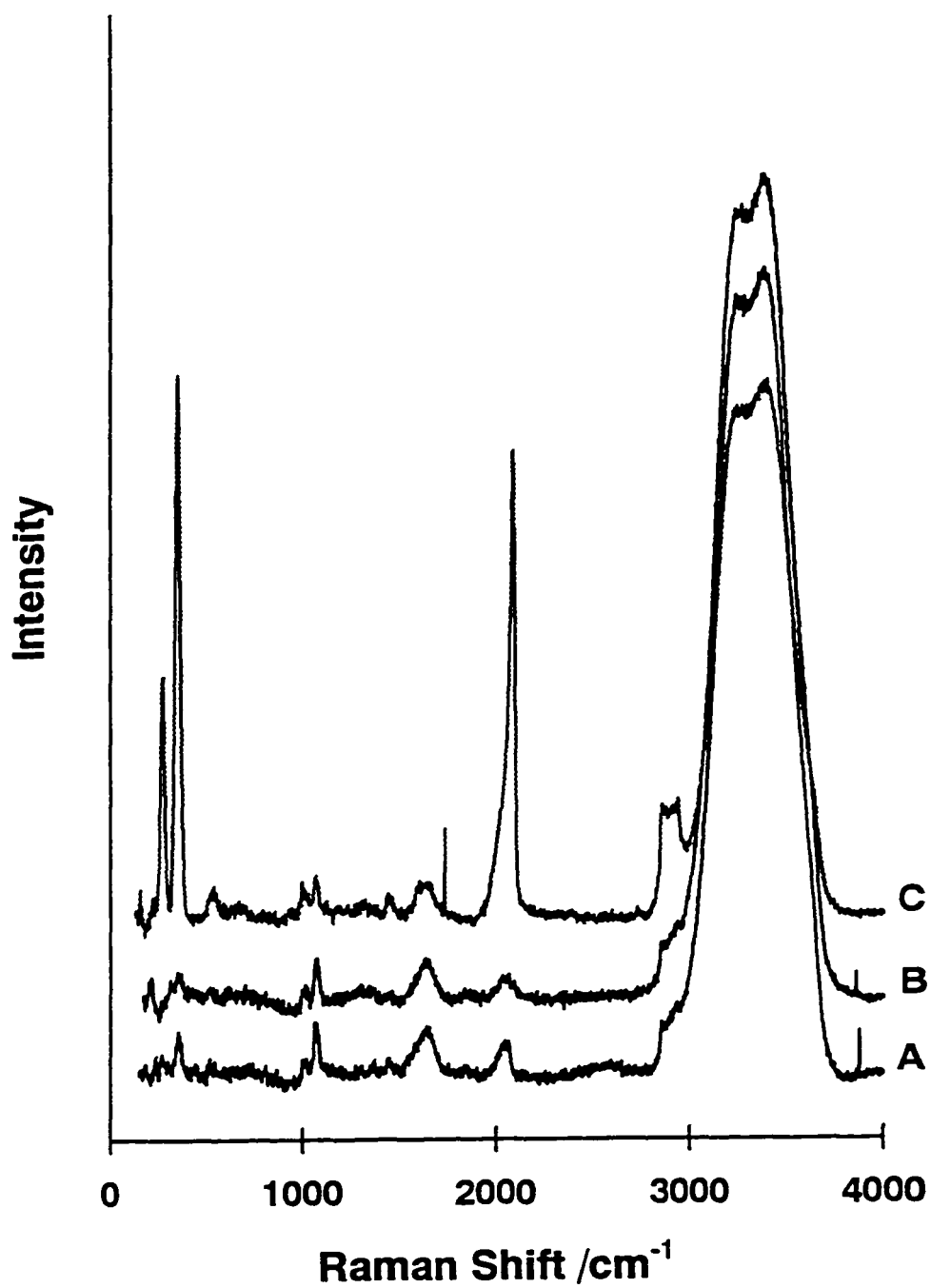


Fig. 4.15: Spectra from the Cu Electrode at -1.21 V in 0.1 M NaHCO₃
A) Initially Saturated with N₂
B) After ~5 minutes with N₂
C) After the addition of CO₂ and two 10 mV/s ORCs



gas was turned off and CO_2 was added to the system. Following two 10 mV/s ORCs, another spectrum was recorded (Fig. 4.15C).

The initial intensities of the adsorbed CO bands for the N_2 -saturated solution were quite weak, especially the relative intensity of the CO stretch. These bands decreased as the reaction continued, indicating that the SERS intensity was being lost. If CO_2 (aq) is being reduced in the reaction, there should be no SERS of CO from N_2 -saturated solution. The small bands observed are likely due to residual amounts of CO_2 , from the $\text{CO}_2 \rightleftharpoons \text{HCO}_3^-$ equilibrium, present in small amounts in HCO_3^- solution.

After the addition of CO_2 and two 10 mV/s ORCs, the SERS intensity had increased significantly. Thus, the SERS intensity of adsorbed CO must be associated with the presence of CO_2 . This agrees with the observations of Kim et. al [107] who demonstrated that it is not possible to reduce the bicarbonate ion directly. Since the increased SERS intensity of the adsorbed CO bands occurs only when CO_2 is added, CO must be produced from the CO_2 (aq). Therefore, the observed CO adsorbate must be the intermediate in the reduction of CO_2 .

4.2.2 CH_x Species

For CO₂-saturated 0.1 M NaHCO₃ (Fig. 4.6) and KHCO₃ (Fig. 4.7), a broad "flat" band is observed at ~2900 cm⁻¹. In both solutions, it was observed initially at -0.36 V (a) and disappeared at 0.64 V (b). It reappeared at -0.36 V (b) and disappeared at -1.76 V. For both the CO₂-saturated (Fig. 4.8) and CO-saturated (Fig. 4.9) 0.1 M NaHCO₃ the time dependence studies showed that this band decreased only slightly with time. Bands related to a symmetric or asymmetric CH stretch of adsorbed methyls are expected in the 2750 - 2950 and 2810 - 3050 cm⁻¹ region [11].

No other reports of this band on copper electrode surfaces were found in the literature. However, bands similar in position and shape were reported from SERS studies of silver [111,112]. These bands were thought to arise from the decomposition of CO₂ on the silver surface [20]. Mahoney et al. [111] assigned this to a CH_x species. Inchinohe et al. [112] assigned it as two separate components, a CH stretch, and an O-C-O overtone and a CH stretch of a formate species[112]. In this work, it is being attributed to a CH_x species.

A weak band which may also be associated with a CH_x species was observed at ca. 1440 cm⁻¹ from CO₂-saturated 0.1 M NaHCO₃ at -1.06 V. From CO₂-saturated 0.1 M KHCO₃, it was observed at ca. 1434 - 1443 cm⁻¹ at 0.14,

-0.71 (b), -1.06 and -1.36 V. This band was only observed when the $\sim 2900\text{ cm}^{-1}$ band was present. Bands related to the deformation of adsorbed methyls are expected in this $1300 - 1475\text{ cm}^{-1}$ range [11]. Thus, this band is also assigned to a CH_x species.

The CH_x bands were observed from CO_2 -saturated 0.1 M KDCO_3 (Fig. 4.7) at -1.06 V . The intensity of these bands appeared to increase slightly over time. Bands associated with hydrogen were not expected from the CO_2 -saturated 0.1 M KDCO_3 solution. Two possible explanations for this are contamination of the electrode surface or impurities in the KDCO_3 solution. The contamination of the electrode surface in a manner similar to silver is unlikely as no literature about this contamination on copper has been found.

Another possible explanation is that the hydrogenation of graphitic carbon species occurs more readily than the deuteration. The reduction of H^+ occurs preferentially to D^+ and has been used to enrich the D_2O concentration in H_2O [118]. Likewise, it may be that CH is produced in preference to CD . Although D_2O is 99.9% pure, the H_2O concentration is ca. 10^{-2} M . Excellent SERS were obtained from CO_2 and CO , which at 1 atm . have solution concentrations of ca. $3 \times 10^{-3}\text{ M}$ and $1 \times 10^{-3}\text{ M}$. Thus, if CH bonds are more readily created than CD bonds, the concentration of H_2O in D_2O may be sufficient to produce protonated species on the SERS active sites.

To further explore the CO₂-saturated 0.1 M KDCO₃ system, spectra were collected after the reaction had been occurring for a long time. Figure 4.16A shows a spectrum collected at -1.26 V immediately after the time dependence study had been completed. After collecting this spectrum, the system was explored by stepping to various potentials including numerous positive ones up to 1.24 V. Figure 4.16B shows a spectrum collected at -1.26 V after these experiments were completed. The SERS surface had been reactivated as demonstrated by the observation of the intense CO stretching band.

In Figure 4.16B, a band which was not seen in any previous spectra appeared at ca. 2160 cm⁻¹. This is in the region where a CD symmetric stretch is expected [11]. Thus, it appears that CD_x was eventually produced during this reaction. This shows that it may indeed be possible that the CH bands are due to trace amounts of H₂O in the D₂O solution.

4.2.3.1 CH/Graphitic Carbon Interchange

Bands attributable to graphite are expected in the region between ca. 1300 and 1600 cm⁻¹ [119]. Unfortunately, this overlaps the area where the weak ν_3 band of CO₃²⁻ is expected [35,77]. This makes it difficult to distinguish graphitic carbon from carbonate species based on band position. Thus, it is necessary to see how the bands change in relationship to other bands.

Fig. 4.16: Spectra from the Cu Electrode at -1.26 V in CO₂-Saturated 0.1 M KDCO₃
A) After Time Dependence Experiments
B) After Potential Step Experiments

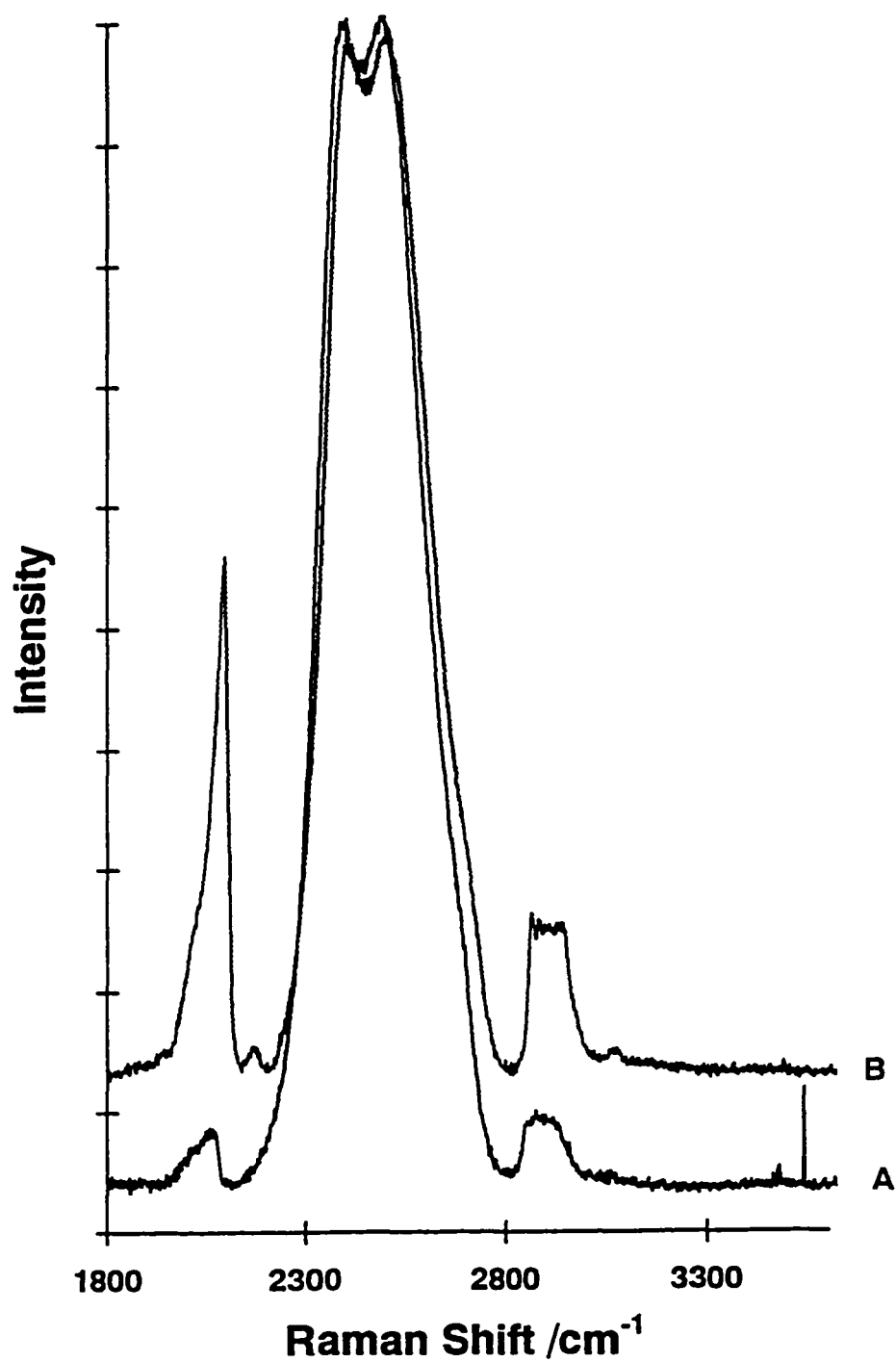
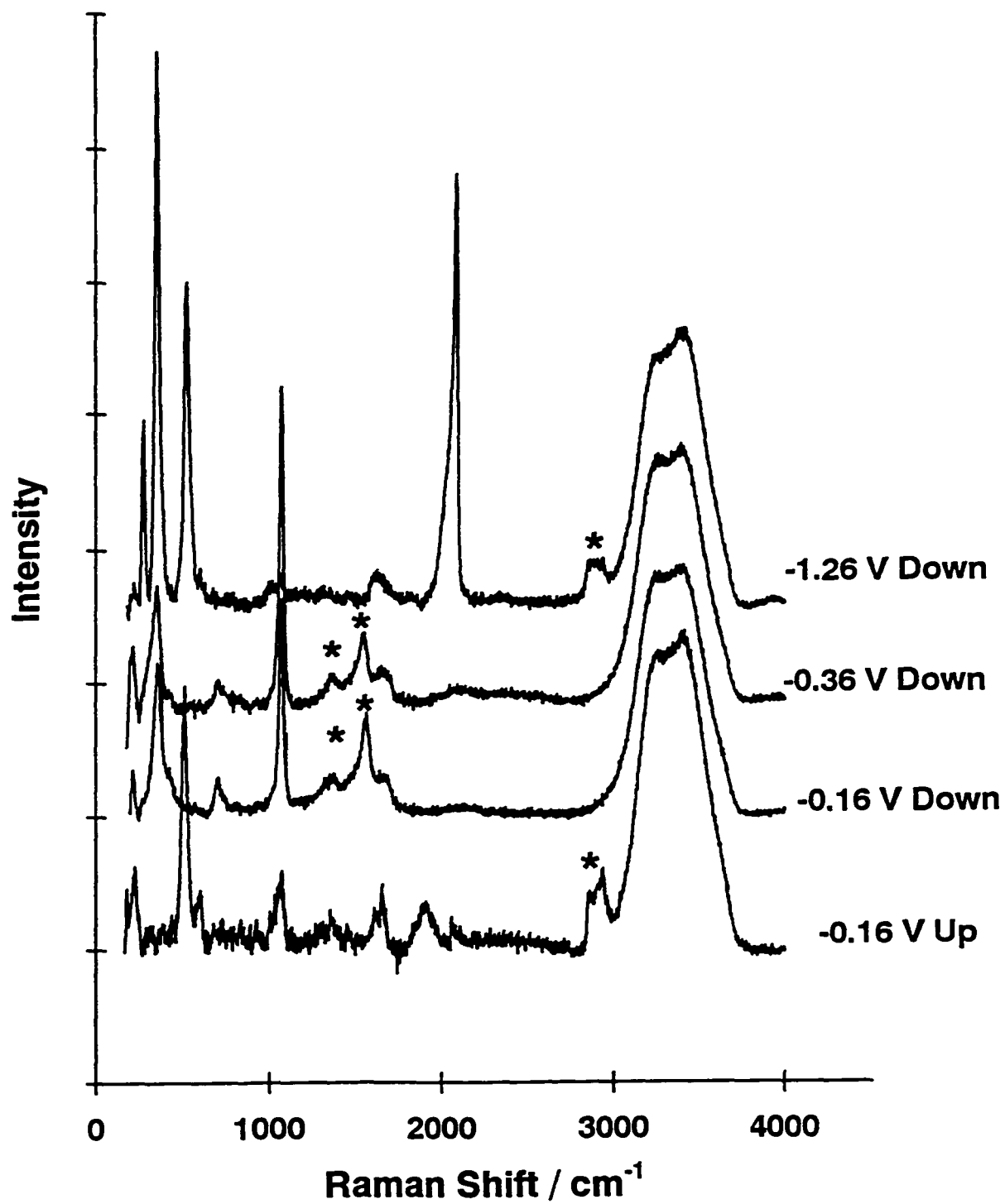


Figure 4.17 shows a comparison between the SERS spectrum obtained for CO₂-saturated 0.1 M NaHCO₃ at -0.16 V (before Fig. 4.5 (A1)) on the upward and the downward potential step. These spectra were recorded sequentially with those presented in Figure 4.11. The CH_x bands were observed at -0.16 V, before the potential was stepped into the anodic region of the voltammogram. On the downward step, -0.16 and -0.36 V, these CH_x bands disappeared. At these potentials bands at ca. 1360 and 1580 cm⁻¹ appeared. At -1.26 V, these bands disappeared and the CH_x bands were again observed.

CH_x appears to be a product formed from carbon. If there is a CH_x ⇌ C_{graphite} interchange, graphitic carbon is hydrogenated at negative potentials and not likely the poisoning species. As well, the observed CH_x bands do not show a time dependent increase in intensity for CO-saturated or CO₂-saturated 0.1 M NaHCO₃. Thus, they are unlikely to be related to the poisoning species band which increases in intensity over time. Therefore, it appears that neither CH_x nor graphitic carbon contribute to the poisoning of the system.

In addition, if graphitic carbon was the poisoning species, it would be expected that during the continuous electrolysis of CO₂ the CO signal would decrease, disappear, and be replaced by a carbon signal. This was not

Fig. 4.17: Spectra Comparing CH_2 and Possible Graphite Bands from the Cu Electrode in CO_2 -Saturated 0.1 M NaHCO_3 (* highlights bands of interest)



observed. Thus it appears that the deactivation of the copper surface during CO₂ reduction is not associated with the formation of carbon (graphite) islands.

DeWulf et al. [102] attributed this poisoning species to graphitic carbon based on ex-situ results. However, our experiments demonstrate that bands attributed to graphitic carbon were not found in the potential regions where adsorbed CO was observed. Thus, it may be that the graphitic carbon found in the experiments by DeWulf et al. [102] was created after, rather than during, the reaction.

4.2.4 Carbonate/Bicarbonate

A large number of bands attributable to carbonate and bicarbonate vibrational modes were observed from both CO₂-saturated 0.1 M NaHCO₃, Fig. 4.18, and KHCO₃, Fig 4.19, at different potentials. The results from the time dependence study (Figs. 4.8-4.10) show that the band intensities from these species do not appear to decrease over time. Thus, the bands are likely due to carbonate/bicarbonate in the interfacial region, which may not be participating in the reduction of CO₂. The vibrational modes are labelled based on the assignments (i.e., ν_1 , ν_2 , etc.) for the free CO₃²⁻ ion (Fig. 1.11), even though carbonate may exist in a complex, including cations. This labelling

Fig. 4.18: Spectra from the Cu Electrode in CO₂-Saturated 0.1 M NaHCO₃ for the Carbonate/Bicarbonate Region

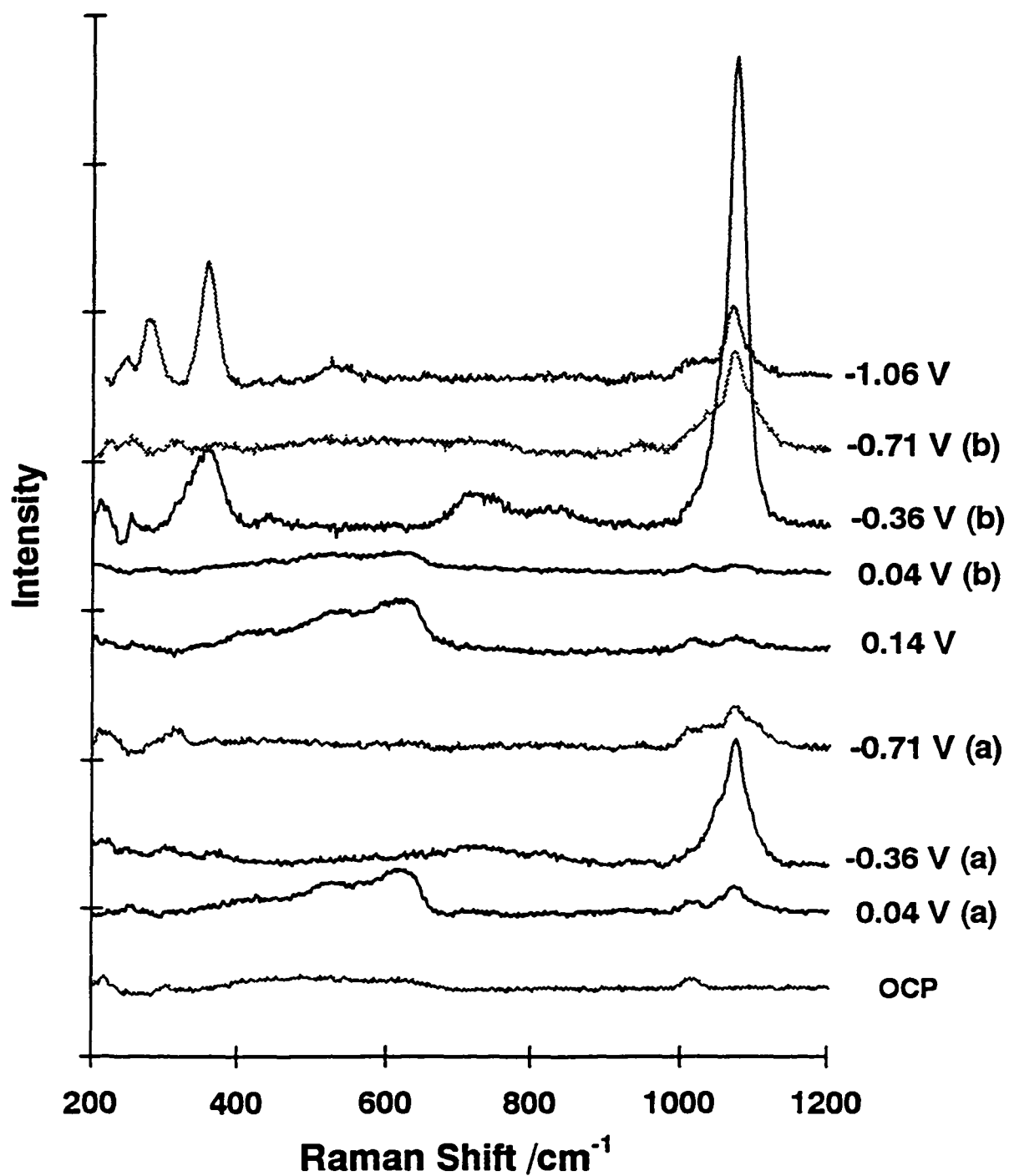
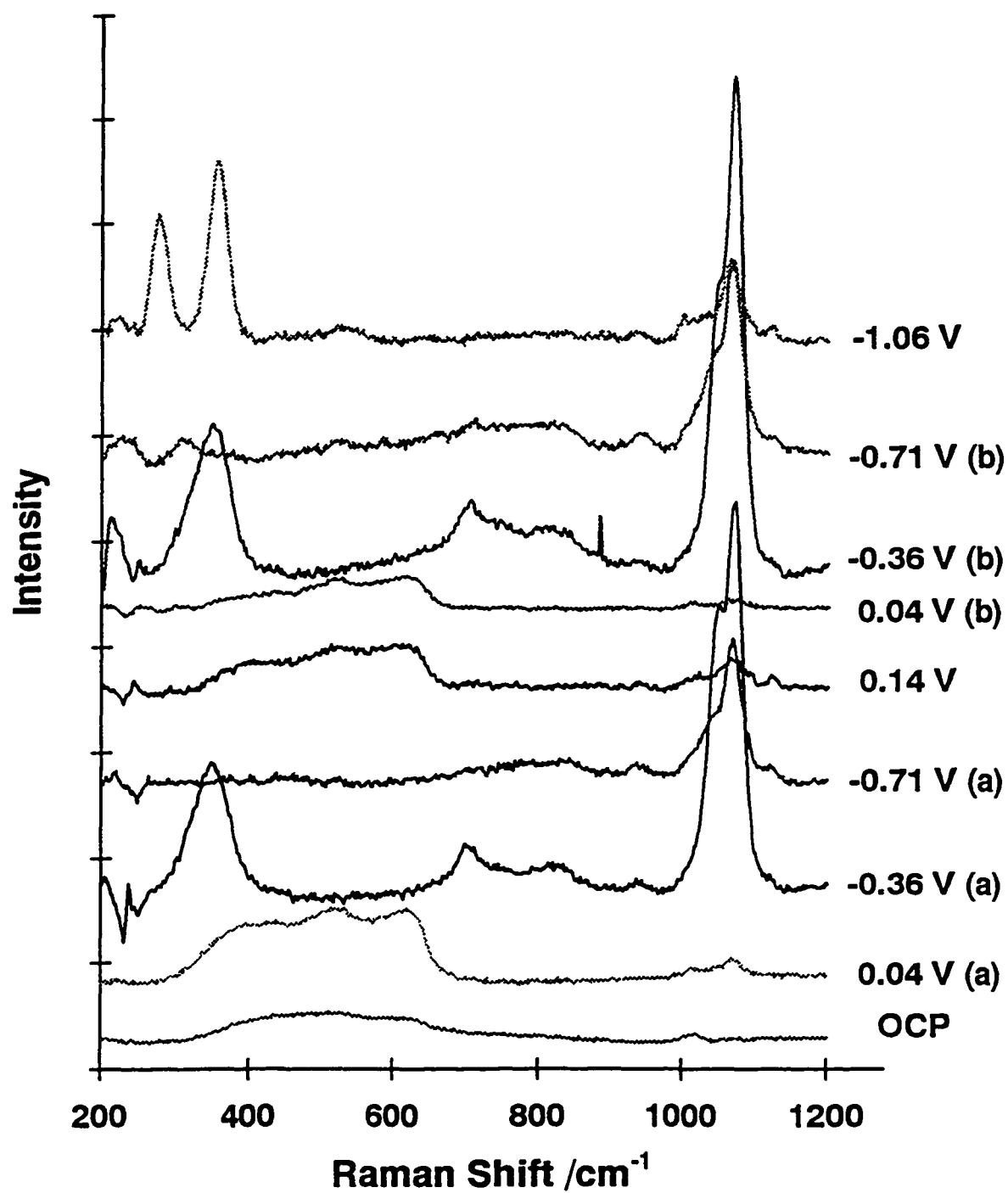


Fig. 4.19: Spectra from the Cu Electrode in CO₂-Saturated 0.1 M KHCO₃ for the Carbonate/Bicarbonate Region



is consistent with the labelling of vibrational modes found in the literature [35,74,75,77].

The $\text{Na}[\text{CuCO}_3)_2] \cdot 3\text{H}_2\text{O}$ structure was shown by Wells [72]. The Cu atom has distorted (4+1+1) coordination. The four short bonds (1.92 Å) are to the oxygens of two monodentate and one bidentate carbonates. There is a longer bond (2.36 Å) to the oxygen of the water. This gives a distorted square pyramidal geometry for the copper. There is also a very long bond (2.60 Å) from the copper to one of the monodentate carbonates (i.e., one of the monodentate carbonates can also be thought of as a highly asymmetrical bidentate carbonate).

Taravel et al. [77] was the only reference found in the literature who reported Raman and IR bands of $\text{Na}[\text{CuCO}_3)_2] \cdot 3\text{H}_2\text{O}$ and the $[\text{Cu}(\text{CO}_3)_2]^{2-}$ ion. They provided band assignments, but did not present their spectra. Thus, it was not possible to compare their band shapes with this work. Their results are presented in Table 3.2. An attempt was made in the present study to observe the $[\text{Cu}(\text{CO}_3)_2]^{2-}$ ion, but no spectra could be obtained as the red exciting line was completely absorbed by the blue solution.

From CO_2 -saturated 0.1 M NaHCO_3 a band at ca. 356 cm^{-1} was observed at -0.36 V (Fig. 4.18 b). From CO_2 -saturated 0.1 M KHCO_3 this band was

observed at ca. 347 and 348 cm^{-1} at -0.36 V (Fig. 4.19 a and b, respectively). This band is being attributed to a Cu-OCO₂ mode, based on the assignment by Taravel et al. [77] of the Raman band at 310 cm^{-1} and the IR bands at 320 and 350 cm^{-1} . This band overlaps the region where Cu-CO stretching was observed. However, the Cu-OCO₂ band is broader than the Cu-CO stretching band. As well, the intensity of the associated CO stretching mode increased from -0.36 to -1.06 V, while the Cu-OCO₂ band was only seen at -0.36 V. No band was observed in this region at -0.71 V. The Cu-CO stretch was not observed until -1.06 V. The fact that the Cu-OCO₂ stretch does not appear to be associated with the other modes of adsorbed CO further supports its assignment.

From CO₂-saturated 0.1 M NaHCO₃ a band at ca. 720 cm^{-1} was observed at -0.36 V (Fig. 4.18 a and b). From CO₂-saturated 0.1 M KHCO₃ this band was observed at ca. 702 and 705 cm^{-1} at -0.36 V (Fig. 4.19 a and b). This band is being assigned to a $\nu_4(\text{CO}_3^{2-})$ mode of a copper carbonate species, based on the assignment by Taravel et al. [77] of a Raman band at 755 cm^{-1} for the $[\text{Cu}(\text{CO}_3)_2]^{2-}$ ion in solution.

For both solutions a weak band, ca. 813 to 829 cm^{-1} , appeared almost as a shoulder to the $\nu_4(\text{CO}_3^{2-})$ band. Taravel et al. [77] did not observe this band for the $[\text{Cu}(\text{CO}_3)_2]^{2-}$ ion in solution. However, an IR band at 855 cm^{-1} from the crystal was observed and assigned to a $\nu_2(\text{CO}_3^{2-})$ mode. For the free CO₃²⁻ (D_{3h}),

this mode should not be Raman active. The observation of a $\nu_2(\text{CO}_3^{2-})$ band, at 880 cm^{-1} , in the Raman spectra of $8\text{ M K}_2\text{CO}_3$, was attributed by Davis and Oliver to a distortion of the D_{3h} symmetry of the ion, combined with cation interactions [35]. For nitrate complexes (also of D_{3h} symmetry), the ν_2 mode for complexes occurs 28 cm^{-1} lower than the ν_2 mode of the free anion [120]. Thus, this band is assigned to a $\nu_2(\text{CO}_3^{2-})$ mode of a copper carbonate species.

From CO_2 -saturated 0.1 M NaHCO_3 and KHCO_3 a band at ca. 1064 to 1074 cm^{-1} was observed at all potential steps less than 0.64 V . Taravel et al. [77] did not observe this band as NO_3^- and free CO_3^{2-} bands from their solution obscured this portion of the spectra. However, a Raman band at 1071 cm^{-1} was observed for the salt and assigned to a $\nu_1(\text{CO}_3^{2-})$ mode. Thus, this band is being assigned as a $\nu_1(\text{CO}_3^{2-})$ mode of the copper carbonate complex ion.

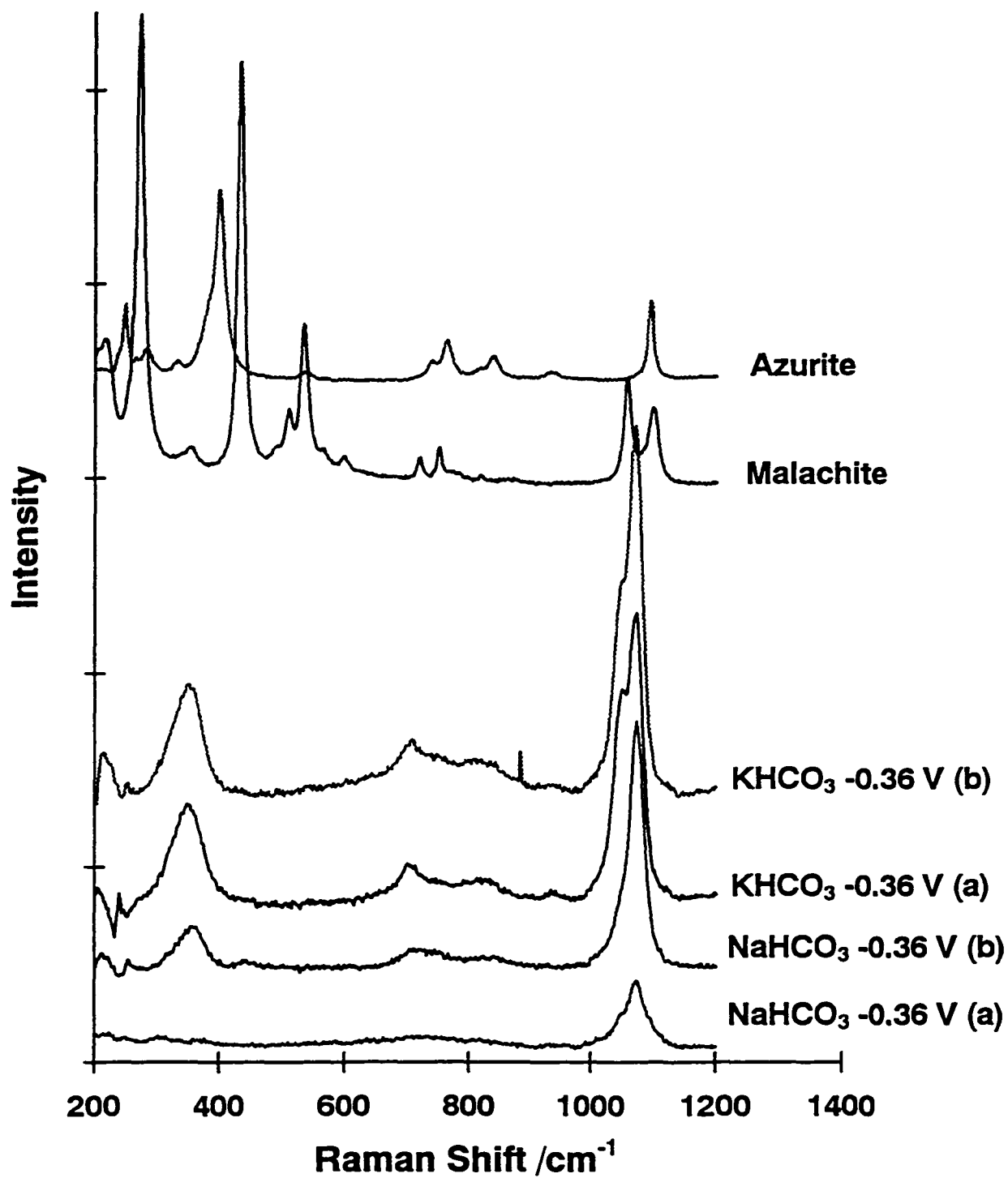
From both solutions a weak band at ca. 1010 to 1020 cm^{-1} appeared at all potentials. At potential steps less than 0.04 V , it appeared as a shoulder on the larger $\nu_1(\text{CO}_3^{2-})$ band. Davis and Oliver [35] observed a Raman band at 1017 cm^{-1} for 3.5 M KHCO_3 . They assigned this band to a $\nu_5(\text{C-OH})$ stretch of the HCO_3^- ion. For reference, 2 M KHCO_3 , 0.1 M NaHCO_3 and $2\text{ M K}_2\text{CO}_3$ were measured and bands were observed at ca. 1017 and 1018 cm^{-1} . Thus this band is being assigned to the $\nu_5(\text{C-OH})$ stretch of the HCO_3^- ion of the electrolyte. A third shoulder on this larger band is seen ca. 1044 to 1050 cm^{-1}

at potentials of -0.36 and -0.71 V. It appears to be associated with the $\nu_1(\text{CO}_3^{2-})$ band which is a non-degenerate mode. Thus if this third shoulder is related to the $\nu_1(\text{CO}_3^{2-})$, there must be two distinct species one for each band observed. Taravel et al. [77], observed one Raman and two IR bands, including one at 1055 cm^{-1} , which was assigned to $\nu_1(\text{CO}_3^{2-})$ modes of the $[\text{Cu}(\text{CO}_3)_2]^{2-}$ ion. Thus this band is assigned to a $\nu_1(\text{CO}_3^{2-})$ mode.

The most intense bands from carbonate modes were seen at -0.36 V. The C3 feature occurs on the voltammogram at -0.36 V. Thus, the C3 feature is related to production of carbonate species through the decomposition of the surface film. According to the Pourbaix diagram (Fig. 3.2), the stable species expected to be formed at the initial step to 0.64 V would be a copper carbonate species such as malachite or azurite.

Reference spectra of malachite and azurite samples were recorded (Fig. 3.1). Figure 4.20 compares these spectra to those obtained at -0.36 V from Figs. 4.18 and 4.19. The -0.36 V spectra do not resemble those from the reference samples. It appears that the observed copper carbonate species is not simply composed of these minerals. It is probably a complex copper carbonate hydroxide mixture.

Fig. 4.20: Spectra from Azurite and Malachite Compared to the Cu Electrode at -0.36 V in CO₂-Saturated 0.1 M NaHCO₃ and KHCO₃



4.2.5 Copper Oxides

From both CO₂-saturated 0.1 M NaHCO₃ (Fig. 4.21) and KHCO₃ (Fig. 4.22), a broad envelope containing several weak bands was observed between ca. 320 and 680 cm⁻¹. These bands were observed at OCP and disappeared at -0.36 V ((a), cf. p. 123-124). They reappeared at 0.14 V and disappeared again at -0.36 V (b). This is shown in Fig. 4.21 for CO₂-saturated 0.1 M NaHCO₃, and Fig. 4.22 for CO₂-saturated 0.1 M KHCO₃. For CO₂-saturated 0.1 M NaHCO₃ at 0.04 (a) and 0.14 V, this band appeared as three peaks ca. 398 to 408, 520 to 527, and 615 cm⁻¹. For CO₂-saturated 0.1 M KHCO₃ at 0.04 V (a and b) and 0.14 V, peaks were observed at ca. 390 to 398, 518 to 520, and 615 cm⁻¹.

At 0.04 (a) and 0.14 V the intensity of this band envelope was greatest. The voltammogram (Fig. 4.6) showed a feature, C1, at around 0.1 V. Perez-Sanchez [80] observed a voltammetric feature in bicarbonate media, at around 0.1 V. They assigned this feature to the reduction of a CuO/Cu(OH)₂ layer to a Cu₂O layer.

Cu₂O should have only one Raman active vibrational mode (F_{2g}) [49]. However, more than one vibrational mode has been reported for crystals and crushed powders [49,51,60,61,71]. This has been attributed to the breakdown of the selection rules due to imperfections in the crystal lattice [62]. As

Fig. 4.21: Spectra from the Cu Electrode in CO₂-Saturated 0.1 M NaHCO₃ for the Oxide Region

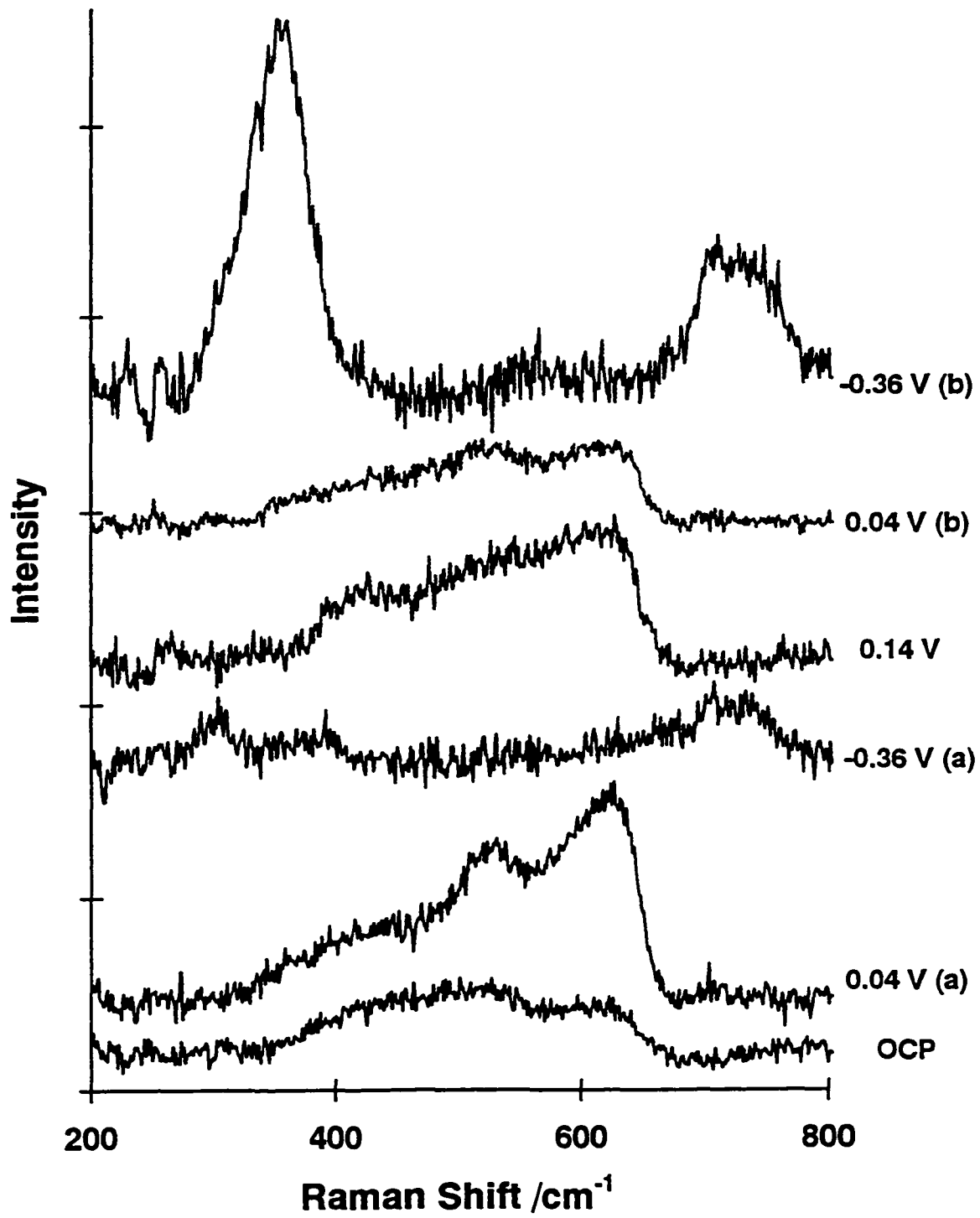


Fig. 4.22: Spectra from the Cu Electrode in CO₂-Saturated 0.1 M KHCO₃ for the Oxide Region

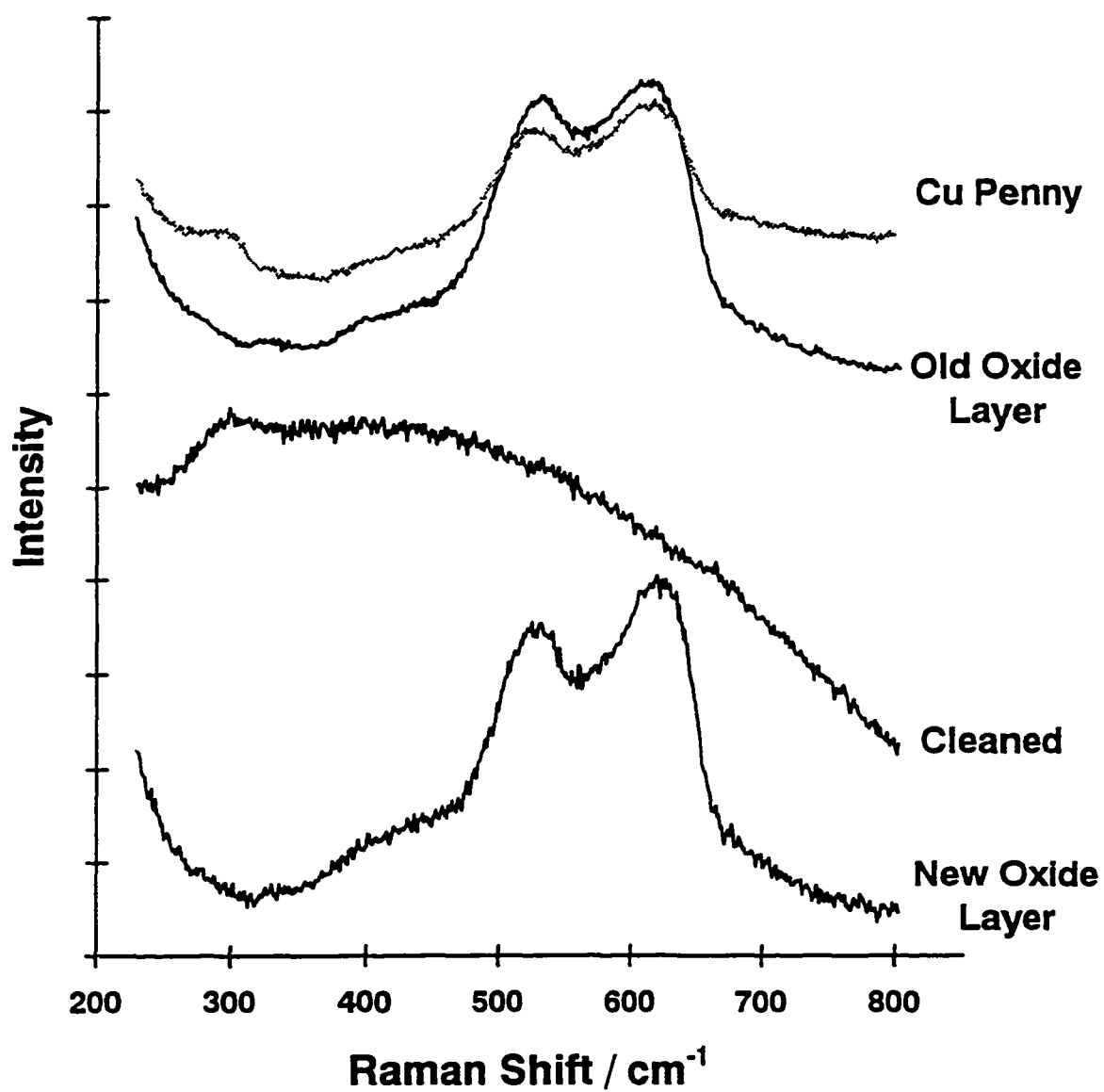


previously presented in Table 3.1, authors have reported observing between two and seven Raman bands for Cu_2O in the 350 to 690 cm^{-1} range. Based on the similarity between the observed band envelope and the bands reported for Cu_2O , this band envelope is attributed to a copper oxide.

To further confirm this assignment, several reference samples were run. A spectrum of a copper electrode which had been exposed to the atmosphere for several years was recorded. After washing the electrode with 10% HCl to remove the surface film another spectrum was accumulated. The electrode was then left exposed to the air for several days and another spectrum was recorded. Reference spectra from Cu powder, foils, and coins were also obtained. Figure 4.23 shows the spectra from the old copper electrode, before cleaning, after cleaning, and after re-exposure to air, and a copper penny. These reference spectra show bands similar in shape and position to the bands shown in Fig. 4.21 and 4.22 attributed to copper oxide, further supporting its assignment.

The spectrum of exposed copper resembles the SERS spectra of Cu_2O as presented by Carron et al. [67]. As well, Persson and Leygraf [66] reported that the surface film formed on copper in clean moist air is Cu_2O . Thus, the oxide bands are probably attributable to Cu_2O .

Fig. 4.23: Reference Spectra Measured in Air from a Cu Electrode Before and After Cleaning and a Penny



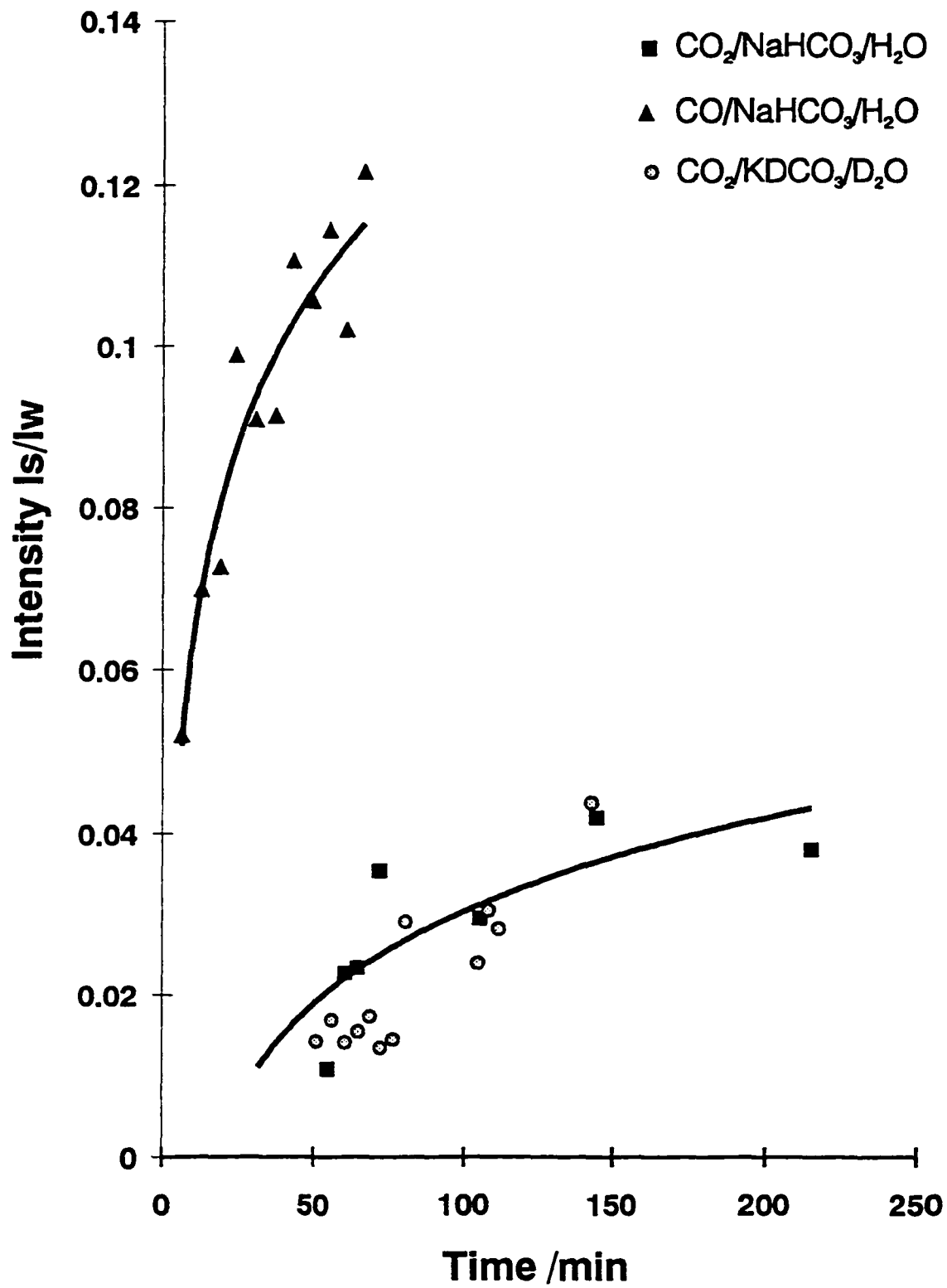
4.2.6 Poisoning Species

In the time dependent study of spectra from CO₂-saturated (Fig. 4.8) and CO-saturated (Fig. 4.9) 0.1 M NaHCO₃ at -1.06 V, a band attributed to the poisoning species was observed at 523 and 527 cm⁻¹. From CO₂-saturated 0.1 M KDCO₃ (Fig. 4.10) at -1.06 V, this band appeared as two peaks at 450 and 513 cm⁻¹. In all cases, the intensity of this band increased over time. The time dependent intensity increase has been quantified by the method used for the CO stretch (Section 4.2.1). The result is shown in Figure 4.24.

The intensity of the bands attributed to adsorbed CO (Fig. 4.14) decayed over time whereas the intensity of the poisoning band increases. This indicates that the poisoning species is related to the electrochemical processes occurring on the copper surface. The loss of SERS intensity of adsorbed CO was related to the poisoning of the reaction, not the loss of SERS active sites.

In the potential dependence study of CO₂-saturated 0.1 M NaHCO₃ (Fig. 4.6) and KHCO₃ (Fig. 4.7), a band was observed at ca. 525 to 528 cm⁻¹. It was first observed at -1.06 V and at lower potentials it was broader and more intense. The copper oxides, assigned in Section 4.2.5, although different in shape were observed in this same region at positive potentials. Hence it is

Fig. 4.24: Time Dependence of the Intensity of the Poisoning Band from the Cu Electrode at -1.06 V in Gas-Saturated 0.1 M Electrolyte



possible that the poisoning species is related to a Cu_2O or another Cu-O species.

In addition to Cu-O and Cu-OH bands, summarized in Table 3.1, metal-carbon (i.e., Cu-C) vibrational modes are expected in the region below 700 cm^{-1} [1]. Cu-O and Cu-OH bands also occur below 700 cm^{-1} in Malachite and Azurite (Table 3.2). In order to identify the poisoning species, the presence of Cu-O, Cu-OH, and Cu-C modes must be explored.

Since only the poisoning band increased with time, the Cu-C vibrational mode would have to be due to a copper carbide. The poisoning species was seen at a wide variety of potentials (Fig. 4.11). After stepping to potentials as high as 1.0 V and back to -1.06 V, the poisoning species was still present. This would indicate that the poisoning species is stable, even at positive potentials. As noted in Chapter 3, copper carbide is not stable. Thus, it is unlikely that copper carbide is the poisoning species.

As discussed in Chapter 3, a number of bands attributable to adsorbed oxygens have been observed using HREELS in UHV on Cu(110) [91,92]. For three different coverages, bands attributable to adsorbed oxygens were observed at 403 cm^{-1} , 330 and 500 cm^{-1} , and 153 and 653 cm^{-1} . In accordance with the IR data, Mundenar et al. [91] assigned the bands at 153 and 653 cm^{-1}

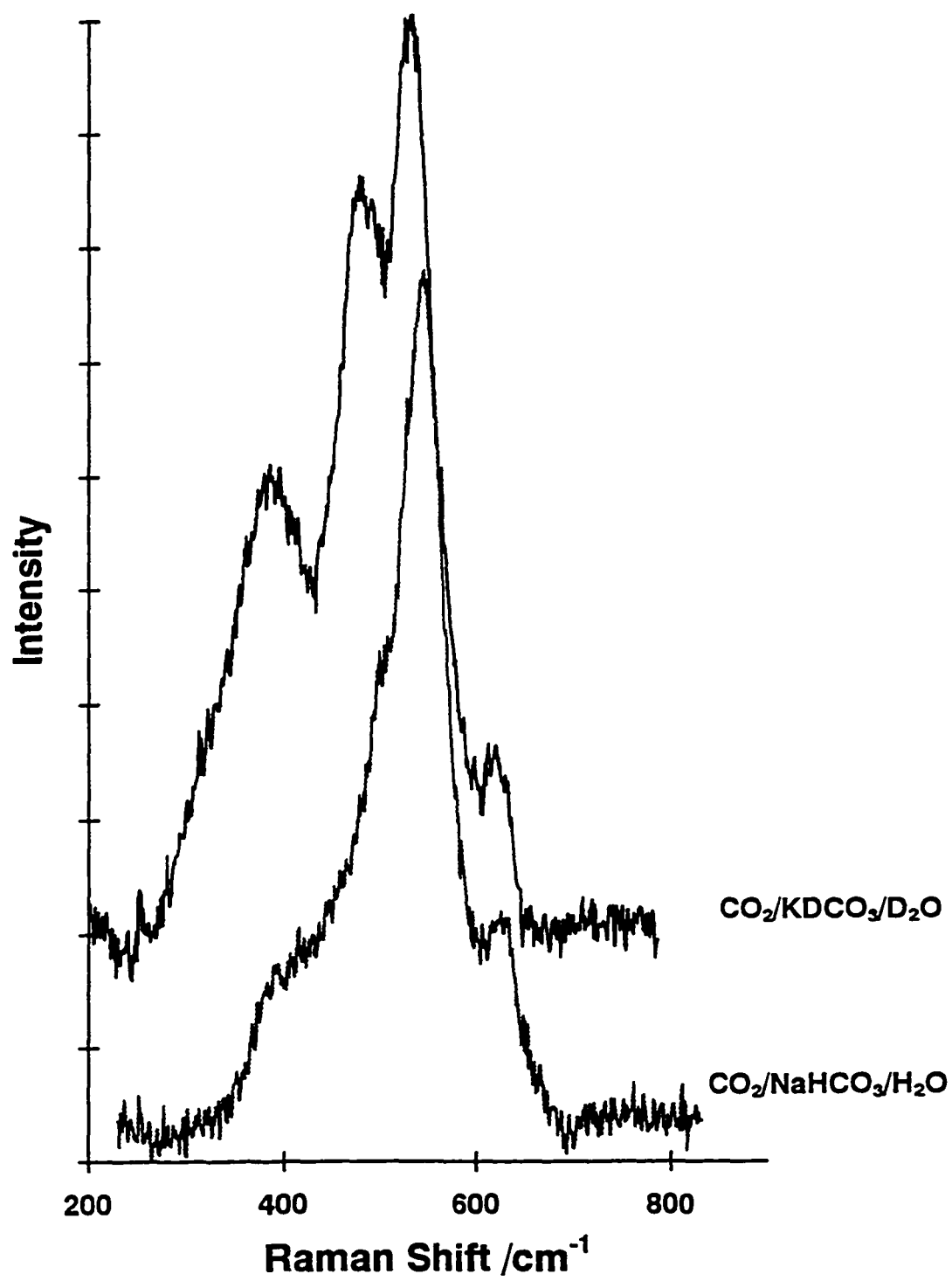
to bulk Cu_2O , and thought that the band at 500 cm^{-1} was related to some form of adsorbed oxygen present on the Cu_2O .

It has been suggested that subsurface oxygen, initially present in copper, may be responsible for the formation of hydroxide species [89]. An experiment was undertaken to look for a connection between Cu-OH modes and the poisoning species. After the time dependence study of CO_2 -saturated 0.1 M KDCO_3 , the potential was stepped to -1.76 V , where a spectrum was collected. Figure 4.25 shows a comparison between this spectrum and the poisoning band from CO_2 -saturated 0.1 M NaHCO_3 after the poisoning species had built up (-1.76 V (a) from Fig. 4.11).

In each spectrum 4 peaks can be seen. To obtain more accurate peak positions the bands were curve resolved. These peaks occur at 386, 476, 530, and 622 cm^{-1} for CO_2 -saturated 0.1 M KDCO_3 , and at 403, 496, 544, and 628 cm^{-1} for CO_2 -saturated 0.1 M NaHCO_3 .

A shift in band position on going from a Cu-OH vibration to a Cu-OD vibration is expected because of the difference in mass between OH and OD. The vibrational frequency of a molecule, $\tilde{\nu}$, is inversely proportional to the square root of the reduced mass, μ [4]. If OH and OD are treated as a single

Fig. 4.25: Spectra Comparing Poisoning Species from the Cu Electrode at -1.76 V in CO₂-Saturated 0.1 M Electrolyte



unit, i.e., $m_{\text{OH}} = 17$ and $m_{\text{OD}} = 18$, the first approximation for the ratio of the expected vibrational change is:

$$\tilde{\nu}_1/\tilde{\nu}_2 = (\mu_2/\mu_1)^{1/2}$$

Therefore,

$$(\tilde{\nu}_{\text{Cu-OH}}/\tilde{\nu}_{\text{Cu-OD}}) = (\mu_{\text{Cu-OD}}/\mu_{\text{Cu-OH}})^{1/2}$$

$$(\mu_{\text{Cu-OH}}) = 1/(1/m_1 + 1/m_2) = 1/(1/63.5 + 1/17) = 13.41$$

$$(\mu_{\text{Cu-OD}}) = 1/(1/m_1 + 1/m_2) = 1/(1/63.5 + 1/18) = 14.02$$

$$\tilde{\nu}_{\text{Cu-OH}}/\tilde{\nu}_{\text{Cu-OD}} = (14.02/13.41)^{1/2} = 1.02$$

For an OH(D) bonded to a copper surface, where the mass of the copper surface approaches infinity relative to the mass of OH(D), $1/m_1 = 0$, therefore:

$$\tilde{\nu}_{\text{Cu-OH}}/\tilde{\nu}_{\text{Cu-OD}} = (18/17)^{1/2} = 1.03$$

The isotopic ratios observed for the peaks in the poisoning band for CO₂-saturated 0.1 M NaHCO₃ and KDCO₃ were:

$$403/386 = 1.04, 496/476 = 1.04, 544/530 = 1.03, \text{ and } 628/622 = 1.01$$

The ratios between the energies of the peaks in H₂O and D₂O are close to the expected ratio for a Cu-OH mode. Thus, it is possible that the poisoning species is associated with a Cu-OH species.

Contrary to our observations, Hartinger et al. [89] in their study of 0.5 M NaOH reported a large SERS band at ca. 700 cm⁻¹, shifted upwards to 725 cm⁻¹ upon deuteration. They theorized that although the mass difference should produce a downward shift, the effect of coupling changes was greater, resulting in an upward shift. The difference between the band shift observed by Hartinger et al. [89] and this work is possibly due to differences in solution, reaction time, and the absence of the electrochemical reduction of CO₂.

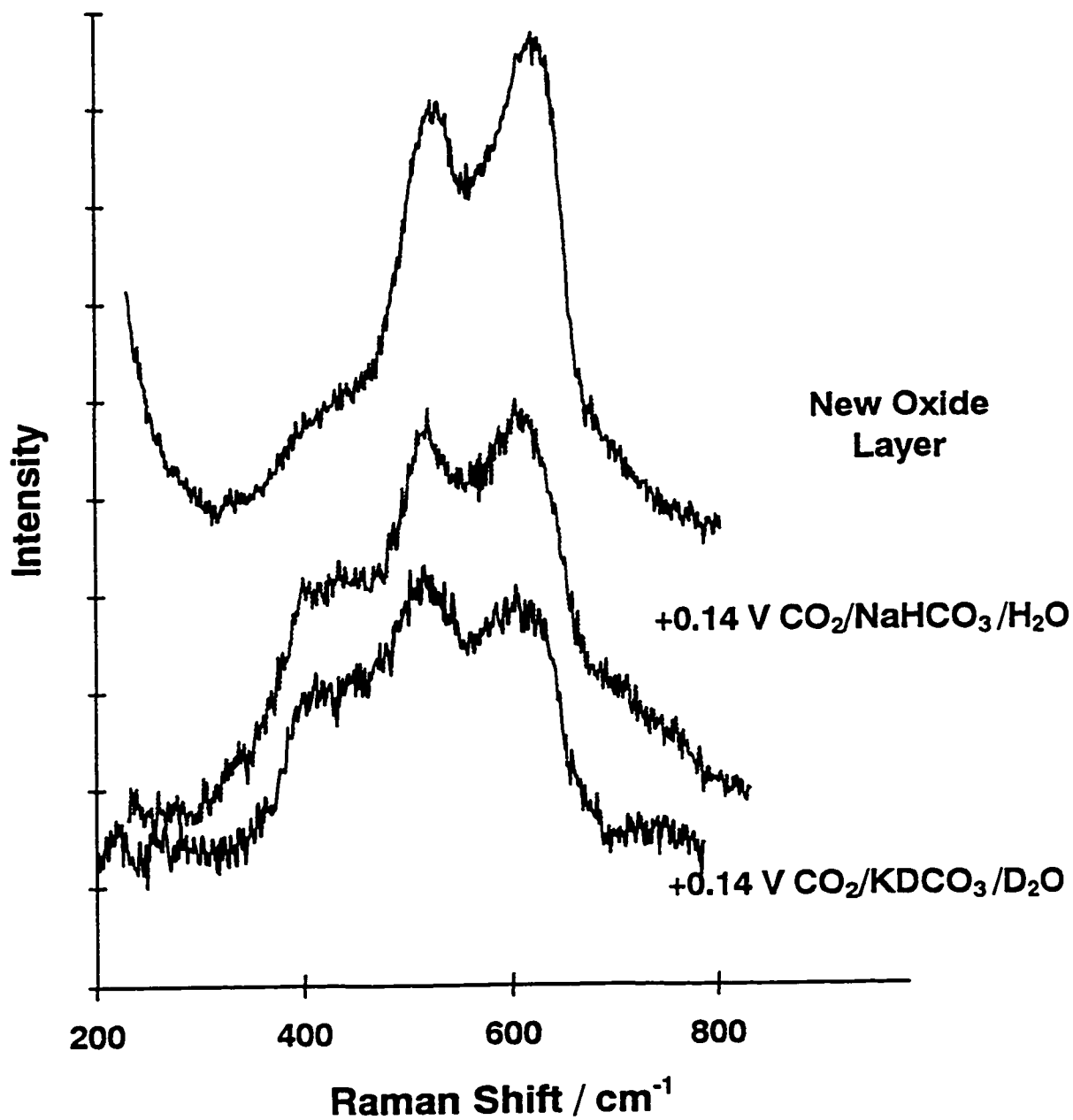
Although the isotope ratio calculation shows that Cu-OH bands could be associated with the poisoning species, it cannot confirm that they are attributable to the poisoning species. When a Cu-OH band is observed, it is expected that an OH band should also be seen. No OH band corresponding to the Cu-OH mode was observed. However, it may have been masked by the

bulk water band. This masking of the OH band by bulk water was reported by Hartinger et al. [89]. They observed a Cu-OH mode and noted that the corresponding OH band could only be observed using spectral subtraction.

Another possible assignment for the poisoning species is some form of non-crystalline Cu_2O . Both Cu oxidation and Cu^{2+} reduction can produce Cu(I) oxides, which are reported to be quite difficult to reduce [48]. A similar breakdown of selection rules may apply to the disordered copper substrate of the poisoning species on the roughened electrode surface. Between five and fifteen Raman bands have been observed for Cu_2O crushed powders and crystals (Table 3.1). However, Carron et. al. [67] only observed two SERS bands from Cu_2O on copper electrodes.

After the above experiment, where spectra were recorded at -1.76 V from CO_2 -saturated 0.1 M KDCO_3 , the potential was gradually stepped to 0.14 V and a spectrum was recorded. Figure 4.26 compares this spectrum to the spectra at 0.14 V from CO_2 -saturated 0.1 M NaHCO_3 (Fig. 4.11) and the new oxide layer on the electrode (Fig. 4.23). The similarities between the poisoning species and the oxidized copper are quite remarkable. This suggests that the poisoning band may indeed be related to a Cu_2O species.

Fig. 4.26: Spectra Comparing Poisoning Species Bands from the Cu Electrode at 0.14 V in CO₂-Saturated 0.1 M Electrolyte with Bands from Oxidized Cu



Jermann [117] found that CO₂ reduction on thermally oxidized Cu and Cu₂O deposited on Cu, yielded high Faradaic efficiencies for hydrocarbon production, as well as exceptionally high ethylene to methane ratios [117]. In this case it appears that Cu₂O is promoting the reaction rather than poisoning it. However, since there was no spectroscopic observations of the surface species, it is not possible to know what happened on the surface during the actual reaction.

Taking all the experimental data into account the poisoning species is best attributed to an oxide/hydroxide "patina" generated during CO₂ reduction. Frese [39] proposed that CO splitting accounted for the generation of OH radicals on the copper surface as a by-product of the electrochemical reduction of CO₂. This could be one explanation for the presence of oxide/hydroxide on the surface. It is also possible that during anodic activation a considerable number of Cu²⁺ ions is dissolved into the solution and redeposited as a kinetically stable hydroxide or oxide. Another explanation may be that cathodic disintegration of the electrode as an unstable Cu-H followed by solution phase oxidation, results in the deposition of the oxide/hydroxide film.

Chapter 5

Conclusions

5.0 Scope

This thesis has demonstrated that SERS spectra of intermediate species formed during the electrochemical reduction of CO₂ can be measured using the spectroelectrochemical cell designed for this work. A method for creating reproducible SERS active copper electrode surfaces was developed. By combining the information provided through voltammetry, potential step experiments, and time dependent studies, the observed spectral bands were assigned. This chapter will summarize the experimental results, provide some general conclusions about the mechanism of SERS, and suggest areas for future research.

5.1 Cell Design and Instrumentation

The spectroelectrochemical cell which was designed for use on the Dilor OMARS 89 Raman Spectrometer has been successfully utilized with the Renishaw System 1000 Raman Microscope as well. Using this cell it has been possible to obtain SERS of a copper surface in non-halide media and to study the in-situ electrochemical reduction of CO₂. It has been demonstrated that high quality SERS spectra can be collected from 180° back-scattering, even though this is not an ideal angle of incidence.

5.2 SERS Active Surfaces

The use of a series of fifteen 1 V/s and two 10mV/s ORCs was found to be effective in producing a clean, SERS active surface for studying the electrochemical reduction of CO₂. This was established as a pretreatment procedure for the copper electrode surface. The ORC process which created the SERS active surface was explored by recording spectra at the potentials where features were observed in the voltammogram. The SERS active surface was found to have been formed by the decomposition of an oxide/hydroxide/carbonate layer on the copper electrode surface. As well, the creation of the SERS sites allowed intermediates in the electrochemical reduction of CO₂ to be observed.

5.3 Band Assignment

The results from voltammetry, potential step, and time dependence studies were combined to aid in the identification of band assignments. Voltammetry provided clues into where changes in these bands could be expected, based on the potential. It was determined that the most valuable area of study for the reduction of CO₂ was in the potential region around -1.06 V. This was the potential where the time dependence experiments were performed. Using the results of these studies and a comparison with the literature presented in Chapter 3, band assignment were made.

Adsorbed CO was shown to be an intermediate in the reduction of CO₂ and band assignments were made for the CO stretch, the Cu-CO stretch and Cu-CO frustrated rotation. The fact that the intensity of all these bands decreased with time while the poisoning bands increased, showed that SERS active sites were not being lost. As well, it demonstrated that the changes in band intensity were related to the electrochemical reduction process. Thus it appears that the SERS active sites are catalytically active for the reduction of CO₂ (Gu et al. [28] suggested that SERS active sites on Ag are catalytically active).

Band assignments for a CH_x species were made. The observation of CH_x species in deuterated solution was proposed to result from the trace amount of H₂O present in D₂O. The relationship between the CH_x species and graphite was explored and it was found that a possible interchange existed between these substances. Neither of these products was found to be associated with the poisoning of CO₂ reduction.

SERS bands of a large number of carbonate/bicarbonate modes were observed. These were from the interfacial region, but did not appear to be involved in the reduction of CO₂ as they varied only slightly in the time dependence studies. Bands were assigned to various carbonate/bicarbonate species but were believed to be due to a more complex molecular structure than that of a free CO₃²⁻ ion. Bands for these species were assigned to $\nu_s(\text{Cu-OCO}_2)$,

$\nu_1(\text{CO}_3^{2-})$, $\nu_2(\text{CO}_3^{2-})$, $\nu_4(\text{CO}_3^{2-})$, $\nu_5(\text{HCO}_3^-)$. As well, it was determined that the bands were not from crystalline azurite or malachite.

Bands attributable to Cu_2O were assigned and compared favourably with spectra from oxide films of exposed copper. An oxide/hydroxide patina was proposed to be the poisoning species in the reaction, after graphite and carbide were ruled out.

5.4 SERS Mechanism

The creation of the SERS active surface permitted the observation of the reduction products from CO_2 . Although this was the focus of the research, the experiments also provided information related to the nature of the SERS mechanism and the active sites.

Differences between the SERS and RRS spectra of Cu_2O provide an interesting contrast between these two spectroscopic techniques. Authors who used 488 nm excitation observed films of Cu_2O grown at anodic potentials. SERS spectra of this film were observed either just at the onset of film growth or during the film decomposition. This highlights the complementary nature of SERS and RRS.

The mechanism of enhancement helps explain the differences in observations. RRS results from an interaction within the molecule of interest. The enhancement from RRS will increase with film thickness. In contrast, SERS results from an interaction between the molecule of interest and the metal surface. Thus SERS works best for very thin films. Thick films prevent the observation of SERS bands.

The CT mechanism of SERS provides for the preferential enhancement of the vibrational modes of molecules in the first layer (i.e., adsorbed on the surface). This makes SERS a sensitive technique for studying reaction intermediates. This was demonstrated for adsorbed CO. Since the frustrated rotation is parallel to the surface, EM enhancement should not be strong and the bands, according to the EM selection rules, should be quite weak. This was not the case.

The field gradient enhancement mechanism does not account for the intensity of the observed bands. According to this enhancement mechanism, molecules are assumed to retain a non-adsorbed symmetry. For adsorbed CO on copper, the frustrated rotation involves a Cu-CO bond. Since carbonyl-metal bonding involves σ and π bonding, a non-adsorbed CuCO would be linear. This would belong to the point group $C_{\infty v}$. Thus, the CuCO frustrated rotation would be a bending mode. This mode would have $\Pi(E_1)$ symmetry. According

to the β values given in the character tables [2] the values of the field gradient terms, A , would be -1 and this vibration would not be enhanced.

Further support for the CT enhancement mechanism is provided by Cu-CO modes not being observed at all potentials where the CO stretch was seen. This suggests that as the electrode potential changes, i.e., the energy of the Fermi level changes, this band is "tuned in" or "tuned out" to an energy level suitable for charge transfer. The observation of bands attributed to the CO stretch when "tuned out" may be due to some EM enhancement of this mode.

The CT mechanism involves adsorption of molecules on special sites (E sites). This may help explain the observation of adsorbed CO at -0.36 V, in advance of the electrochemical reduction of CO₂. Akemann and Otto [87,88] have reported that on disordered Cu in UHV at 40 K, CO₂ can be adsorbed as an activated CO₂⁻. This would have to involve a special absorption site. If this activated adsorption occurred in this system, the CO₂⁻ might be readily reduced to adsorbed CO at potentials much greater than -1.9 V.

5.5 Future Work

The results from the experiments described in this work assisted in the understanding of the mechanism of CO₂ reduction and the associated SERS bands. Further classification of the intermediates could build on this knowledge. The experiments showed that information relating to the SERS active sites could be observed. Thus, further study into the nature of the surface film growth and decomposition could be explored using other systems.

To further prove that the adsorbed CO, observed in this work, is the intermediate in CO₂ reduction, spectroscopic, electrochemical and chromatographic data could be collected concurrently and correlated. The use of these complementary techniques might also yield additional information regarding the nature of the poisoning of this reaction.

The oxide/hydroxide patina needs to be further explored. In CO-saturated and CO₂-saturated solutions the band positions and intensities differed. It may be that in CO-saturated solution the CO was more readily adsorbed despite the fact that CO₂ is more soluble than CO. It could also be due to the pH difference between the electrolytes. In CO₂-saturated solution the pH is maintained at an approximately neutral value due to the participation of the CO₂ in the solution equilibrium. In CO-saturated solutions,

however, the gas will not be an active participant in the solution equilibrium and this will allow the solution pH to shift to higher values. These possibilities could be explored by varying the pH, total carbonate concentrations, cation and temperature of the solutions.

References

1. K. Nakamoto, *Infrared and Raman Spectra of Inorganic and Coordination Compounds*, 3rd ed., Wiley-Interscience, John Wiley and Sons, Toronto, (1978).
2. J.G. Grasselli and B.J Bulkin (Eds.), *Analytical Raman Spectroscopy*, Wiley-Interscience, Toronto, (1991).
3. D.A. Long, *Raman Spectroscopy*, McGraw-Hill, New York, (1977).
4. J.R. Ferraro and K. Nakamoto, *Introductory Raman Spectroscopy*, Academic Press, Toronto, (1994).
5. A. Campion, in *Vibrational Spectroscopy of Molecules at Surfaces*, J.T. Yates, Jr. and T.E. Madey, Eds., p. 345, Plenum Press, New York, (1987).
6. J.A. Creighton, in *Spectroscopy of Surfaces*, Advances in Spectroscopy, Vol. 16, R.J.H. Clark and R.E. Hester, Eds., p. 37, John Wiley and Sons, Toronto, (1988).
7. C. Kittel, *Introduction to Solid State Physics*, 5th ed., John Wiley and Sons, Toronto, (1976).
8. G.A. Somorjai, *Introduction to Surface Chemistry and Catalysis*, John Wiley and Sons, Toronto, (1994).
9. B. Pettinger, in *Adsorption of Molecules at Metal Electrodes*, J. Lipkowski and P.N. Ross, Eds., p. 285, VCH, New York, (1992).
10. N.V. Richardson and N. Sheppard, in *Vibrational Spectroscopy of Molecules at Surfaces*, J.T. Yates, Jr. and T.E. Madey, Eds., p. 1, Plenum Press, New York, (1987).
11. M.W. Urban, *Vibrational Spectroscopy of Molecules and Macromolecules on Surfaces*, Wiley-Interscience, Toronto, (1993).
12. A.M. Bradshaw and E. Schweizer, in *Spectroscopy of Surfaces*, Advances in Spectroscopy, Vol. 16, R.J.H. Clark and R.E. Hester, Eds., p. 413, John Wiley and Sons, Toronto, (1988).
13. B.E. Hayden, in *Vibrational Spectroscopy of Molecules at Surfaces*, J.T. Yates Jr. and T.E. Madey, Eds., p. 267, Plenum Press, New York, (1987).
14. B. Beden and C. Lamy, in *Spectroelectrochemistry Theory and Practice*, R.J. Gale, Ed., p. 189, Plenum Press, New York, (1988).
15. M.A. Chesters and N. Sheppard, in *Spectroscopy of Surfaces*, Advances in Spectroscopy, Vol. 16, R.J.H. Clark and R.E. Hester, Eds., p. 377, John Wiley and Sons, Toronto, (1988).
16. A. Whitley, *Personal Communication*.

17. R.L. McCreery, in *Charge Transfer Devices in Spectroscopy*, J.V. Sweedler, K.L. Ratzloff, and M.B. Denton, Eds., p. 227, VCH, New York, (1994).
18. M. Fleischmann, P.J. Hendra, and A.J. McQuillan, *Chem. Phys. Lett.*, **26**, 163, (1974).
19. Q.J. Huang, J.L. Yao, B.W. Mao, R.A. Gu, and Z.Q. Tian, *Chem. Phys. Lett.*, **271**, 101, (1997).
20. A.G. Brolo, D.E. Irish, and B.D. Smith, *J. Molec. Struct.* **405**, 29, (1997).
21. R.L. Birke, T. Lu, and J.R. Lombardi, in *Techniques for Characterization of Electrodes and Electrochemical Processes*, R. Varma and J.L. Selman, Eds., p. 211, Wiley-Interscience, Toronto, (1991).
22. A. Otto, *J. Raman Spectrosc.*, **22**, 743, (1991).
23. A. Otto, I. Mrozek, H. Grabhorn, and W. Akemann, *J. Phys. Condens. Matter*, **4**, 1143, (1992).
24. J.K. Sass, H. Neff, M. Moskovits, and S. Holloway, *J. Phys. Chem.*, **85**, 621, (1981).
25. M. Moskovits, *Rev. Mod. Phys.*, **57**, 783, (1985).
26. K.J. Maynard and M. Moskovits, *Surf. Sci.*, **225**, 40, (1990).
27. X.J. Gu, K.L. Akers, and M. Moskovits, *J. Phys. Chem.*, **96**, 383, (1992).
28. X.J. Gu, K.L. Akers, and M. Moskovits, *J. Phys. Chem.*, **95**, 3696, (1991).
29. F.T. Wagner, in *Structure of Electrified Interfaces*, J. Lipkowski and P.N. Ross Eds., p. 309, VCH, New York, (1993).
30. A.G. Brolo and D.E. Irish, *J. Electroanal. Chem.*, **414**, 183, (1996).
31. A.G. Brolo and D.E. Irish, *J.C.S. Faraday Trans.*, **93**, 419, (1997).
32. A.G. Brolo, D.E. Irish, G. Szymanski, and J. Lipkowski, *Langmuir*, in press.
33. J.N. Butler, *Carbon Dioxide Equilibria and their Applications*, Lewis, Chelsea, MI, (1991).
34. H. Freiser, *Concepts and Calculations in Analytical Chemistry a Spreadsheet Approach*, CRC Press, Ann Arbour, (1992).
35. A.R. Davis and B.G. Oliver, *J. Solution Chem.*, **1**, 329, (1972).
36. G. Herzberg, *Molecular Spectra and Molecular Structure: II Infrared and Raman Spectra of Polyatomic Molecules*, D. Van Nostrand and Co., Toronto, (1945).

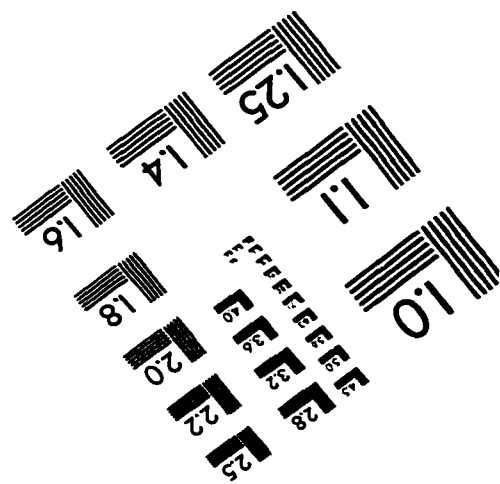
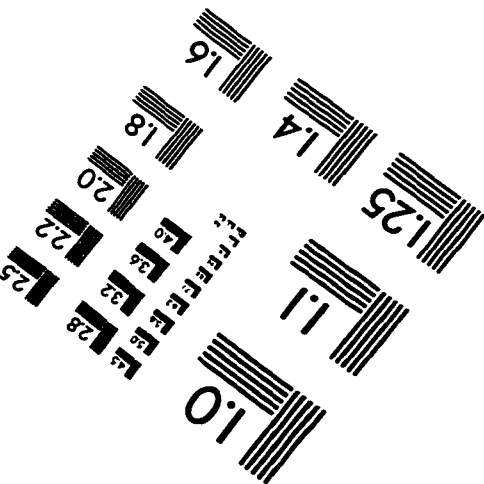
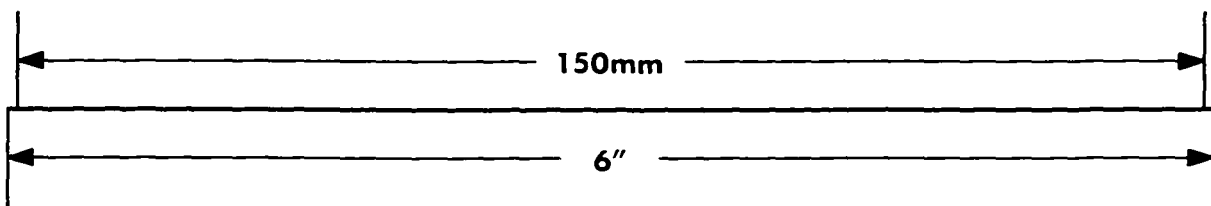
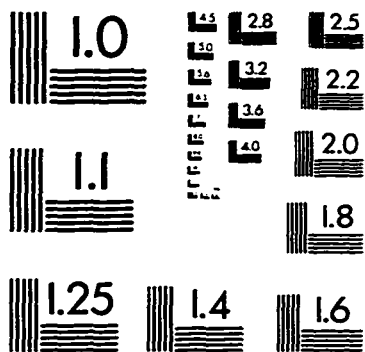
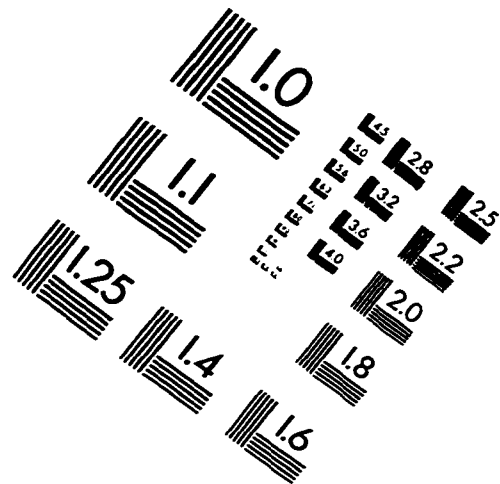
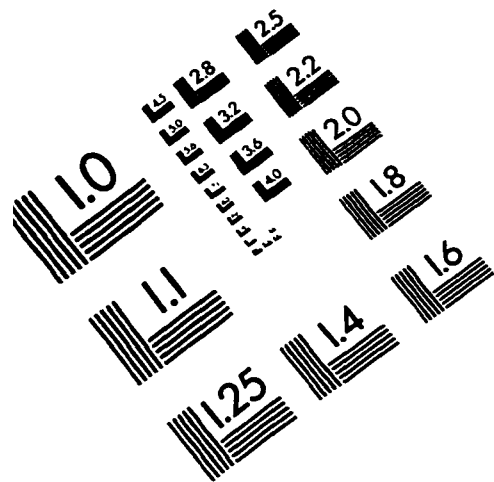
37. F.R. Keene, in *Electrochemical and Electrocatalytic Reactions of Carbon Dioxide*, B.P. Sullivan, K. Krist, and H.E. Guard, Eds., p. 1, Elsevier, New York, (1993).
38. Y. Hori, H. Wakebe, T. Tsukamoto, and O. Koga, *Electrochim. Acta*, **39**, 1833, (1994).
39. K.W. Frese Jr., in *Electrochemical And Electrocatalytic Reactions of Carbon Dioxide*, B.P. Sullivan, K. Krist, and H.E. Guard, Eds., p. 145, Elsevier, New York, (1993).
40. A. Novak, P. Saumange, and L.D.C. Bok, *J. Chim. Phys.*, **72**, 981, (1975).
41. A. Kudelski and J. Bukowska, *Vib. Spectrosc.*, **10**, 335, (1996).
42. H. Furukawa, M. Takahashi, and M. Ito, *J. Electroanal. Chem.*, **256**, 213, (1988).
43. I. Oda, H. Ogasawara, and M. Ito, *Langmuir*, **12**, 1094, (1996).
44. H. Sano, G. Mitzutani, and S. Ushioda, *Phys. Rev. B*, **47**, 13773, (1993).
45. U. Wenning, B. Pettinger, and H. Wetzels, *Chem. Phys. Lett.*, **70**, 49, (1980).
46. B. Chase and B. Parkinson, *J. Phys. Chem.*, **95**, 7810, (1991).
47. I. Pockrand, *Chem. Phys. Lett.*, **85**, 40, (1982).
48. M. Pourbaix, *Atlas d'Equilibres Electrochimiques*, p. 384, Gauthier-Villars & Cie, Paris, (1963).
49. P. Dawson, M.M Hargreave, and G.R. Wilkinson, *J. Phys. Chem. Solids*, **34**, 2201, (1973).
50. M. Cardona, in *Light Scattering in Solids II, Basic Concepts and Instrumentation*, M. Cardona and G. Güntherodt, Eds., p. 19, Springer-Verlag, New York, (1982).
51. K. Reimann and K. Syassen, *Phys. Rev. B*, **39**, 11113, (1989).
52. Y. Petroff, P.Y. Yu, and Y.R. Shen, *Phys. Rev. B*, **12**, 2488, (1975).
53. P.Y. Yu, Y.R. Shen, and Y. Petroff, *Solid State Comm.*, **12**, 973, (1973).
54. M.A. Washington, A.Z. Genback, H.Z. Cummins, H.R. Bruce, A. Compaan, and R.A. Forman, *Phys. Rev. B*, **15**, 2145, (1977).
55. P.Y. Yu, Y.R. Shen, Y. Petroff, and L.M. Falicov, *Phys. Rev. Lett.*, **30**, 283, (1973)
56. P.Y. Yu and Y.R. Shen, *Phys. Rev. Lett.*, **32**, 373, (1974).
57. A. Compaan and H.Z. Cummins, *Phys. Rev. Lett.*, **31**, 41, (1973).

58. P.Y. Yu, Y.R. Shen and Y. Petroff, *Phys. Rev. Lett.*, **29**, 1558, (1972).
59. J.C.W. Taylor and F.L. Weichman, *Can. J. Phys.*, **49**, 601, (1971).
60. S.T. Mayer, *Ph.D. Thesis*, Lawrence Berkeley Laboratory Report, LBL-28085, University of California, Berkeley, CA, (1989).
61. J.C. Hamilton, J.C. Farmer, and R.J. Anderson, *J. Electrochem. Soc.*, **133**, 739, (1986).
62. F.M. Hoffmann, K.C. Lin, R.G. Tobin, C.J. Hirschmugl, G.P. Williams, and P. Dumas, *Surf. Sci.*, **275**, L675, (1992)
63. S.T. Mayer and R.H. Muller, *J. Electrochem. Soc.*, **139**, 426, (1992).
64. C.A. Melendres S. Xu, and B. Tani, *J. Electroanal. Chem.*, **162**, 343, (1984).
65. C.A. Melendres, G.A. Bowmaker, B.Beden, and J.M. Leger, in *Proceedings of the International Symposium on New Directions in Electroanalytical Chemistry*, The Electrochemical Society Proceedings, Vol. PV 96-9, J. Leddy and M. Wightman, Eds., p. 224, The Electrochemical Society, Pennington, NJ, (1996).
66. D. Persson and C. Leygraf, *J. Electrochem. Soc.*, **140**, 1256, (1993).
67. K.T. Carron, G. Xue, and M.L. Lewis, *Langmuir*, **7**, 2, (1991).
68. G. Xue and J. Zhang, *Appl. Spectrosc.*, **45**, 760, (1991).
69. T. Nanba and T.P. Martin, *Phys. Stat. Sol.*, **76A**, 235, (1983).
70. H. Hagemann, H. Bill, W. Sadowski, E. Walker, and M. Francois, *Solid State Commun.*, **73**, 147, (1990).
71. S.N. Narang, V.B. Kartha, and N.D. Patel, *Physica C*, **204**, 8, (1992).
72. A.F. Wells, *Structural Inorganic Chemistry*, 5th ed., Clarendon, Oxford, (1984).
73. A.M. Pollard, R.G. Thomas, P.A. Williams, J. Just, and P.J. Bridge, *Mineral Mag.*, **55**, 163, (1991).
74. J.A. Goldsmith and S.D. Ross, *Spectrochim. Acta*, **24A**, 2131, (1968).
75. M. Schmidt and H.D. Lutz, *Phys. Chem. Minerals*, **20**, 27, (1993).
76. L. Burgio, D.A. Ciomartan, and R.J.H. Clark, *J. Raman Spectrosc.*, **28**, 79, (1997).
77. B. Taravel, M. Berjot, and F. Fromage, *C.R. Acad. Sc.*, **279B**, 159, (1974).
78. M. Pourbaix, *Lectures on Electrochemical Corrosion*, Plenum Press, New York, (1973).

79. W. Stumm and J.J. Morgan, *Aquatic Chemistry*, 3rd ed., Wiley-Interscience, Toronto, (1996).
80. M. Perez Sanchez, M. Barrera, S. Gonzalez, R.M. Souto, R.C. Salvarezza, and A.J. Arvia, *Electrochim. Acta*, **35**, 1137, (1990).
81. W. Akemann and A. Otto, *J. Raman Spectrosc.*, **22**, 797, (1991).
82. J.R. Rack, J.D. Webb, and S.H. Strauss, *Inorg. Chem.*, **35**, 277, (1996).
83. C.J. Hirschmugl, G.P. Williams, F.M. Hoffmann, and Y.J. Chabal, *Phys. Rev. Lett.*, **65**, 481, (1990).
84. Y. Hori, A. Murata, T. Tsukamoto, H. Wakebe, O. Koga, and H. Yamazaki, *Electrochim. Acta*, **39**, 2495, (1994).
85. Y. Hori, O. Koga, H. Yamazaki, and T. Matsuo, *Electrochim. Acta*, **40**, 2617, (1995).
86. B. Westerhoff and R. Holze, *Ber. Bunsenges. Phys. Chem.*, **97**, 418, (1993).
87. W. Akemann and A. Otto, *Surf. Sci.*, **287/288**, 104, (1993).
88. W. Akemann and A. Otto, *Surf.Sci.*, **272**, 211, (1992).
89. S.A. Hartinger, B. Pettinger, and K. Doblhofer, *J. Electroanal. Chem.*, **397**, 335, (1995).
90. H. Yu, D.Q. Hu, K.T. Leung, *Surf. Sci.*, **355**, L335, (1996).
91. J.M. Mundernar, A.P. Baddorf, E.W. Plummer, L.G. Sneddon, R.A. Didio, and D.M. Zehner, *Surf. Sci.*, **188**, 15, (1987).
92. A.P. Baddorf and J.E. Wendelken, *Surf. Sci.*, **256**, 264, (1991).
93. B. Pettinger, M.R. Philpott, and J.G. Gordon, *Surf. Sci.*, **105**, 469, (1981).
94. Y.X. Chen and Z.Q. Tian, *Chem. Phys. Lett.*, submitted, (1997).
95. N. Iwasaki, Y. Sasaki, and Y. Nishna, *Surf. Sci.*, **198**, 524, (1988).
96. P.B. Dorain, *J. Phys. Chem.*, **90**, 5808, (1986).
97. P.B. Dorain, *J. Phys. Chem.*, **90**, 5812, (1986).
98. P.B. Dorain, *J. Phys. Chem.*, **92**, 2546, (1988).
99. I. Pockrand, *Surf. Sci.*, **122**, L569, (1982).
100. I. Pockrand, *Surface Enhanced Raman Vibrational Studies at the Solid/Gas Interface*, Springer Tracts in Modern Physics, Vol. 104, Springer-Verlag, New York, (1984).
101. H. Ibach and S. Lehwald, *Surf. Sci.*, **91**, 187, (1980).

102. D. W. DeWulf, T. Jin, and A.J. Bard, *J. Electrochem. Soc.*, **136**, 1686, (1989).
103. B. Jermann and J. Augustynski, *Electrochim. Acta*, **39**, 1891, (1994).
104. Y. Hori, K. Kikuchi, A. Murata, and S. Suzuki, *Chem. Lett.*, 897, (1986).
105. Y. Hori, K. Kikuchi, and S. Suzuki, *Chem. Lett.*, 1695, (1985).
106. Y. Hori, A. Murata, and R. Takahashi, *J. Chem. Soc. Faraday Trans. I*, **85**, 2309, (1989).
107. J.J. Kim, D.P. Summers, and K.W. Frese, Jr., *J. Electroanal Chem.*, **245**, 223, (1988).
108. A. Santoni and J. Urban, *Surf. Sci.*, **186**, 376, (1987).
109. R.W. Joyner, G.R. Darling, and J.B. Pendry, *Surf. Sci.*, **205**, 513, (1988).
110. V.I. Ivanov-Omskii and G.S. Frolova, *Tech. Phys.*, **40**, 966, (1995).
111. M. Mahoney, M.W. Howard, and R.P. Cooney, *Chem. Phys. Lett.*, **71**, 59, (1980).
112. Y. Ichinohe, T. Wadayama, and A. Hatta, *J. Raman Spectrosc.*, **26**, 335, (1995).
113. B.D. Smith and D.E. Irish, in *Proceedings of the 15th International Conference on Raman Spectroscopy*, S.A Asher and P.B. Stein Eds., p. 742, John Wiley and Sons, Toronto, (1996).
114. G. Aloisi, A.M. Funtikov and R. Guidelli, *Surf. Sci.*, **296**, 291, (1993).
115. R.K. Chang and B.L. Laube, *CRC Crit. Rev. Solid State Mater. Sci.*, **12**, 1, (1986).
116. B.D. Smith and D.E. Irish, unpublished.
117. B. Jermann, *Ph.D. Thesis*, University of Geneva, (1996).
118. P.N. Ross, in *Standard Potentials in Aqueous Solution*, A.J. Bard, R.P. Parsons, and J.Jordan, Eds., p. 39, IUPAC, Marcel Dekker, New York, (1985).
119. Y. Wang, D.C. Alsmeyer, and R.L. McCreery, *Chem. Mater.*, **2**, 557, (1990).
120. D.E. Irish and M.H. Brooker, in *Advances in Infrared and Raman Spectroscopy Vol. 2*, R.J.H. Clark and R.E. Hester Eds., p. 212, John Wiley and Sons, Toronto, (1976).

IMAGE EVALUATION TEST TARGET (QA-3)



APPLIED IMAGE, Inc
 1653 East Main Street
 Rochester, NY 14609 USA
 Phone: 716/482-0300
 Fax: 716/288-5989

© 1993, Applied Image, Inc., All Rights Reserved